

THESIS FOR THE DEGREE OF DOCTOR OF PHILOSOPHY

**Functionalization and Characterization of Carbon Based Nanomaterials for  
Electronics, Composite and Biomedical Applications**

Nan Wang



**CHALMERS**

Department of Microtechnology and Nanoscience (MC2)

Electronics Materials and Systems Laboratory (EMSL)

CHALMERS UNIVERSITY OF TECHNOLOGY

Göteborg, Sweden 2017

# **Functionalization and Characterization of Carbon Based Nanomaterials for Electronics, Composite and Biomedical Applications**

**Nan Wang**

© 2017 Nan Wang

Department of Microtechnology and Nanoscience (MC2)

Electronics Materials and Systems Laboratory (EMSL)

ISSN 1652-0769

Technical report no MC2- 359

Chalmers University of Technology

Department of Microtechnology and Nanoscience (MC2)

Electronics Materials and Systems Laboratory (EMSL)

SE-412 96 Göteborg, Sweden

Telephone +46 (0)31-772 1000

Printed by Chalmers Reproservice  
Göteborg, Sweden 2017

# Abstract

Surface functionalization of nanomaterials to combine different material's properties together opens up unlimited possibilities for both academic research and industrial applications. In this thesis, flexible and scalable chemical approaches to functionalize carbon nanomaterials (CNMs) are developed for different applications, including electronics, composite and biomedical applications. According to the bonding difference between CNMs and functional components, these approaches can be divided into two groups, including covalent functionalization and non-covalent functionalization.

Covalent functionalization of CNMs surface is based on reactions of different components with the oxygen-containing groups of CNMs. The first part in this section introduced the covalent functionalization of carbon nanotubes for biomedical application. The surface of CNTs was modify by a multi-oxidation process and coated by silver nanoparticles to improve CNT's antibacterial property. The developed silver/CNT composites show strong antibacterial property to bacteria. The second part presents covalent functionalization of graphene oxide for cement reinforcement. The developed surface functionalized GO (FGO) can improve both the early and ultimate strength of the Portland cement mortar efficiently. The key benefit of FGO lies in its ability to form covalent bonds with C-S-H whilst having minimum effect on the workability of mortar paste. The third part introduced the covalent functionalization of graphene based films (GBFs) that act as heat spreaders for hotspot cooling. The applied covalent bonding between GBF and the substrate can significantly reduce the thermal interface resistance, showing great advantages on cooling of high-power density devices.

Non-covalent functionalization utilizes various functional molecules or active species as assembly mediators to functionalize the surface of CNMs via non-covalent interactions. The first part of this section presents a method of non-covalent self-assembly of high-thermal-conductivity of graphene films (GFs). The fabricated smooth, large-grain and turbostratic-stacking GFs shows excellent thermal and mechanical properties, which is superior to most of currently existing thermally conductive materials. The second part introduced the non-covalent functionalization of graphene for high thermal conductive adhesive. Liquid exfoliated few-layer graphene was utilized as fillers to improve the thermal conductivity of the thermal conductive adhesive which showed an improvement of 400 %. The third part presents a non-covalent functionalization process for synthesizing intrinsically flexible multi-functionalized CNT based hybrid nanowires. The synthesized multi-functionalized CNT based hybrid nanowires possess many excellent properties, such as good dispersability and stability in various polar solvents, large flexibility and high electrical conductivity. These extraordinary properties facilitate the application of hybrid nanowires in the fabrication of flexible and stretchable circuits (FSCs) with high resolution.

**Keywords:** carbon nanomaterials, functionalization, graphene, flexible electronics, hybrid nanowires



# List of Publications

## Appended papers and manuscript

This thesis is based on the following appended papers and manuscript

**A Efficient surface modification of carbon nanotubes for fabricating high performance CNT based hybrid nanostructures**

N. Wang, S. Pandit, L. Ye, M. Edwards, V.R.S.S. Mokkalapati, M. Murugesan, V. Kuzmenko, C. Zhao, F. Westerlund, I. Mijakovic, J. Liu,  
*Journal Paper – Carbon. 111 (2017) 402–410. doi:10.1016/j.carbon.2016.10.027*

**B Functionalized Graphene Oxide Reinforced Cement for Improved Mechanical Strength**

N. Wang, S. Wang, L. Tang, L. Ye, J. Liu  
*Submitted*

**C Improved Heat Spreading Performance of Functionalized Graphene in Micro electronic Device Application**

Y. Zhang, H. Han, N. Wang, P. Zhang, Y. Fu, M. Murugesan, M. Edwards, K. Jeppson, S. Volz, J. Liu  
*Journal Paper – Advanced Functional Materials: 5 JUN 2015. 25 (2015) 4430–4435. doi:10.1002/adfm.201500990*

**D Functionalization mediates heat transport in graphene nanoflakes**

H. Han, Y. Zhang, N. Wang, M.K. Samani, Y. Ni, Z.Y. Mijbil, M. Edwards, S. Xiong, K. Säaskilahti, M. Murugesan, Y. Fu, L. Ye, H. Sadeghi, S. Bailey, Y.A. Kosevich, C.J. Lambert, J. Liu, S. Volz, Co-1<sup>st</sup> Author  
*Journal Paper – Nature Communication. 7 (2016) 11281. doi:10.1038/ncomms11281.*

**E Large-scale production of graphene films with high thermal conductivity**

N. Wang, M. Samani, H. Li, L. Dong, Z. Zhang, P. Su, S. Chen, J. Chen, S. Huang, G. Yuan, X. Xu, B. Li, K. Leifer, L. Ye, J. Liu  
*Submitted*

**F Development and Characterization of Graphene Enhanced Thermal Conductive Adhesives**

N. Wang, N. Logothetis, W. Mu, S. Huang, L. Ye, J. Liu, INVITED PAPER  
*Conference paper – 2016 6th Electronic System-Integration Technology Conference ESTC, 2016: pp. 1–6. doi:10.1109/ESTC.2016.7764682.*

**G Flexible Multi-functionalized Carbon Nanotubes Based Hybrid Nanowires**

N. Wang, D. Jiang, L. Ye, M. Murugesan, M. Edwards, Y. Fu, J. Liu  
*Journal Paper –Advanced Functional Materials 2015, 25, 26:4135–4143 (DOI: 10.1002/adfm.201501017 )*

**H Embedded Fin-Like Metal/CNT Hybrid Structures for Flexible and Transparent Conductors,**

D. Jiang, N. Wang, M. Edwards, W. Mu, A. Nylander, Y. Fu, K. Jeppson, J. Liu, Co-1<sup>st</sup>  
Author

*Journal Paper –Small 12 (2016) 1521–1526. doi:10.1002/sml.201503091*

## Other contributions

The following selection of contributions is appended to the thesis due to overlap or being outside of the scope of the thesis:

**A Thermal characterization of power devices using graphene-based film**

Pengtu Zhang, Nan Wang, Carl Zandén, Lilei Ye, Yifeng Fu, Johan Liu

*Proceedings – 2014 64th IEEE Electronic Components and Technology Conference (ECTC) 459–463. doi:10.1109/ECTC.2014.6897324*

**B Development and characterization of graphene-enhanced thermal conductive adhesives**

Marcello Casa, Nan Wang, Huang Shirong, Lilei Ye, Ciambelli Paolo, Johan Liu

*Proceedings – 2014 15th International Conference on Electronic Packaging Technology (ICEPT) 480–483. doi:10.1109/ICEPT.2014.6922700*

**C Use of graphene-based films for hot spot cooling**

Yong Zhang, Pengtu Zhang, Nan Wang, Yifeng Fu, Johan Liu

Proceedings of the 5th Electronics System-Integration Technology Conference, ESTC 2014 p. Art. no. 6962834. (2014)

**D Reliability investigation of nano-enhanced thermal conductive adhesives**

Nan Wang, Murali Murugesan, Lilei Ye, Björn Carlberg, Si Chen, Johan Liu

*Proceedings – of the 2012 12th IEEE Conference on Nanotechnology, doi:10.1109/NANO.2012.6322137*



# Abbreviations

CNT	Carbon Nanotube
ED	Ethylenediamine
EDTA	Ethylenediaminetetraacetic acid
PVP	polyvinylpyrrolidone
APTES	(3-Aminopropyl)triethoxysilane
PDMS	Polydimethylsiloxane
TEM	Transmission electron microscopy
SEM	Scanning Electron Microscopy
FT-IR	Fourier transform infrared spectroscopy
XRD	X-ray diffraction
UV	Ultra violet
FSCs	Flexible and stretchable circuits
LED	Light-emitting diode
TGA	Thermogravimetric analysis
BET	Brunauer-Emmett-Teller
BJH	Barrett-Joyner-Halenda
GO	Graphene oxide
GBF	Graphene based film



# Table of Contents

<b>Abstract .....</b>	<b>I</b>
<b>List of Publications.....</b>	<b>III</b>
<b>Chapter 1.....</b>	<b>1</b>
1.1 Nanotechnology and Nanomaterials .....	1
1.2 Carbon-based nanomaterials .....	2
1.3 Functionalization of CNMs.....	3
1.4 Scope and outline .....	6
<b>Chapter 2.....</b>	<b>9</b>
2.1 Covalent functionalization of carbon nanotubes for biomedical application.....	9
2.1.1 Surface activation of CNTs .....	10
2.1.2 Deposition of silver nanoparticles on the activated CNTs.....	14
2.1.3 Anti-bacterial activity of M-CNT/Ag .....	16
2.1.4 Conclusion.....	19
2.2 Covalent functionalization of graphene oxide for cement reinforcement.....	19
2.2.1 The morphology and composition of FGO .....	22
2.2.2 Workability study.....	23
2.2.3 Mechanical strength .....	24
2.2.4 Microstructure analysis .....	26
2.2.5 Conclusions .....	27
2.3 Covalent functionalization of GBF for improving its cooling property.....	27
2.3.1 Thermal resistance measurement with photothermal reflectance. ....	30
2.3.2 Heat spreading through different functional molecules. ....	30
<b>Chapter 3.....</b>	<b>35</b>

3.1	Non-covalent self-assembly of high-thermal-conductivity of graphene films....	35
3.1.1	Optimization of GF self-assembly process .....	36
3.1.2	Reduction of GFs .....	43
3.1.3	Thermal conductivity of GFs .....	48
3.1.4	GFs as superior heat-spreading material .....	55
3.1.5	GFs are flexible and have superior mechanical strength.....	57
3.1.6	Conclusions .....	58
3.2	Non-covalent functionalization of graphene for high thermal conductive adhesive	58
3.2.1	Mechanical exfoliation of graphene.....	59
3.2.2	Thermal performance of graphene enhanced TCAs .....	62
3.2.3	Demonstration .....	64
3.2.4	Conclusions .....	65
3.3	Non-covalent functionalization of carbon nanotube for flexible electronic application .....	65
3.3.1	Functionalization of CNT surface by APTES and SiO <sub>2</sub> .....	66
3.3.2	Deposition of silver nanoparticles on the functionalized CNTs .....	70
3.3.3	Fabrication of flexible and stretchable electrical circuits.....	71
3.3.4	Electro-mechanical properties and reliability of FSCs .....	75
3.3.5	Flexibility and reliability of FSCs .....	77
3.3.6	Stretchability and reliability of FSCs .....	79
3.3.7	Improved stretchability and reliability of FSCs .....	81
	<b>Chapter 4.....</b>	<b>85</b>
	<b>Acknowledgements.....</b>	<b>87</b>
	<b>Bibliography.....</b>	<b>89</b>





# Chapter 1

## Introduction

### 1.1 Nanotechnology and Nanomaterials

Nanotechnology, as an emerging/enabling technology, is helping to considerably improve, even revolutionize, many traditional technologies and industry areas, ranging from electronic packaging to energy conversion and storage[1–8], from additives to catalysis[9–11], and from sensors to drug delivery and biomedical applications[12–17]. Driven by the great benefits from these applications, all kinds of research based on nanotechnologies have been carried out in multi-disciplinary areas. In order to distinguish this new technology from the traditional disciplines, the generalized definition of nanotechnology was subsequently established by the National Nanotechnology Initiative, which describes nanotechnology as the manipulation of materials with at least one dimension sized from 1 to 100 nanometers[18]. The reason for such a definition is that most fundamental physical properties of materials can change when the geometry size is reduced to a critical value well below 100 nm in at least one dimension. Table 1.1 shows an overview of the effects and potential applications of the reduced dimensionality of nanomaterials[19].

A variety of nanomaterials have been fabricated and applied in many areas. Generally, nanomaterials can be classified into four groups according to their structural dimensions[20]. As shown in Figure 1-1, zero-dimensional (0D) nanomaterials means that materials are nanoscale in all dimensions, including all kinds of nanoparticles ranging from metal to ceramic. One dimensional (1D) nanomaterials are described as materials which have one dimension larger than nanoscale, such as nanowires and nanotubes. Among them, carbon

**Table 1.1** an overview of the effects and potential applications of the reduced dimensionality of nanomaterials

Nanoscale effects	Applications
High surface-to-volume ratio and enhanced reactivity	Catalysis, solar cells, batteries, gas sensors
Enhanced electrical properties	Conducting materials
Increased hardness from small crystal grain size	Hard coatings, thin protection layers
Narrower electronic band gap	Opto-electronics
Lower melting and sintering temperatures	Processing of materials, low sintering materials
Improved transport kinetics	Batteries, hydrogen storage
Improved reliability	Nanoparticle-encapsulated electronic components
Increased wear resistance	Hard coatings, tools
Higher resistivity with smaller grain size	Electronics, passive component, sensors

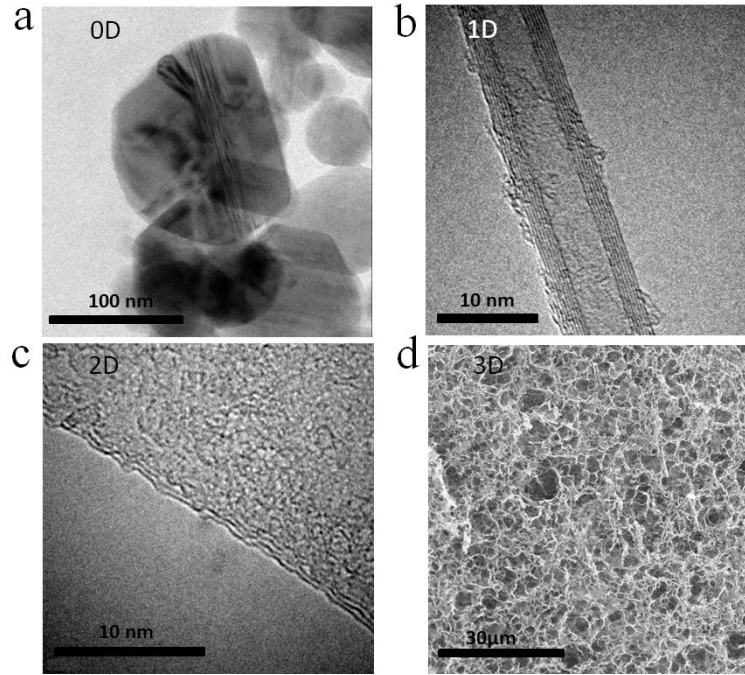


**Figure 1-1** Different types of nanomaterials classified by structural dimensions (a) 0D silicon carbide nanoparticles (b) 1D multi-walled carbon nanotube (c) 2D multilayer graphene (d) 3D graphene sponge

nanotubes (CNT), including single-walled carbon nanotubes (SWCNT) and multi-walled carbon nanotubes (MWCNTs), are the most representative 1D nanomaterial. Two-dimensional (2D) nanomaterials usually refer to thin-sheet materials with nanoscale thickness. For example, graphene, one or few layers of carbon atoms, have been regarded as one of the most promising 2D nanomaterials. Three-dimensional (3D) nanomaterials usually include powders, fibrous, multilayer and polycrystalline materials which are constructed by all kinds of building blocks, such as 0D, 1D and 2D nanomaterials. The building blocks are in close contact with each other and form interfaces inside 3D nanomaterials. Figure 1-1d shows the 3D graphene sponge in which individual graphene sheet are bonded together through self-assembly. This special 3D structure has the advantages of large surface area and extremely low density, making it a promising material for supercapacitors[21].

## 1.2 Carbon-based nanomaterials

Carbon is well known to form distinct solid state allotropes with diverse structures ranging from  $sp^3$  bonded diamond to  $sp^2$  bonded fullerene and graphite. Mixed states are also possible and form the basis of amorphous carbon[22]. The diversity of carbon-lattice structures can lead to great differences on bulk properties ranging from mechanical strength to electrical and thermal performance. Diamond is a metastable form of carbon that possesses a face-centered cubic lattice structure with a lattice constant of 3.57 Å and C–C bond length of 1.54 Å. Such extremely rigid lattice structure endows diamond with superlative physical qualities, such as the highest hardness and thermal conductivity of all the bulk material[23]. In

contrast, graphite is the most thermodynamically stable form of carbon under normal conditions and consists of a layered planer structure where the carbon atoms are arranged in a hexagonal honeycomb lattice with a bond length of 1.42 Å. These single atom thick layers (i.e., graphene layers) are bonded via noncovalent van der Waals forces with an interlayer spacing of 3.35 Å. Such a special layered two-dimensional structure would benefit the phonon transfer in horizontal direction by giving a large group velocity and long mean free path. Consequently, graphite shows superior in-plane thermal and electrical conductivities which facilitate its widespread application in thermal management and electrodes[24]. In addition, the loose interlamellar coupling between graphene layers makes graphite to be an excellent lubricant that has been widely used in industry[25].

The weak interlayer bonding in graphite implies that graphite can be exfoliated and engineered to various types of carbon-based nanomaterials (CNM), including fullerenes, single or multi-walled nanotubes and graphene. Fullerenes are the zero-dimensional form of graphitic carbon that can be visualized as an irregular sheet of graphene being curled up into a sphere by incorporating pentagons in its structure. The first fullerene molecule was discovered in 1985 and named as buckminsterfullerene (C<sub>60</sub>) which is the smallest fullerene molecule containing pentagonal and hexagonal rings. Nowadays, fullerene molecules come in various forms and sizes ranging from 30 to 3000 carbon atoms, which have been widely researched in lots of areas, such as solar cells, superconductors, x-ray imaging contrast agents and drug delivery[26–29].

Among all kinds of CNMs, CNTs and graphene are the most popular 1D and 2D nanomaterials that have been extensively studied in the past two decades. Comprising of a  $sp^2$  bonded hexagonal graphitic structure, CNTs and graphene both possess excellent mechanical strength, electrical and thermal conductivity, and optical properties. The Young's modulus and tensile strength of a CNT and graphene can reach to 1 TPa and 130 GPa[30]. Electron mobility of graphene is more than  $15000 \text{ cm}^2 \cdot \text{V}^{-1} \cdot \text{s}^{-1}$ , and the current density of metallic CNTs are orders of magnitude higher than those of metals such as copper[31,32]. Thermal conductivities of a single CNT and graphene are about 3000 W/mK and 5000 W/mK respectively[33]. The light absorption ratio of single-layer graphene is just 2.5%[34]. Lots of the research efforts have been focused on utilizing these advantageous properties for various applications including electronics, biological engineering, filtration, lightweight/strong composite materials, photovoltaics and energy storage[35–38].

### 1.3 Functionalization of CNMs

Surface functionalization of nanomaterials refer to assemble different organic and inorganic materials together in nanoscale through covalent bonds or non-covalent bonds including hydrogen bonds, the electrostatic force, or the van der Waals force[39]. The unlimited possible combinations of the distinct properties of inorganic, organic, or even bioactive components have attracted considerable attention[40–42]. So far, a vast number of novel advanced functionalized CNMs with well-controlled structures and multiple functions have been created and applied in many fields. For example, flexible electrode materials

consisting of highly electrically conductive metal nanoparticles coated CNTs demonstrate collective properties of high current density and good flexibility[43]. Graphene coated with ferromagnetic nanoparticles exhibit controlled movement under magnetic fields, demonstrating great potential for magnetic recording[44]. In particular, CNTs deposited with catalytic nanoparticles, such as Pt, Pd and Ru, may provide high-performance catalysts for applications in fuel cell electrodes, Li-ion batteries and supercapacitors[45–47].

A variety of physical and chemical approaches have been developed to controllably design and functionalize CNMs with different functional components at the nanoscale[48–52]. Generally, these functional routes can be divided into two types, including covalent functionalization and non-covalent functionalization, according to the different connection mechanisms between CNMs with the functional components.

The covalent functionalization is based on forming covalent bonds between functional components and carbon atoms in the basal plane of CNMs[53]. Due to the chemically inert and hydrophobic properties of graphite, it is usually difficult to directly assemble functional components on the surface of CNMs. Therefore, the covalent functionalization of CNMs is necessary for fabrication of CNM-enhanced composites. During the functionalization, a vast number of oxygen-containing groups, such as carbonyl and carboxyl groups, would be grafted onto the graphitic surfaces and form covalent bonds to the p-conjugated skeleton of CNMs under aggressive conditions (e.g., strong acid oxidization or plasma etching)[54,55]. These oxygen-containing groups show high reactivity with many other functional nanomaterials and also possibly act as attaching points for further assembling of nanohybrids.

However, in most cases, the covalent functionalization processes unavoidably cause the destruction of the graphitic structures, and thus compromise their intrinsic electronic and mechanical properties. Therefore, there is a growing interest in the development of non-covalent interactions between the CNMs and functional components. The principle ideas of non-covalent assembly are to utilize various functional molecules or active species as assembly mediators to functionalize the surface of CNMs via non-covalent interactions such as hydrophobic[56],  $\pi$ - $\pi$  stacking[57], van der Waals force[39], and wrapping interactions[58,59]. The assembled mediators then act as binding points for anchoring other molecules or nanomaterials.

Previous research has revealed the chemical mechanisms behind different methods of non-covalent functionalization. The first method, hydrophobic interaction, utilizes long chains of aliphatic compounds to interact with the hydrophobic surface of CNMs and functionalize the surface with active groups. As an example, sodium dodecyl sulfate (SDS) is a well-known anionic surfactant for dispersing CNTs, which can be absorbed to the surface of CNTs and cover them with active sulfate groups[60]. The second method of non-covalent assembly is  $\pi$ - $\pi$  stacking in which the pyrenyl group is used to interact with CNMs. The pyrenyl group is well known to be highly aromatic in nature and able to bind strongly with the basal plane of graphite and/or sidewalls of the nanotubes via  $\pi$ - $\pi$  stacking, thus providing a fixation point for the attachment of functional components[61]. The other method is called polymer wrapping in which polymer molecule can be absorbed onto the surface of CNMs and form a coating layer through electrostatic interactions. The functional groups of the polymer enable the assembly of a variety of organic and inorganic nanostructures[62]. Table 1.2 highlights the different

**Table 1.2** Overview of different functionalization approaches on CNMs

Functionalization				
Interaction mechanism	Types	Active functional groups	Examples	Potential application
Covalent bonds	Oxidation	-COOH	Ag-CNM,	Composites
	Oxygen plasma	-OH -O-	Au-CNM	
Hydrophobic	Non-ionic aliphatic	-SH, -COOH, -NH <sub>2</sub>	Au-CNM (dodecanethiol), TiO <sub>2</sub> -CNM (oleic acid)	Photo switch, chemical sensor.
	Ionic aliphatic	Charged group	Ru-CNM(SDS)	Fuel cell
$\pi$ - $\pi$ stacking	Non-ionic aromatic	-SH, -COOH, -NH <sub>2</sub> , -OH	Ag-CNM (benzyl mercaptan), Co-CNM (pyrene derivative)	Conductive material
	Ionic aromatic	Charged group	Pt, Pd, Ru, Rh-CNM (IIL)	Electrochemical catalysis
Attraction	Van der Waals' force	Hydrogen bond	Graphene film and fiber	Self-assembly
Wrapping	Homopolymer	Charged group, -NH <sub>2</sub>	Au, Fe <sub>3</sub> O <sub>4</sub> -CNM (PSS/PDDA)	Nano-reinforced fiber material
	Copolymer	Charged group, -SH	Au, Cu, Fe-CNM (PSMA)	Single-electron device
	DNA	-SH,	Au-CNM (DNA)	Vapor sensing
Doping		N	Au, Ag, Cu, Pd (N-CNM)	Supercapacitor field emission
Direct deposition	E-beam deposition,		Ag-CNM	Nano electronic device
	Electrochemical deposition		Au, Ag, Cu, Pd-CNM	

functionalization approaches which have been used for assembling various organic/inorganic functional nanostructures onto the surface of CNMs[39].

## 1.4 Scope and outline

The thesis focuses on developing flexible and scalable chemical approaches to functionalize CNMs and investigating their potential applications. According to the bonding difference between CNMs and the functional components, these functionalization approaches can be divided into two groups, namely covalent functionalization and non-covalent functionalization.

Chapter 1 gives a general introduction of different nanomaterials and their unique properties, especially on CNMs. In addition, different functionalization processes and how they manipulate CNMs structures and properties are described and explored.

Chapter 2 focuses on the covalent functionalization of CNMs. It includes three parts of work that target on CNTs and graphene respectively. The first part introduces a process to **covalent functionalize carbon nanotubes for biomedical application**. To improve the bonding strength between CNTs and attached functional components, a multi-oxidation process was developed to modify the original chemically inert graphitic surface of CNTs. The surfaces of the modified CNTs were coated by silver nanoparticles to improve CNT's antibacterial property. The developed silver/CNT composites show strong antibacterial property to E.coli bacteria. The second part presents **covalent functionalization of graphene oxide for cement reinforcement**. A special surface functionalized GO (FGO) was synthesized and employed as the reinforcing agent to improve the ultimate strength of the Portland cement mortar. The key benefit of FGO lies in its ability to form covalent bonds with C-S-H whilst having minimum effect on the workability of mortar paste. The third part introduced the **covalent functionalization of graphene based films (GBFs) that act as heat spreaders for hotspot cooling**. The covalent bonding between GBF and the substrate is realized via the linkage of a silane coupling agent which can significantly reduce the thermal interface resistance and improve the cooling effect. Such results show great potential in the thermal management of high-power density devices.

Chapter 3 focuses on the Non-covalent functionalization of CNMs, The first part presents a method of **non-covalent self-assembly of high-thermal-conductivity of graphene films**. The fabrication of the graphene film is based on phase change of graphene oxide sheets from random dispersion to liquid crystal in aqueous solution, and followed by graphitization and pressing. It yields smooth, large-grain and turbostratic-stacking GFs with an in-plane thermal conductivity over 3200 W/mK, which is superior to currently existing thermally conductive pyrolytic graphite sheets by over 60%. The fabricated GFs also have excellent flexibility and mechanical tensile strength. It thus opens for addressing major heat dissipation issues in current form-factor driven electronics and other high power driven systems. The second part introduced the **non-covalent functionalization of graphene for high thermal conductive adhesive**. Liquid exfoliated few-layer graphene was utilized as fillers to improve the thermal conductivity of the thermal conductive adhesive. To overcome the Van der Waals' force

between graphene layers, proper solvents with similar surface tensile as graphene were selected as the exfoliation solvents, which demonstrated excellent exfoliation efficiency and solution stability. Thermal conductivity of thermal conductive adhesive with 3% of graphene was increased about four times than the reference sample, which demonstrated superior heat dissipation properties. The viscosity of the paste was regulated in an acceptable range by decreasing the interaction of nanofillers and polymer binder molecules. The third part presents a **non-covalent functionalization process for synthesizing intrinsically flexible multi-functionalized CNT based hybrid nanowires**. The multi-functionalized CNT based hybrid nanowires were synthesized with different functional materials on the surface of CNTs to produce a metal nanoparticle coating layer and form uniform dispersions whilst possessing the CNT's original structural integrity and high flexibility. The synthesized multi-functionalized CNT based hybrid nanowires possess many excellent properties, such as good dispersability and stability in various polar solvents, large flexibility and high electrical conductivity. These extraordinary properties facilitate the application of hybrid nanowires in the fabrication of flexible and stretchable circuits (FSCs) with high resolution. The electro-mechanical properties and reliability of FSCs are also investigated. The results show good flexibility and stable electrical performance of FSCs under different structural deformation. Light-emitting diodes (LED) demonstrators are also fabricated, which illustrate the superior mechanical and electrical performance of multi-functionalized CNT based FSCs.

The conclusions and future outlook are summarized in chapter 4



# Chapter 2

## Covalent Functionalization of CNMs

### 2.1 Covalent functionalization of carbon nanotubes for biomedical application

Covalent assembly of nanostructures onto CNTs surface is based on covalent functionalization of CNT, in which the oxygen-containing groups (e.g carbonyl and carboxyl groups) are introduced directly onto the CNT surfaces through bonding to the  $\pi$ -conjugated skeleton of the CNTs under aggressive conditions, such as strong acid oxidation or plasma etching.

In this section, we introduced a multi-oxidation process to modify the original chemically inert graphitic surface of CNTs for close bonding with silver nanoparticles. The key benefit of the multi-oxidation process lies in its abilities to create a porous out layer with abundant nanoscale defects and also bond large amount of oxygen-containing groups on the surface of CNTs. These surface modifications of CNTs facilitate the penetration of silver cations into the deep layer of CNTs and form silver nanoparticles that closely bonded with the CNT surface. Moreover, the oxygen containing groups can offer excellent dispersability and stability to the final hybrid. The fabricated hybrid exhibited much enhanced anti-bacterial performance compared to commercial silver nanoparticles due to the combined anti-bacterial effects of CNTs and silver nanoparticles. With these superior properties, the developed surface modification process could be widely used for improving the performances of many CNT based hybrid nanomaterials in diverse applications.

The process of surface activation of CNT and silver nanoparticles deposition are schematically illustrated in Figure 2-1. The surface modification of CNTs was carried out in a multi-oxidant solution consisting of both an intercalating agent ( $\text{H}_2\text{SO}_4$ ) and oxidants ( $\text{KMnO}_4$ ,  $\text{NaNO}_3$ ) under low-power ultrasonication. Initially, the oxidation process started from the edge and surface defects of the pristine CNTs. These positions are more vulnerable to attack from the oxidants due to their incomplete  $\text{sp}^2$  carbon structures. Consequently, many oxygen-containing groups, such as phenolic, ether, carboxyl and carbonyl groups, were generated at these places. With expansion of the defect area, sulfuric acid, as the intercalating agent, started to penetrate into the inner graphitic layers of CNTs and caused deep oxidation, which generated the porous out layer with large amounts of nanoscale defects. Besides the oxidation treatment, a low-power ultrasonication was also maintained during the whole modification process to increase the surface roughness of the M-CNTs.

After the surface activation, the coating of silver nanoparticles on the surface of CNTs was carried out in a complex solution containing silver ion source ( $\text{Ag}(\text{NH}_4)^+$ ), reducing agent

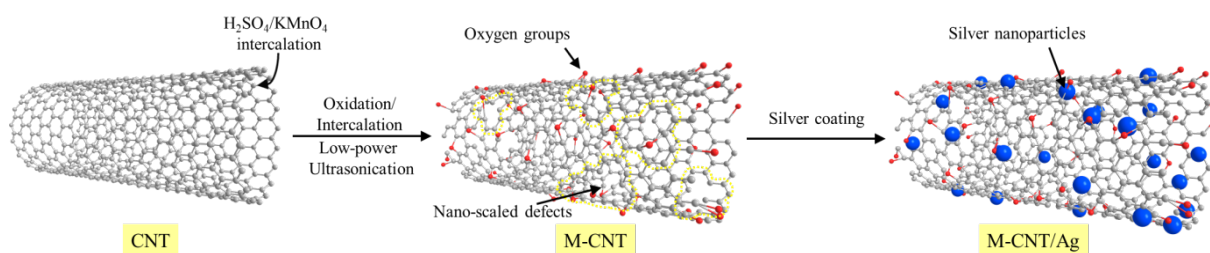


**Figure 2-1** Schematic of the multi-oxidation process of CNTs (multi-walled carbon nanotubes) and the following silver nanoparticle growth.

( $\text{Co}^{2+}$ ) and chelating agent (ethylenediaminetetraacetic acid (EDTA)). During the silver coating process, cobalt (II) ions, acting as the reducing agent, reacted with silver ions to form metallic silver nanoparticles on the surface of the CNTs. Also, due to the chelation of EDTA, the reaction between silver ions and cobalt ions is stable which can benefit for achieving highly uniform and densely packed silver nanoparticles coating layer on CNT surfaces.

### 2.1.1 Surface activation of CNTs

The multi-oxidation process was much more efficient at modifying the CNTs than traditional acid etching processes. To make a comparison, pristine CNTs were also treated by following the typical acid etching procedure reported in many publications [63,64]. Fourier-transform infrared spectroscopy (FTIR) analysis was employed to study the functional group changes on the M-CNT surface and compare the activation efficiency of different processes. As shown in Figure 2-2a, the spectrum of pristine CNTs shows some inherent characteristic peaks corresponding to oxygen-containing functional groups, such as epoxy, carbonyl and carboxyl, which most likely resulted from the production process used by the material supplier. By comparison, the spectrum of M-CNTs shows significant increases in oxygen-containing groups on M-CNT surfaces. For instance, the characteristic peaks at  $1220\text{ cm}^{-1}$  and  $1700\text{ cm}^{-1}$  corresponding to the breathing vibration of C-O and the stretching vibration of C=O from carbonyl and carboxyl groups became much more intense. A new strong and broad peak appeared in the range of  $1400\text{--}1536\text{ cm}^{-1}$ , which represented the stretching vibration of C-O. In addition, two more characteristic peaks appeared at  $2870\text{ cm}^{-1}$  and  $2960\text{ cm}^{-1}$ , due to the stretching vibration of C-H. These results indicate the successful bonding of the oxygen-containing groups on the M-CNT surface. For A-CNTs, it shows a limited increase of oxygen-containing groups compared to the pristine CNTs, such as C-O and C=O groups at  $1220\text{ cm}^{-1}$  and  $1700\text{ cm}^{-1}$ . However, the intensities of these peaks are much smaller than that of M-CNTs, indicating that the traditional acid etching process only has a weak activation effect. In addition, the multi-oxidation process has a shorter treatment time (30 min) and lower temperature ( $30\text{--}40^\circ\text{C}$ ) compared to the acid etching process, demonstrating the high modification efficiency of the multi-oxidation process.

X-ray photoelectron spectroscopy (XPS) was used to quantitatively characterize the oxidation degree and carbon/oxygen ratios (C/O) in M-CNTs and A-CNTs. As shown in Figure 2-2b, pristine CNTs show a high purity without any metal atoms detected from the XPS spectra. The C/O ratio of pristine CNTs is about 98:2, indicating the existence of small amount of oxygen and defects. Compared to pristine CNTs, O1s peaks increased significantly

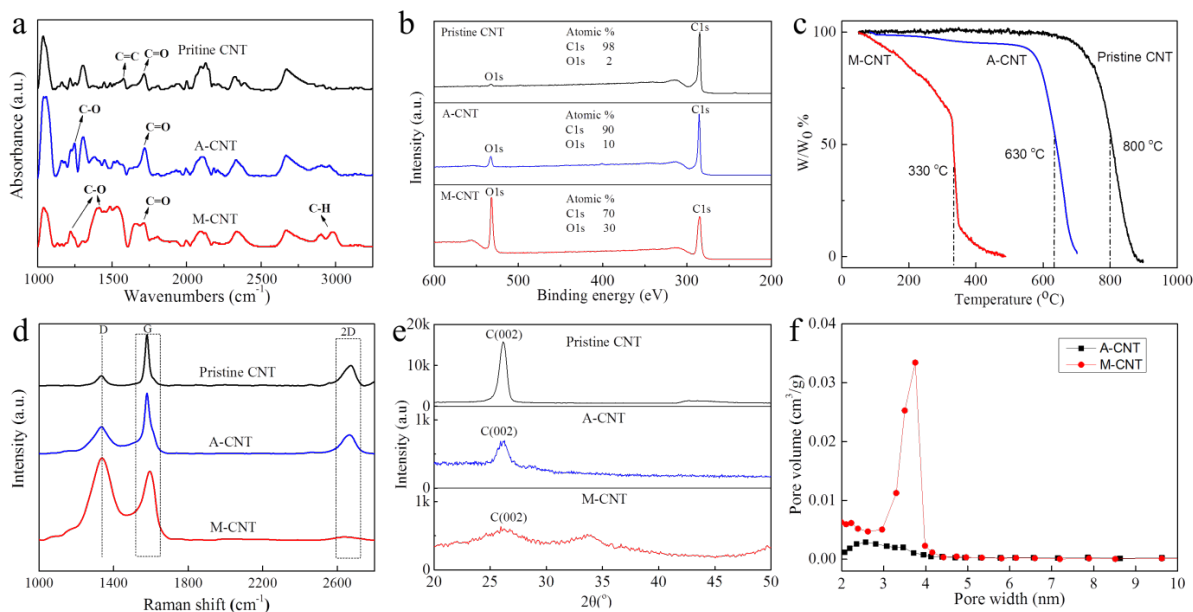


**Figure 2-2** (a) FTIR spectra of pristine CNTs, A-CNTs and M-CNTs. (b) XPS curves of pristine CNTs, A-CNTs and M-CNTs. (c) TGA curves of pristine CNTs, A-CNTs and M-CNTs. (d) Raman spectroscopy of pristine CNTs, A-CNTs and M-CNTs. (e) XRD spectra of pristine CNTs, A-CNTs and M-CNTs. (f) Pore volume distribution of pristine A-CNTs and M-CNTs.

in both M-CNTs and A-CNTs. The M-CNTs, in particular, showed the highest O1s peak intensity, and also the C1s peak of the M-CNTs became smaller and broader compared to the other two samples, indicating the bonding of sufficient oxygen functional groups. Furthermore, the C/O ratios in different samples are 98:2 (pristine CNTs), 90:10 (A-CNTs) and 70:30 (M-CNTs). Such a high ratio of oxygen in M-CNTs is essential for the homogeneous dispersion of the final hybrids due to the formation of hydrogen bonds between oxygen groups and water molecules. Thermal gravimetric analysis (TGA) was performed to show the effect of oxygen groups on the property change of CNTs. As shown in Figure 2-2c, all samples were heated from 50 to 900°C in a dry air flow with a heating rate of 20 °C/min. It has been found that the decomposition temperatures of M-CNTs and A-CNTs were decreased from 800 to 330°C and 630°C respectively when compared with pristine CNTs. The significant decrease of decomposition temperature of M-CNTs is due to the deep oxidation caused by the multi-oxidation process. Defects and oxygen-containing groups make the CNT structure less stable during heating. Moreover, as a result of burning, there were no remnants detected in all three samples, indicating that the three samples were high pure, and a high purity of the carrier materials is desirable for ensuring the best possible performance of the silver nanoparticles.

The created defects on the surface of M-CNTs act as nucleation sites and are essential to ensuring the size and uniformity of the silver nanoparticles. Therefore, it is important to analyze the size and amount of defects. Raman spectroscopy was employed to examine the change of the defect area on CNTs before and after surface modification (Figure 2-2d). The spectrum of the pristine CNTs presents a strong G peak at 1580  $\text{cm}^{-1}$  and a weak D peak around 1335  $\text{cm}^{-1}$  representing the high crystallinity of the CNT's structure and the low

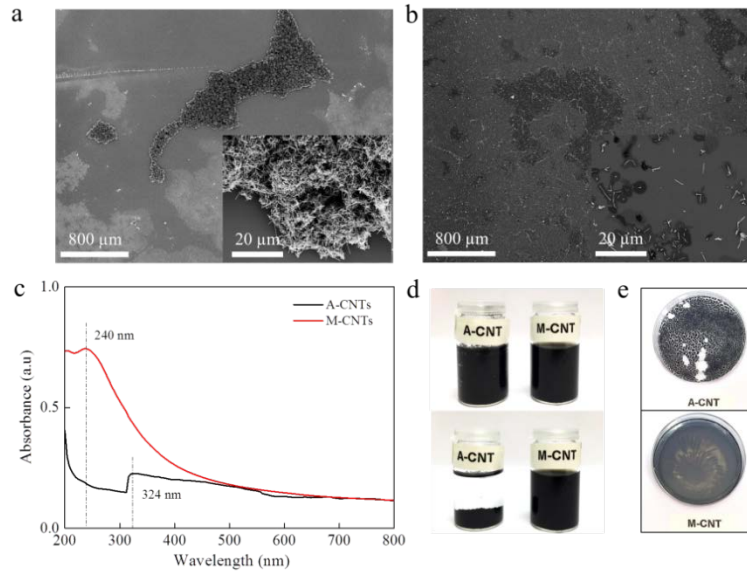


**Figure 2-3** (a-b) SEM image of A-CNTs (a) and M-CNTs (b) dispersed on the silicon chip, and the inset shows the zoom out SEM images of each sample. (c) UV-visible spectra of A-CNT and M-CNT aqueous colloids. (d) Optical images of fresh A-CNT and M-CNT aqueous colloids (left) and one week after preparation (right). (e) Optical images of deposited A-CNT and M-CNT thin films on polystyrene petri dishes.

number of defects on CNTs respectively [65]. Compared to that, the ratios of D and G band intensities ( $I_D/I_G$ ) of M-CNTs and A-CNTs increased significantly after surface modification, and M-CNTs showed the highest  $I_D/I_G$  ratio. This result means that the defect area on the surface of M-CNTs is greatly expanded due to the intercalation and deep oxidation of multi-oxidants. X-ray diffraction (XRD) analysis shows consistent results with Raman spectroscopy. As shown in Figure 2-2e, a distinct diffraction peak appeared at  $26^\circ$  is indexed as the (002) reflection of the hexagonal graphitic structure [66]. After surface activation, M-CNTs show a significantly decreased and widened graphitic peak compared to that of pristine CNTs and A-CNTs, representing a breakdown in the graphitic lattice structure in M-CNTs induced by the activation treatment. To analyze the average size of those defects, Barrett-Joyner-Halenda (BJH) pore volume and size distribution tests were carried out, and the result is shown in Figure 2-2f. Compared to A-CNTs, M-CNTs present a strong peak between 3 and 4 nm in the pore distribution curve, implying the formation of large amount of nanoscale defects with a narrow size distribution on M-CNTs. Moreover, Brunauer-Emmett-Teller (BET) surface area analysis show that the surface area of M-CNTs ( $33.5 \text{ m}^2/\text{g}$ ) is over twice that of A-CNTs ( $16.3 \text{ m}^2/\text{g}$ ) due to the created nanoscale defects.

Based on the results above, it can be concluded that the multi-oxidation process efficiently creates abundant nanoscale defects and also form large amounts of oxygen-containing groups onto the surface of CNTs. These surface modifications also result in M-CNTs having superior dispersability. Figure 2-3a-b shows the SEM images of A-CNTs and M-CNTs dispersed on the silicon chip surface respectively. It can be found that A-CNTs show a poor dispersion property and form large size bundles due to the strong Van der Waals force. As a comparison, M-CNTs show a much homogeneous dispersion on silicon surface due to the strong hydrogen

bonds formed between the M-CNTs surface and the substrate surface. Figure 2-3c exhibits the UV-visible spectra of the aqueous colloids of M-CNTs and A-CNTs. The UV-visible spectrum of M-CNTs shows a maximum at 240 nm and gradually decreased from UV to near IR. The characteristic peak at 240 nm indicates the acquisition of monodispersed M-CNT colloids [67,68]. As a control, A-CNT colloids have a very low absorbance at 324 nm in their UV-visible spectrum because of the existing CNT bundles which are less active at wavelengths between 200 and 800 nm [68]. Figure 2-3d shows the colloid stability of A-CNTs and M-CNTs. It has been found that the M-CNT colloid exhibited good stability while a precipitation occurred in the A-CNT colloid over a period of one week after preparation. Such a good stability of M-CNT colloids is attributed to the electrostatic stabilization effect of abundant oxygen functional groups on each individual M-CNT surface. In addition, the oxygen functional groups play a crucial role in determining the morphology of the deposited CNT thin films. Figure 2-3e shows the deposited A-CNT film and M-CNT film on polystyrene petri dishes. It has been found that the evaporation of water led to formation of large individual A-CNT bundles on the substrate surface. In addition, these bundles could easily be peeled off from the substrate surface, showing that the A-CNTs had poor bonding strength. M-CNTs, in comparison, formed a uniform deposition layer on the substrate surface and bonded robustly to the substrate. This is due to the strong electrostatic repulsion effect of negatively charged oxygen functional groups on the surface of M-CNTs and this appears to prevent the formation of large CNT bundles. The uniform and tightly bonded M-CNT film on a substrate has the benefits of improving contact surfaces and the binding capability that is not the case for silver nanoparticles alone and thus enhances their anti-bacterial activity [69].

Transmission electron microscopy (TEM) was carried out to understand the structural changes to M-CNTs. As shown in Figure 2-4a-b, the pristine CNTs used in this work have an average diameter of 100 nm and a small aspect ratio about 100 (Figure 2-4a). Such a small aspect ratio of CNTs has the benefit of reducing the twisting among CNTs as well as improving their dispersion. Furthermore, the pristine CNTs, as shown in Figure 2-4b, have a highly oriented structure comprising of numerous parallel graphitic layers, demonstrating the high crystallinity of the pristine CNTs. In comparison to that, some obvious morphology changes were noticed on the structure of M-CNTs. As seen from Figure 2-4c, the cross-sectional view of M-CNTs shows a sharp contrast between the porous outer layer and the tight inner layer, and the porous outer layer has an average thickness of 10 nm. This structural change to the M-CNTs was caused by the combined effect of both deep oxidation and low-power ultrasonication of the multi-oxidation process. The lattice structure close to the surface area of the M-CNTs was partly disrupted and formed small nanoscale defects due to the effect of deep oxidation. The inner graphitic layers were not affected by the modification process and still kept their original highly oriented structure, as shown in Figure 2-4d, which helped to maintain the mechanical strength of the M-CNTs. TEM images of M-CNTs are consistent with the previous material characterization results, showing a superior efficiency of the multi-oxidation process in creating nanoscale defects on CNT surfaces.

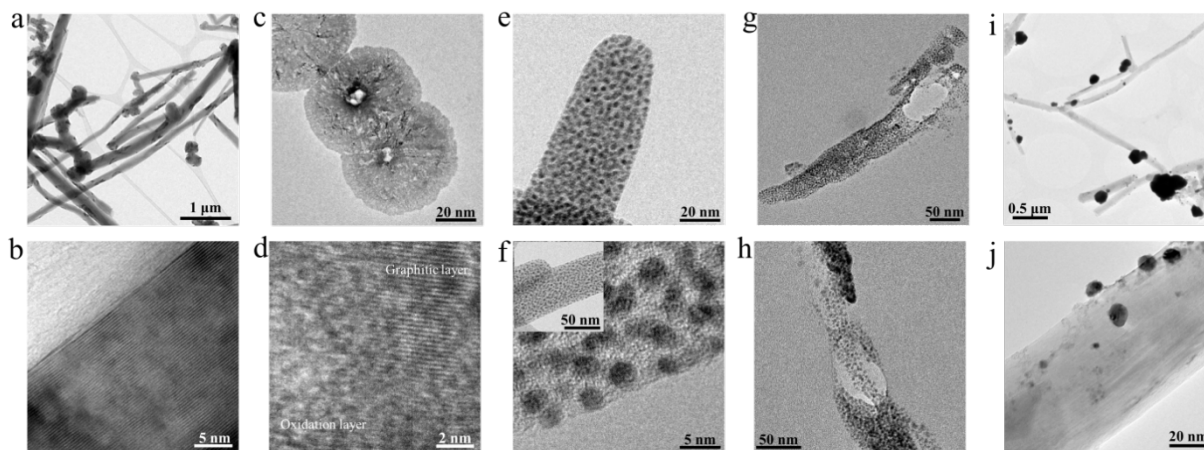


**Figure 2-4** (a-b) TEM images of pristine CNTs with different magnifications. (c) TEM cross-sectional view of M-CNTs. (d) TEM image of the graphitic lattice change of M-CNTs. (e-f) TEM images of M-CNTs carrying monodispersed silver nanoparticles with different magnifications. (g-h) TEM images of the out layer of M-CNTs carrying monodispersed silver nanoparticles. (i-j) TEM images of A-CNTs carrying large silver nanoparticles with different magnifications.

### 2.1.2 Deposition of silver nanoparticles on the activated CNTs

The growth of silver nanoparticles was carried out in a silver complex solution where a stable reaction speed was maintained to refine nanoparticle's size and geometry. Figure 2-4e-f show the morphology of M-CNTs carrying the silver nanoparticles. As seen, large amounts of monodispersed nanoparticles with a mean diameter of 3 nm were uniformly deposited around the whole M-CNT surface and formed a densely packed nanoparticle layer, and interestingly, these nanoparticles penetrated into the porous out layer of M-CNTs. After extracting the tight inner part of M-CNT, the out layer with the tremendous silver nanoparticles can still remain the original shell structure, instead of forming individual particles (Figure 2-4g-h), indicating the strong binding capability of M-CNTs to the attached nanoparticles. Furthermore, there were no detected large-sized particles or obvious agglomeration on the surface of the M-CNTs, indicating the highly uniform diameter and distribution of nanoparticles. The reason for such a good coating effect is that the large number of nanoscale defects created on the surface of M-CNTs restricted the growth of individual particles and also prevented their agglomerations. Figure 2-4i-j show the morphology of A-CNTs carrying silver nanoparticles. It was found that the surface of A-CNTs was lightly coated by a very limited amount of silver nanoparticles. In addition, the silver nanoparticles had irregular shapes and different sizes ranging from 10 nm to 200 nm. Such a poor silver coating probably resulted from insufficient nucleation sites for the growth and attachment of silver nanoparticles. These results show the importance of our developed CNT surface modification process to the uniformity of nanoparticles.

An X-ray diffraction (XRD) study was employed to identify the elementary composition of the nanoparticle layer. As shown in Figure 2-5a, the spectrum shows three new intensive peaks appearing at angles of 37.9°, 44.1°, and 64.8°. They are indexed as the (111), (200) and (220) reflections of silver's face-centered cubic (FCC) structure, implying the presence of

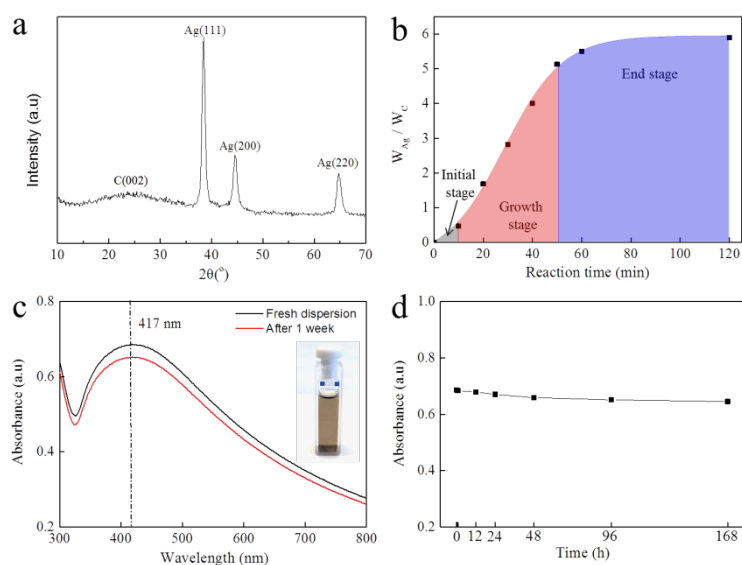


**Figure 2-5** (a) X-ray diffraction (XRD) patterns of M-CNTs carrying silver nanoparticles. (b) The change of silver weight ratios deposited on the surface of CNTs as a function of the reaction time as measured by TGA. (c) UV-visible spectroscopy of the fabricated M-CNT carrying silver nanoparticle aqueous dispersion freshly made and after one week. (d) The time-resolved UV-visible absorbance intensities of the M-CNT carrying silver nanoparticle dispersion at the wavelength of 417 nm over one week.

silver with high crystallinity [70]. Due to the use of chelating agents, the developed silver nanoparticle growth method has advantages of stable reaction speed, a steady process, and good controllability of the metallic nanoparticle size and uniformity, which is superior to many reported approaches. For example, glucose, the most common silver reducing agent for mirror fabrication, can only grow very limited amount of silver nanoparticles on the surface of CNTs. Furthermore, the generated silver nanoparticles showed irregular shapes and variable sizes ranging from 10 nm to 200 nm [71]. Such non-uniform silver growth is likely a result of the fast reaction between the silver cations and glucose. Besides using conventional glucose for reduction, previously reported silver growth methods employing, for example, sodium borohydride or dimethylamine borane species as reducing agents unavoidably lead to the generation of hydrogen gas during the reactions [72,73]. Hydrogen bubbles can take over the nucleation sites on the surface of the CNTs and interfere in the morphology and coverage ratio of silver nanoparticles.

To precisely control the size and amount of silver nanoparticles, a systematic study of silver deposition was performed by TGA analysis. Different M-CNT samples with varied silver nanoparticle growth time were collected and burnt completely in a dry air flow to record the change of silver mass ratios expressed as  $W_{Ag}/W_C$ . The expressions  $W_{Ag}$  and  $W_C$  represent the weights of silver and M-CNTs respectively. Figure 2-5b shows the change of silver mass ratio as a function of growth time. According to the curve, there was a short initial stage lasting for 10 min at the beginning of silver growth. During this stage, the reaction speed was relatively slow, possible reasons could be that most of silver and cobalt ions were encapsulated by the chelating agent (EDTA) and formed stable metal ion chelates,  $Ag^+$ -EDTA

and  $\text{Co}^{2+}$ -EDTA, respectively. The reaction speed at this stage was mainly dominated by the slow spreading and decomposition processes of metal ion chelates. After this initial stage, reactions between silver cations and cobalt cations became much more active due to the self-catalytic effect of silver. As a result, large amount of silver nanoparticles were generated and deposited onto the surface of the M-CNTs. This growth stage continued for about 40 min and the  $W_{\text{Ag}}/W_{\text{C}}$  ratio increased from 0.5 to 5. Importantly, a stable reaction speed was exhibited during this stage due to the slow decomposition of the chelated compounds. Therefore the rapid growth of silver nanoparticles is avoided and the benefit was obtaining a monodispersed nanoparticle layer. The reaction then reached a plateau after 60 minutes with a final  $W_{\text{Ag}}/W_{\text{C}}$  ratio of approximately 6 and diminished completely after prolonged reaction time due to the depletion of reactants in the solution bath. According to the calculation of silver input-output ratio, up to 70% of the silver in the solution reacted while the reduction of the remaining 30% was prevented by the chelating agents. Further prolongation of reaction time would result in no further increase in the silver mass ratio, indicating that the growth of silver nanoparticles had been completed.

Due to the strong SPR absorption of silver nanoparticles in the visible region, the dispersability and stability of the fabricated M-CNT/Ag in an aqueous dispersion was characterized by UV-visible spectroscopy. As shown in Figure 2-5c, the absorption spectra of the freshly-prepared dispersion and the same dispersion after one week exhibited similar surface plasmon absorption bands with a maximum of 417 nm. It has been reported that the exact position and shape of the SPR absorption band are strongly dependent on the particle shape and size [74]. According to the literature, the number of SPR peaks increases as the symmetry of the nanoparticle decreases, meaning that agglomeration of silver nanoparticles would lead to the increase of SPR peaks in the UV-visible spectrum [75]. Therefore, the single SPR peak in both two spectra indicates the presence of spherical silver nanoparticles with no agglomeration. Additionally, the position of SPR peak is also closely related the particle size. When silver nanoparticles aggregate, the SPR peak tends to shift towards longer wavelengths due to the increased particle size [76]. However, the SPR peak of the dispersion still showed a maximum absorption band at the wavelength of 417 nm after one week, confirming the good uniformity of the dispersion. Figure 2-5d shows the time-resolved UV-visible absorbance intensities of the M-CNT/Ag dispersion at the wavelength of 417 nm. It can be seen that the dispersion showed relatively stable SPR absorbance intensities over a week period, indicating the good stability of the dispersion.

### **2.1.3 Anti-bacterial activity of M-CNT/Ag**

Due to the intrinsic anti-bacterial property of Ag NPs and large surface area of M-CNT, the fabricated M-CNT/Ag was used for killing bacteria. The anti-bacterial activity of M-CNT/Ag was compared to commercial Ag NPs with an average size of 5 nm by monitoring the respective growth and time killing assay of *E.coli* bacteria. Figure 2-6a shows the optical density (OD) changes of Ag NPs and M-CNT/Ag as a function of growth time respectively. Blank samples without any anti-bacterial agents served as the control group. It was found that the control group was more opaque compared to the other two samples,

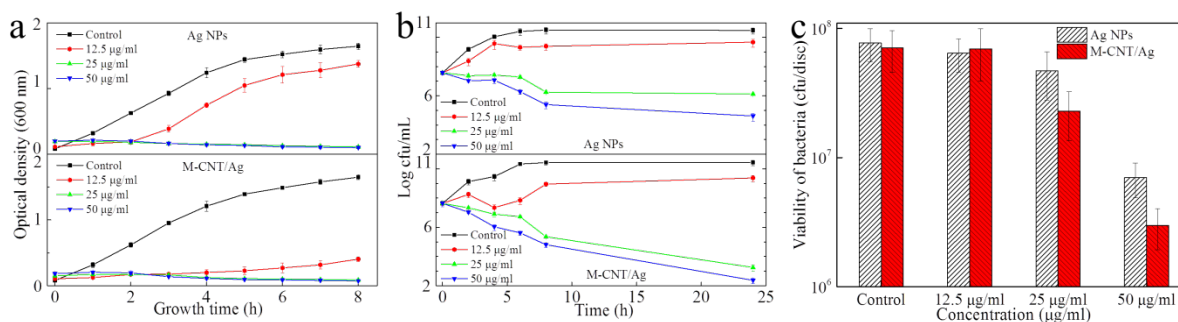


**Figure 2-6** (a) The optical density (OD) changes of Ag NPs and M-CNT/Ag as a function of growth time respectively. Ag NPs and M-CNT/Ag with different concentrations (12.5 µg/ml, 25 µg/ml and 50 µg/ml) were measured respectively. (b) The time killing assay of *E. coli* in the presence of Ag NPs and M-CNT/Ag with different concentrations (12.5 µg/ml, 25 µg/ml and 50 µg/ml). (c) Anti-bacterial activities of Ag NPs and M-CNT/Ag with different concentrations (12.5 µg/ml, 25 µg/ml and 50 µg/ml) against *E. coli* biofilm. Blank samples without any anti-bacterial agents acted as the control group in all of the measurements.

indicating normal growth of the bacteria. Compared to that, the transparency of the culture medium was consistent for Ag NPs at high concentrations ( $\geq 25$  µg/ml), showing the strong bacteriostatic effect of silver nanoparticles. However, the bacterial growth at a low concentration of 12.5 µg/ml exhibited a relatively similar growth pattern to the control group, demonstrating a very weak bacteriostatic effect (top image of a). A possible reason is that Ag NPs tend to form agglomeration which decreased the contact areas between the silver nanoparticles and bacteria and made the bacteriostatic effect of Ag NPs less obvious at low concentrations. On the other hand, M-CNT/Ag at high concentrations ( $\geq 25$  µg/ml) also exhibited very strong bacteriostatic effect to the growth of bacteria, as shown in the bottom image of Figure 2-6a. Interestingly, M-CNT/Ag at a lower concentration of 12.5 µg/ml showed a much more restricted growth of bacteria within the first 8 h than the Ag NPs. The bacteria growth speed of within the first 8 h was very slow, indicating a higher bacteriostatic effect of M-CNT/Ag at low concentrations.

Figure 2-6b depicts the time killing assay of *E. coli* in the presence of Ag NPs and M-CNT/Ag. Herein, both Ag NPs and M-CNT/Ag did not show obvious bactericidal effects against *E. coli* at a low concentration of 12.5 µg/ml. Nevertheless, the viability of the bacteria still decreased compared to the control sample due to silver's inhibitory effect on bacterial growth. It has also been found that M-CNT/Ag at the concentration of 12.5 µg/ml was more effective than Ag NPs in the initial 2-6 hours. This is due to the fact of large contact areas between the bacteria and the M-CNT/Ag that caused immediate damage to the bacteria and thus slow down the initial growth speed. With continued growth of bacteria, the inhibitory effect of M-CNT/Ag became less obvious because the bacteria outnumbered the available M-CNT/Ag. The inhibitory effect at low concentrations was not detected from Ag NPs. In the case of high concentrations (25 µg/ml and 50 µg/ml), the bactericidal effect of M-CNT/Ag can be clearly observed with the increase of interaction time between the bacteria and M-CNT/Ag, where the bacteria were neutralized in a more linear fashion. For Ag NPs, it also showed bactericidal activity at high concentrations but the overall bacterial killing rate and

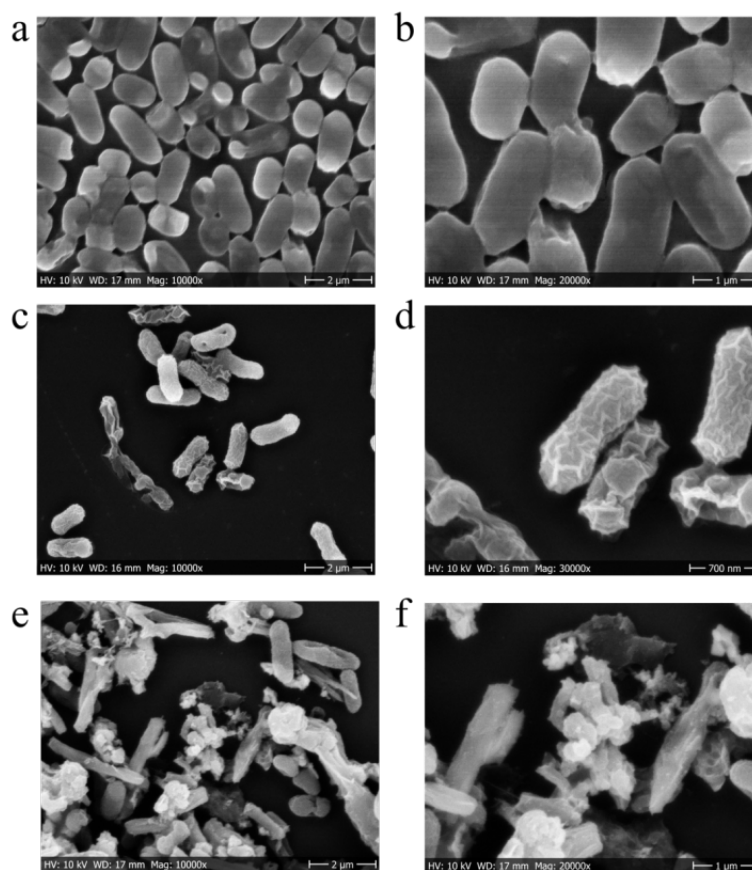


**Figure 2-7** SEM images showing the structural damages of *E.coli* biofilm cells treated by Ag NPs and M-CNT/Ag respectively. (a-b) The morphology of *E.coli* biofilm cells from the control group. (c-d) The morphology of *E.coli* biofilm cells treated by Ag NPs (50  $\mu\text{g/ml}$ ). (e-f) The morphology of *E.coli* biofilm cells treated by M-CNT/Ag (50  $\mu\text{g/ml}$ ).

final bacterial viability were much less than M-CNT/Ag. Moreover, it has been noticed that the bactericidal effect of Ag NPs reached a threshold after 8 hours, meaning that the bacterial killing speed of Ag NPs was almost in a state of equilibrium with the bacterial growing speed. These results show that the M-CNT/Ag hybrids have stronger anti-bacterial activity and better reliability than Ag NPs at all concentrations.

Anti-bacterial activities of Ag NPs and M-CNT/Ag against *E.coli* bacteria on biofilm were also evaluated, and the results are shown in Figure 2-6c. It was found that both Ag NPs and M-CNT/Ag at a low concentration of 12.5  $\mu\text{g/ml}$  did not show obvious bactericidal effects against bacteria on biofilm due to the strong resistance of biofilm bacteria to anti-bacterial agents. For higher concentrations (25  $\mu\text{g/ml}$  and 50  $\mu\text{g/ml}$ ), the viability of the bacteria treated by M-CNT/Ag was only half that for Ag NPs, showing the superior anti-bacterial performance of M-CNT/Ag hybrids compared to Ag NPs. Scanning electron microscope (SEM) images (Figure 2-7) show the structural damage of *E.coli* bacteria treated with Ag NPs and M-CNT/Ag respectively. As seen in Figure 2-7a-b, *E.coli* bacteria from the control group showed intact morphology and the cells maintained a normal physicality. In contrast, the treatment of Ag NPs (50  $\mu\text{g/ml}$ ) caused obvious shrinkage of the cell walls (Figure 2-7c-d) due to the lysing effect of silver. For M-CNT/Ag (50  $\mu\text{g/ml}$ ), it can be clearly observed that most of the cell walls were completely destroyed and the ratio of damaged/dead *E.coli* was

much higher than that of Ag NPs (Figure 2-7e-f). This result shows that the very strong anti-bacterial activity of M-CNT/Ag is actually attributed to the combined effect of deposited silver nanoparticles and M-CNTs. For example, the interaction of the sharp edges of M-CNTs and rough surfaces with the bacteria cell wall resulted in obvious physical damage to cell membranes and led to the loss of bacterial membrane integrity. The silver nanoparticles on the surface of M-CNTs then caused irreversible damage to the proteins, DNA and lipids after exposure to the bacterial cytoplasmic matrix. Moreover, the significant amount of oxygen functional groups on the M-CNTs was able to generate large amount of reactive oxygen species (ROS); which induced oxidative stress onto the bacteria thereby lysing them. As a whole, the membrane and oxidative stresses induced by M-CNTs, together with the lysing effect of silver nanoparticles, significantly enhanced the anti-bacterial activity of the M-CNT/Ag hybrids.

#### **2.1.4 Conclusion**

In this paper, a new surface modification process was developed to modify the chemically inert graphitic surface of CNTs for close bonding with silver nanoparticles. The multi-oxidation process is capable of creating a porous out layer with abundant nanoscale defects and bond large amounts of oxygen-containing groups onto the surface of the CNTs. The M-CNTs show excellent dispersability and stability in water without using any surfactants, Monodispersed silver nanoparticles with an average size of 3 nm were closely bonded on the surface of M-CNTs without any obvious agglomerations. Due to the combined anti-bacterial effects of M-CNTs and silver nanoparticles and good reliability of the hybrid nanostructures, the fabricated M-CNT/Ag exhibited greatly enhanced anti-bacterial activity compared to commercial silver nanoparticles. With these superior properties, the developed surface modification process could be widely used for improving the performances of many CNT based hybrid nanomaterials in diverse applications, such as catalysts, optical spectroscopies, conductive inks, water sterilization, and biosensors.

## **2.2 Covalent functionalization of graphene oxide for cement reinforcement**

Cement-based concrete is the most common and widely used building and construction material in the world. Although concrete itself is relatively durable when used under the mild environments, the brittle nature caused by the porous and vulnerable structure of concrete still limits its life-time performance in many high-strength required applications. Traditional strategies to reinforce the mechanical strength of concrete are to utilize various fibrous materials with high intrinsic tensile strength, such as steel bars[77], steel fibers[78], carbon fibers[79], polymer fibers[80–82], and glass fibers[83,84]. These materials have shown good performance on prevention of large crack growth and stabilizing the concrete against shrinkage. However, their applications in concrete are facing some challenges. For example, steel bars suffered the corrosion problem caused by moisture and ionic immigration. Polymer

fibers have good tensile strength but poor reliability. Carbon fibers could significantly decrease the workability of the fresh cement paste and also cost a lot in economy, and glass fibers can improve the early strength but have no obvious effect on the ultimate strength of the concrete due to their reaction with cement hydration products. Most importantly, the reinforcement of concrete via fibrous materials suffered a common problem which is that the fibers can only replace large cracks with many micro-cracks but fail to stop crack initiation at nanoscale. Nanoscale pores with a diameter less than 100 nm contribute to most of the pore volume in concrete and play a crucial factor in the mechanical strength of concrete[85]. It is essential to seek a method that can significantly improve the ultimate strength of concrete through modification of concrete nanostructure.

Recent development in nanotechnology has presented new opportunities to address the issue. Many different nanomaterials have been synthesized and employed as the reinforcing materials to fabricate high performance concretes (HPC). For example, silica nanoparticles can significantly accelerate the hydration process of cement due to their strong pozzolanic activity and large surface areas, and therefore, the concrete's strength can be enhanced at very early ages[86,87]. However, the reinforcing effect of silica nanoparticles becomes less obvious with the progress of the hydration process, especially at the later age, due to their reaction with cement hydration products. Carbon nanotubes (CNTs) are also potential candidates for making HPC. Comprising of a  $sp^2$  bonded hexagonal graphitic structure, CNTs possess extraordinary mechanical properties with tensile strength in the range of hundreds of GPa and Young's modulus on the order of TPa and also large surface areas[88]. Therefore, CNTs can in theory strongly reinforce the concrete structure at the nanoscale by increasing the amount of high stiffness calcium silicate hydrates (C-S-H) and decreasing the porosity. However, there are some major challenges associated with the incorporation of CNTs in concrete, such as poor dispersion, weak bonding, and low workability. These challenges could strongly decrease the reinforcing efficiency of the CNTs and limit the application of CNTs in the field of HPC.

Recently, graphene oxide (GO), a two-dimensional (2D) carbon nanomaterial, has the same hexagonal graphitic structure as CNTs and demonstrates a great potential on the application of cement reinforcement due to many of its extraordinary properties, such as large surface area, ultrahigh strength and bulk production[89,90]. Importantly, GO contains large amounts of oxygen groups covalently bonded on its basal planes and edges, which play a crucial factor during the reinforcement. The oxygen groups could form hydrogen bonds with water molecules and therefore dramatically improve GO's dispersion in water. The good dispersability of GO would benefit the mixing process of GO with cement paste. Also, the oxygen groups are negatively charged and can be absorbed by the positively charged calcium ions from cement paste due to their strong electrostatic attraction. The strongly physical and chemical interaction behaviors between GO and C-S-H greatly enhance the interface bonding strength from nanoscale and lead to an improved ultimate strength of concrete. However, our previous study shows that the dispersability and bonding ability of GO in cement paste are contradictory with each other. The strong attraction between GO and calcium cations can cause the immediate coating of GO on the unhydrated cement particles and lead to the formation of big clusters during the mixing, which can significantly decrease the workability

and hydration degree of the fresh cement paste and affect the ultimate strength of concrete. On the other hand, using any surfactants to improve the workability of the cement paste could prevent the contact between GO and C-S-H and lead to much decreased interface interactions. Therefore, it is essential to modify the chemical structure of GO to meet the requirements for both good workability and high mechanical strength.

In this section, a special surface functionalized GO (FGO) was employed as the reinforcing agent to improve the strength of the Portland cement mortar. The key benefit of FGO lies in its ability to form covalent bonds with C-S-H whilst having minimum effect on the workability of mortar paste. To achieve this goal, the original negatively charged oxygen groups of GO were functionalized by positively charged amino groups which could significantly decrease the electrostatic attraction of calcium cations and prevent the cluster formation during the mixing. Also, the amino groups are bonded together with silane groups that are highly reactive with C-S-H. Therefore, strong covalent bonds are able to form between FGO and C-S-H during the hydration process. In addition, to maximize the reinforcing effect of FGO, the whole surface of FGO was coated by an amorphous silica layer which could trigger a fast hydration of cement particles surrounding FGO at the early age. The close binding between FGO and the ambient can effectively stop crack initiation at the interface areas. Mechanical tests show that the mortar containing of 0.15 wt% FGO exhibits significant increases of 22% and 44% on flexural and compressive strength respectively after curing for 7 days. The strength development curves as a function of time also show that FGO has a strong reinforcing effect to the mortar’s strength both at the early age and the late age due to the hydration accelerating effect and the physical nano-reinforcing effect of FGO.

The FGO functional groups and its interaction mechanism with C-S-H of cement are schematically illustrated in Figure 2-8. As shown, the original GO flakes contains large amounts of oxygen functional groups which offer high chemical reactivity of GO with different functional agents. To address the strong coagulation issue between oxygen groups and calcium ( $\text{Ca}^{2+}$ ) ions[91], we utilize silane coupling agents terminated with amino groups as functional agents which can form covalent bonds with oxygen groups of GO upon catalysis. The protection of positively charged amino groups could minimum the strong electrostatic interaction between GO and  $\text{Ca}^{2+}$  ions, and therefore, decrease the adverse effect of GO to the

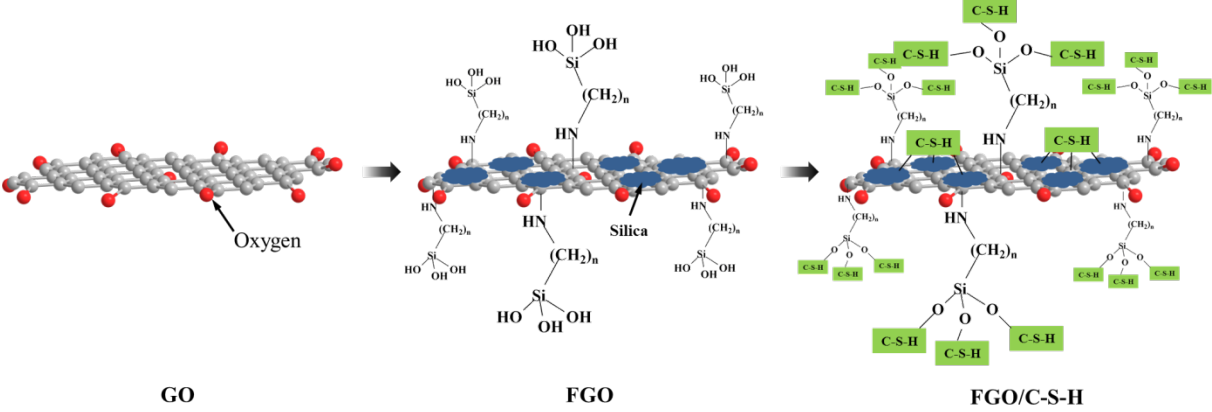


**Figure 2-8.** The sketch of the FGO functional groups and its interaction mechanism with C-S-H of cement

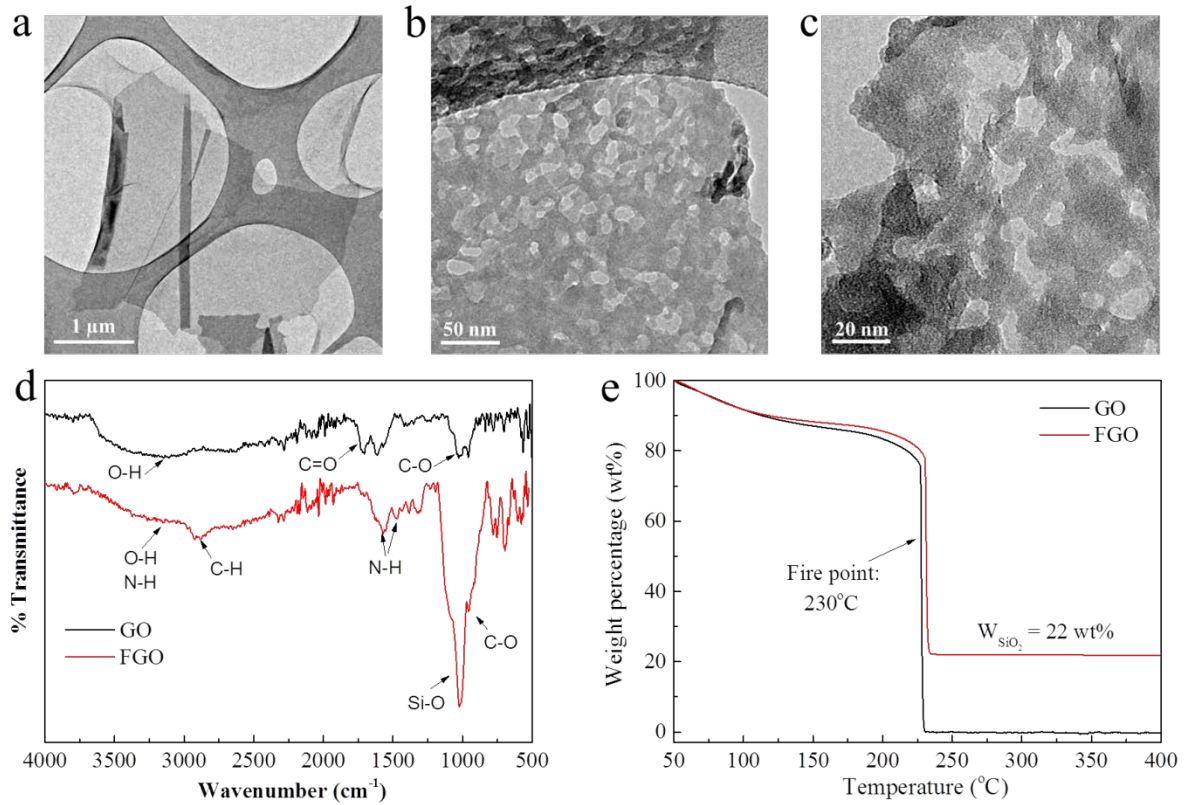


**Figure 2-9.** (a) TEM image of GO. (b-c) TEM images of FGO at different magnifications. (d) FTIR spectra of GO and FGO. (e) TGA spectra of GO and FGO.

workability of cement paste. On the other side, the terminated three silane groups are highly reactive under alkali environment, which can participate in the formation of C-S-H crystals during the cement hydration process. In addition, to further improve the interaction strength between GO and cement hydration products, the surface of GO was also functionalized with a layer of amorphous silica. The amorphous silica can quickly react with calcium hydroxide to form complex composites, which would facilitate the fast growth of C-S-H crystals surrounding FGO flakes, and consequently, reach the target of reinforce cement strength from the nanoscale level. Also, the presence of amorphous silica can accelerate the hydration process and improve the early strength of cement.

### 2.2.1 The morphology and composition of FGO

TEM analysis gives a visual understanding about the morphology change of GO before and after functionalization. Pristine GO flakes (Figure 2-9a) have a lateral size about 3  $\mu\text{m}$  together with a smooth surface. Differently, FGO (Figure 2-9b-c) shows a highly rough surface which was induced by the deposition of the amorphous and porous silica layer. The porous silica deposition layer of FGO can significantly increase the contact area with the cement hydration products and improve the interaction strength between FGO and C-S-H. Previous studies showed that silica coating layer are usually fragile and can easily separate from the attaching substrates[92]. However, in this study, we did not detect the existence of any individual silica particles. The strong adhesion between the amorphous silica layer and

GO flakes is attributed to the covalent bonding of silane coupling agents, which prevented the generation of small silica debris. The amorphous silica layer would act as nucleation sites for the growth of C-S-H crystal surrounding FGO flakes to reinforce cement strength from nanoscale level.

The comparison of the FTIR spectra of GO and FGO shows the functional group change before and after functionalization (Figure 2-9d). Pristine GO shows characterizing peaks of oxygen groups at  $1025\text{ cm}^{-1}$ ,  $1730\text{ cm}^{-1}$ , and  $3410\text{ cm}^{-1}$ , corresponding to epoxy (-C-O), carboxyl (-C=O), and hydroxide (-OH-) groups respectively[93]. After functionalization, several obvious changes were noticed from the spectrum of FGO. The most important change is the appearance of the strong Si-O vibrational peak at  $1085\text{ cm}^{-1}$ , which was originated from both the silane coupling agents and the amorphous silica layers[92]. The other emerging peaks shown on the FGO spectrum are located at  $1578\text{ cm}^{-1}$  and  $1517\text{ cm}^{-1}$ , representing the bending vibration of N-H groups from silane coupling agents. Together with the disappearance of carboxyl groups located at  $1730\text{ cm}^{-1}$ , we can conclude that the oxygen groups of GO flakes were successfully functionalized by the amino groups. There are also some other evidences that proved the presence of silane coupling agents in FGO. For example, the peak located at about  $2949\text{ cm}^{-1}$  is typical of C-H stretching vibration, which is originated from the silane coupling agents. The overlap of the secondary amine groups ( $3000\text{ cm}^{-1}$ ) with hydroxide groups led to the right shift of the broad peak on FGO spectrum originally located at  $3410\text{ cm}^{-1}$ .

The comparison of TGA spectra between GO and FGO show the weight percentage of the amorphous silica in FGO (Figure 2-9e). To calculate the relative amount of amorphous silica in FGO, both dried GO and FGO powders were heated from  $50$  to  $400^\circ\text{C}$  in a dry air flow with a heating rate of  $20^\circ\text{C}/\text{min}$ . The fire point of GO in air was detected to be around  $230^\circ\text{C}$ , which is much lower than the pure graphite (about  $600^\circ\text{C}$ ). The reason for the lower decomposition temperature of GO is the presence of large amount of oxygen groups[94]. As a result of burning, there were no remnants detected in GO, indicating the high purity of the fabricated GO flakes. For FGO, the fire point of GO is also located at  $230^\circ\text{C}$ , indicating that the amorphous silica layer on the surface of FGO has a porous structure. Such porous and rough silica coating layer is desirable for improving the interaction strength between FGO and cement hydration products. After burning, the weight percentage of remnants is about 22 wt%, showing that FGO contains about 22 wt% of highly reactive amorphous silica, which can significantly improve the early strength of cement paste.

### 2.2.2 Workability study

Although GO flakes show excellent dispersability and stability in neutral aqueous solution, it does not mean that GO can also remain such advantages in cement paste. To visualize the dispersion of GO and FGO in cement paste, we simulated the fresh cement paste environment by using calcium hydroxide ( $\text{Ca}(\text{OH})_2$ ) solution which exists extensively in cement paste at the beginning of the hydration process. As shown in Figure 2-10a, the left beaker contains pure GO suspensions in calcium hydroxide solution, which shows big clusters of GO. The formation of GO clusters in calcium hydroxide solution is due to the coagulation effect of calcium ions which can quickly replace the original hydrogen bonds between GO and

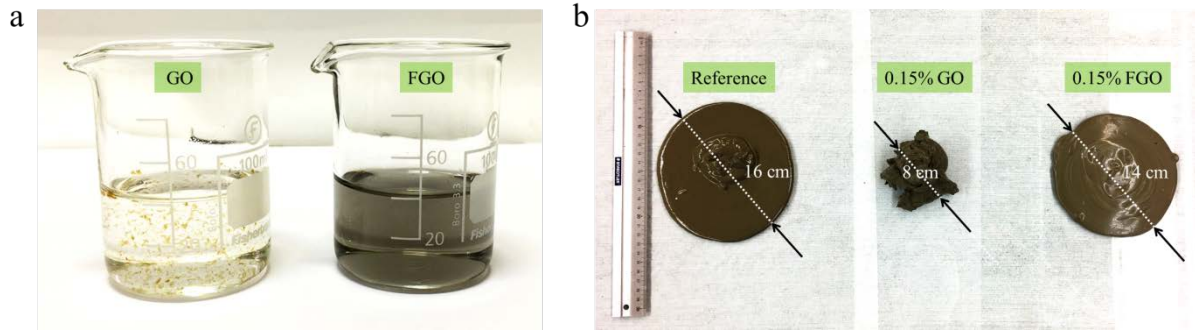


**Figure 2-10.** (a). Optical image of GO and FGO dispersion in calcium hydroxide solution. (b). Slump tests of standard reference cement mortar, and 0.15 wt% GO and FGO reinforced cement mortar samples.

surrounded water molecules and form stable complexes. Previous studies show that the coagulation of GO can decrease the concentration of calcium ions in the fresh cement paste, and subsequently leads to a retardation effect [95]. Differently, due to the protection of the functional layer, FGO shows a much improved dispersability in calcium hydroxide solution without the detection of any agglomerations. Such excellent dispersability of FGO in calcium hydroxide solution can enable a homogeneous dispersion of FGO in cement paste and reach the target of reinforce cement strength at nanoscale level.

Slump tests were carried out on a glass substrate to study the effects of GO and FGO to the workability of fresh cement paste (Figure 2-10b). Compared to the large round shape of the reference cement paste with an average diameter of 16 cm, the adding of 0.15 wt% GO significantly increased the viscosity of the fresh cement paste and made it completely lose the workability. Based on the above dispersability study of GO in calcium hydroxide solution, it can be speculated that the significantly increase of viscosity was induced by the rapid formation of GO/cement particle agglomerations which trapped large amounts of free water molecules inside. Of course, using surfactants and water reducing agents can assist the dispersion of GO in cement paste and improve the workability[85]. However, the surfactant layer can prevent the connection between GO and cement particles and lead to a retardation effect[96]. The use of surfactant would also add extra cost to the constructions. As a comparison, the adding of same amount of FGO does not have obvious decrease to the workability of fresh cement paste which still remained a good fluidity (14 cm). This was attributed to the minimized interaction strength between FGO and calcium hydroxide. Compared to the common strategies of using surfactants or water reducing agent to assist the dispersion of nanomaterials, the developed FGO in this study shows great advantages.

### 2.2.3 Mechanical strength

Figure 2-11a-b shows the effect of varied FGO weight percentages to the flexural and compressive strength of mortar respectively after curing for 7 days. Compared to the standard reference, both the flexural and compressive strength of FGO reinforced cement mortar increased significantly with the increase of the weight percentage of FGO. When the adding amount of FGO reaches to 0.15 wt%, the cement mortar shows the maximum improvement on both flexural (8.3 MPa) and compressive strength (49.4 MPa), which are about 22% and

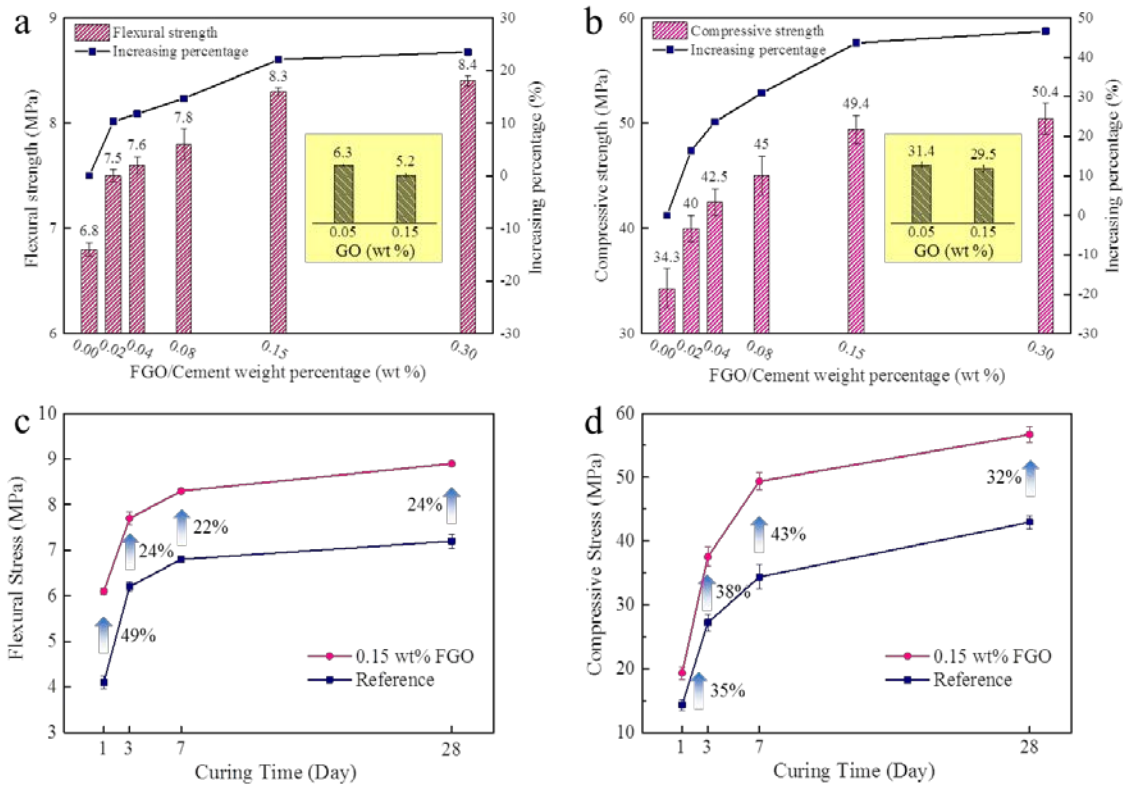


**Figure 2-11.** (a-b) The change of flexural (a) and compressive strength (b) at 7 days as a function of FGO weight percentages. The inserts show the flexural and compressive strength of cement mortar reinforced by GO with weight percentages of 0.05 and 0.15 wt%. (c-d) The flexural (c) and compressive strength (d) of cement mortar reinforced by 0.15 wt% FGO as a function of curing days.

44% more than the standard reference. Subsequent increase of the weight percentage of FGO above than 0.15 wt% did not lead to further improvement on the mechanical strength of mortar. Therefore, for the economic and workability purposes, the FGO weight percentage of 0.15 wt% was employed as the optimized adding proportion in this study.

However, GO reinforced cement mortar shows contrary mechanical performance to that of FGO (the inserts of Figure 2-11a-b). The mechanical strength of GO/cement mortar decreased with the increase of GO weight percentage. For 0.15 wt% GO/cement mortar, its mechanical strength is even lower than the standard reference. The greatly reduced mechanical performance of cement mortar is due to the combined effect of retardation caused by the oxygen functional groups of GO flakes as well as the poor dispersion induced by low workability.

The reinforce effect of FGO on both the early and ultimate strength of cement mortar was also studied in Figure 2-11c-d. The flexural and compressive strength of cement mortar reinforced by 0.15 wt% FGO were measured after different curing days. From the results, it can be found that the flexural and compressive strength of cement mortar after curing for 1 day improved 49% and 35% more than the standard reference, showing an obvious acceleration effect to the cement hydration. For the ultimate strength (after 28 days), the

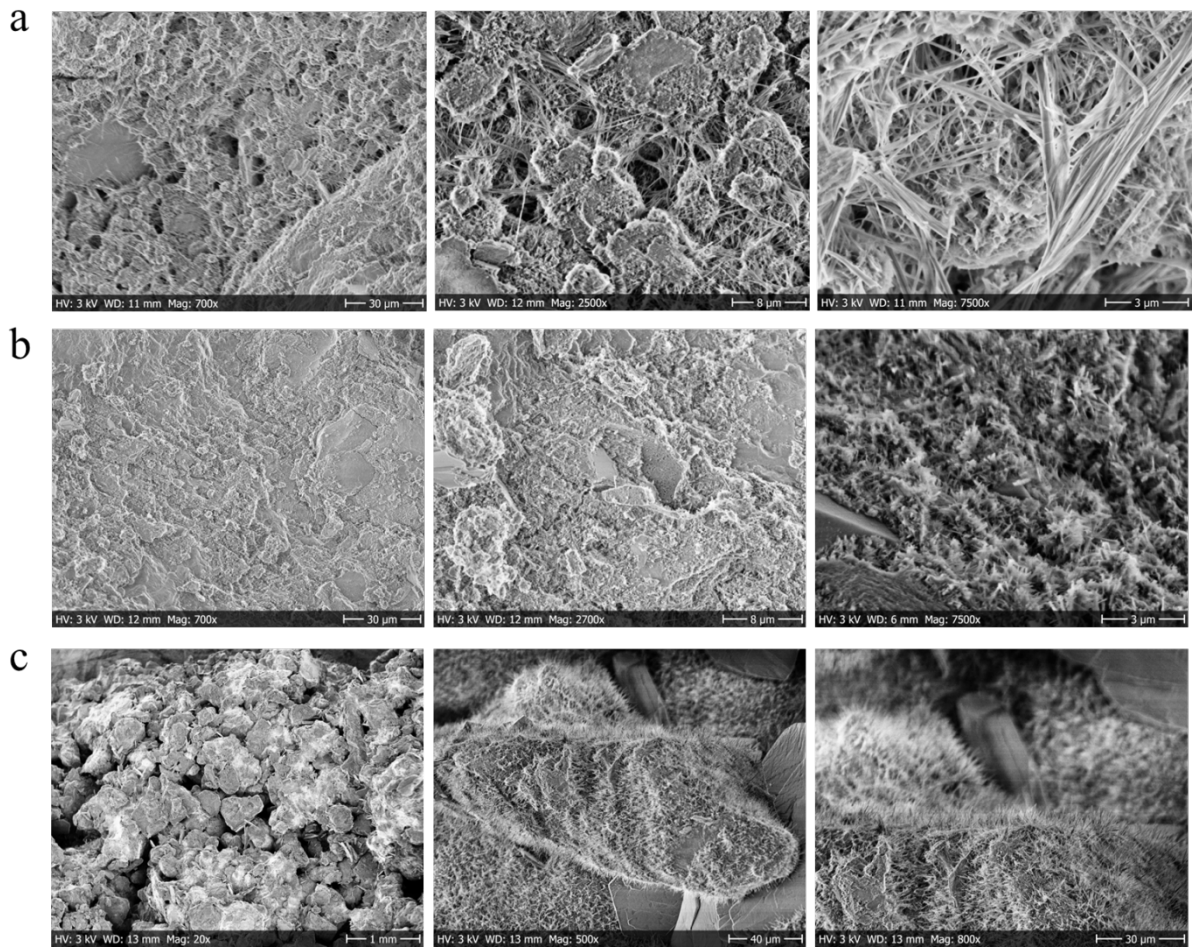


**Figure 2-12.** SEM images of microstructures of different cement mortar samples. (a) Standard reference. (b) 0.15 wt% FGO reinforced cement mortar. (c) 0.15 wt% GO reinforced cement mortar.

0.15 wt% FGO reinforced cement mortar shows improvement about 24% and 32% on the flexural and compressive strength respectively. These results declare a strong reinforce effect of FGO on both the early and ultimate strength of cement mortar. The improvement of early mechanical strength is mainly due to the acceleration effect of the amorphous silica coating layers on the surface of FGO[87], and the strong bonding between FGO and the cement hydration products at nanoscale also leads to robust mechanical strength at the late stage.

## 2.2.4 Microstructure analysis

To understand the reinforcing mechanism of FGO to cement mortar, morphology analysis of different samples, including standard reference, 0.15 wt% FGO and GO reinforced cement mortar (curing for 7 days) were performed by SEM. Figure 2-12a-b show the SEM images of reference sample and FGO reinforced cement mortar at different magnification ratios. The standard reference sample shows a porous structure which contains large amounts of needle-like structures. The needle-like structures formed a network throughout the inside of the sample and acted as the binding agent to provide mechanical strength to the cement mortar. Compared to that, 0.15wt% FGO reinforced cement mortar sample shows obvious differences

on the microstructures. From Figure 2-12b, it can be found that the sample became much denser and the average size of the needle-like crystal decreased significantly from microscale to nanoscale compared to that of standard reference. Such results show a strong refinement effect of FGO to the cement hydration products. The refinement of microstructure is also one of the major reasons for the enhanced mechanical strength of cement mortar.

The microstructure of FGO reinforced cement mortar was also compared with the case of adding 0.15 wt% of GO (Figure 2-12c). It has been found that the adding of GO led to the formation of big clusters and large voids due to the agglomeration of GO flakes with cement particles as well as the significantly decrease of working ability of cement paste. Large amounts of free water were trapped inside the clusters and lead to a poor hydration degree of cement particles. As a consequence, the 0.15 wt% GO reinforced cement mortar shows a poor mechanical strength that is even lower than the standard reference.

### **2.2.5 Conclusions**

In this study, a special amino functionalized GO with amorphous silica coating was employed to reinforce microstructures of the Portland cement mortar. The FGO reinforced cement mortar shows great advantages over many other nano-reinforcing materials, like CNTs and silica nanoparticles. i) Good dispersability. FGO can be easily and homogeneously dispersed into the cement paste without the assist of any surfactants, ii) Excellent workability. The functionalization of amino groups can effectively decrease the electrostatic attraction between the oxygen groups of GO and calcium ions and improve the workability of fresh cement paste. iii) Robust mechanical strength. Mechanical tests at 7 days show that the flexural and compressive strength of cement mortar increased about 22% and 44% respectively compared to the reference sample. iv) Accelerating cement hydration. The presence of amorphous silica in FGO can accelerate the hydration of cement and improve the early strength of cement mortar. With up to 40% increased cement early and ultimate strength due to the incorporation of FGO, Fast demolding and manufacture of lighter, slimmer constructions become highly possible, which give major competitive advantages in many applications when the commodity demand is lower and expensive transport costs are kept down. The decreased consumption of cement would also result in a reduction of CO<sub>2</sub> emissions.

## **2.3 Covalent functionalization of GBF for improving its cooling property.**

Integration and power density of microelectronic systems have been continuously increasing for decades. Efficient systematic thermal management solutions are an immediate requirement to dissipate the large amount of heat generated by the integrated chips and devices. Aiming for high thermal conductive, cost-effective and eco-friendly processes, intensive efforts have been put into the research of novel thermal management materials in both academia and industry during recent years. Among all the alternatives, graphene is one

of the most inspiring materials that may provide potential solutions to these technological barriers. Composed of one or few atomic layers of  $sp^2$ -bound hexagonal carbon lattice, phonon transfer inside graphene becomes extremely efficient, which lead to an outstanding in-plane thermal conductivity of about 5800 W/mK. Consequently, different approaches of utilizing graphene for heat dissipation have been investigated and reported in literature. For example, single-layer graphene sheets fabricated from chemical vapor deposition was transferred onto the top surface of hotspots and acted as heat spreader which showed certain decrease of the working temperature on active devices[97]. However, this approach has some limitations including low transfer efficiency, complexity and relatively high costs. Graphene/polymer composites have also been fabricated and utilized for thermal management[98]. However, the thermal conductivity values of the composites are very limited due to the large phonon boundary scattering of individual graphene sheets.

Instead of using single layer graphene or graphene/polymer composites, a special free-standing graphene based film (GBF) was fabricated for thermal management of power devices in the current thesis work. The GBF is composed of horizontally aligned reduced graphene sheets made by chemical exfoliation. This aligned microstructure can offer the film with many advantages, including good flexibility, strong mechanical strength, and particularly, high in-plane thermal conductivity. The extraordinary mechanical and thermal properties of the GBF facilitate it as the heat spreader to dissipate heat in the x-y direction.

The extraordinary thermal and mechanical properties show great potentials of GBFs as heat spreader for cooling power devices. However, there are still some challenges that could limit its heat dissipating performance during the realistic application, including a poor thermal coupling between free-standing GBF and device surfaces and high thermal contact resistance caused by mismatching of surfaces and roughness. In order to address these challenges, the surface of the GBF which contacts with device surfaces is functionalized with a silane coupling agent. As a small molecule, the silane coupling agent could both react with the oxygen functional groups located at the plane and the edge of graphene sheets, and also form covalent bonds with silicon dioxide or metal oxide surfaces. As a result, molecular bridges could be built between the GBFs and the device substrates, and thus improve the heat transfer efficiency from the power devices.

Figure 2-13a-c show the schematics of preparing functionalized GO (FGO) and the bonding mechanism of GBF on the silica substrate surface. The preparation of FGO is realized via the condensation reaction of the carboxyl groups of GO and the amino groups of (3-Aminopropyl)triethoxysilane (APTES) under the catalyst of dicyclohexylcarbodiimide (DCC). The reaction would result in the formation of covalent bonds between GO and APTES and further functionalized GO with active silane groups. Therefore, FGO, as the binding material between GBF and the silica substrate, can be considered as an amphiphilic molecule which consists of hydrophilic parts (silane groups) and hydrophobic parts (graphene domains). The silane groups of FGO can cross-link with each other, and also react with the amorphous silica layer of the substrate to build covalent silicon-oxygen bonds whilst the graphene domains of FGO can bind strongly with the surface of GBFs via  $\pi$ - $\pi$  stacking.

The thermal evaluation device was integrated with micro Pt-based heating resistors as the hotspot and temperature sensors, as shown in Figure 2-13d, acting as a simulation platform of

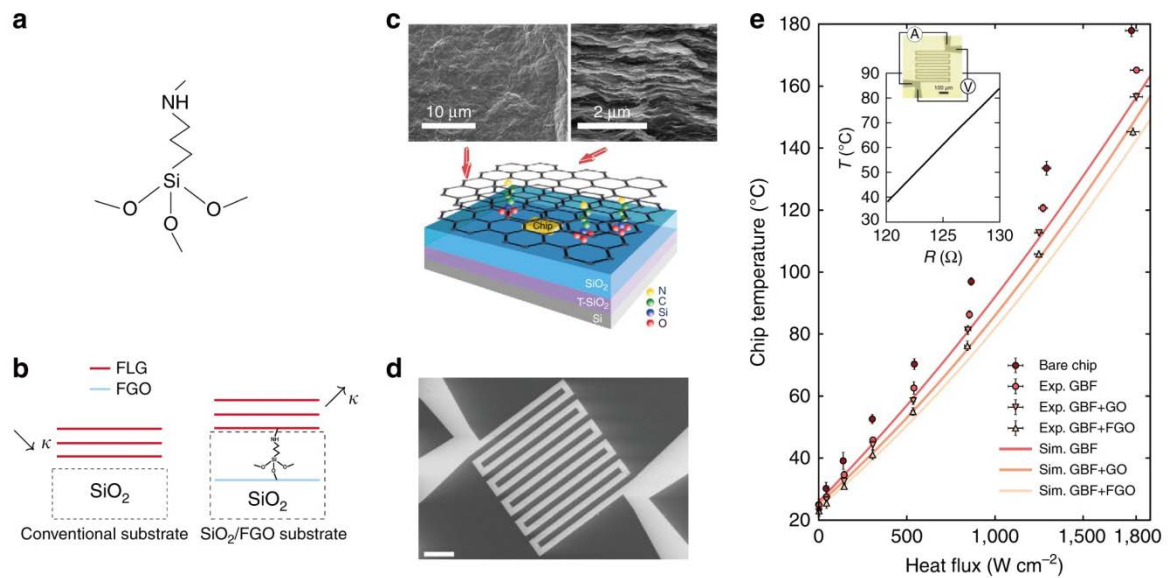


**Figure 2-13** Graphene-based film on FGO as heat spreader for hotspot. (a) Sketch of the chemical bonds of the silane molecule. (b) Schematic of a graphene film on different supports. Left: conventional silica substrate. Right: the proposed silica/FGO substrate. (c) Schematic of the measurement set-up together with the SEM image of the in-plane and the cross-section of the GBF. The chip is embedded in the SiO<sub>2</sub> substrate. T-SiO<sub>2</sub> stands for thermally grown SiO<sub>2</sub>. (d) SEM image of the chip as the hotspot. Scale bar, 100 μm. (e) Measured (filled markers) and finite-element-simulated (lines) chip temperatures versus the in-plane heat fluxes dissipated in a bare hotspot (rectangles), a hotspot covered by a GBF (circles), a chip covered by a GBF with non-functionalized GO (up triangle) and a chip covered by a GBF with APTES FGO (down triangle). ‘Exp.’ and ‘Sim.’ stand for experiments and simulations, respectively. Inset: calibration relationship between the resistance R and the temperature T of the thermal evaluation chip. Scale bar on the chip, 100 μm. The error bars correspond to the s.d.’s from the measurements on five samples.

an electronic component to demonstrate the heat-spreading capability of the supported graphene film. A direct current ( $I$ ) was input into the circuit by applying an outer voltage ( $V$ ) in Figure 2-13e, and hence the generated power is calculated as  $P=V \times I$ . Since the lateral dimension of the hotspot ( $A = 400 \times 400 \mu\text{m}^2$ ) is much larger than its thickness (260 nm), most of the heat is dissipated through the lateral direction of the hotspot. Hence the heat flux is defined as  $Q=P/A$ , and the direction is parallel to the substrate. The calibration relationship between the resistance  $R$  and the temperature  $T$  of the thermal evaluation chip is  $R(T)=0.21T+112$ . The temperature measurement uncertainty is  $\epsilon=\pm 0.5^\circ\text{C}$ . Figure 2-13e shows the temperature measured in situ at the hotspot and compares the thermal performance of the graphene film with and without the functionalization. With a constant heat flux of  $1300 \pm 2.3 \text{ W cm}^{-2}$  at the Pt chip, the hotspot temperature decreased from  $135 \pm 1.2$  to  $118 \pm 1.1^\circ\text{C}$  ( $\Delta T=17 \pm 2.3^\circ\text{C}$ ) with a GBF deposited on non-functionalized GO compared with the case of a bare chip. Such a remarkable temperature decrease is far beyond the measurement uncertainty  $\Delta T \gg \epsilon$ . Furthermore, with the same heat flux input, the hotspot temperature further decreased from  $118 \pm 1.1$  to  $107 \pm 0.8^\circ\text{C}$  ( $\Delta T=11 \pm 1.9^\circ\text{C}$ ) thanks to the presence of the APTES functionalization. The heat-spreading performance is thus enhanced by 57% via the functionalization. The heat-spreading performance of the equivalent macroscopic finite-element model also agrees reasonably well with the one measured by experiments.

### 2.3.1 Thermal resistance measurement with photothermal reflectance.

To further confirm the enhanced heat spreading assisted by molecular functionalization, we measured the interface thermal resistance by using the pulsed photothermal reflectance (PPR) method. To enhance heat absorption, a gold layer was evaporated on the surface of the GO and FGO layers after drop coating. The sample was first excited by a Nd:YAG laser pulse. This caused a fast rise in the surface temperature followed by a relaxation. The change of surface temperature was monitored by a probe laser, which reflects off from the samples' surface. Since the relaxation time is governed by the thermal properties of the underlying layers and interfacial thermal resistance between the layers, by obtaining the temperature profile one can extract the thermal properties of the layers and interface thermal resistance between the layers through a heat conduction model. Four sets of samples were fabricated, as shown in Figure 2-14. The thermal resistance  $R_1$  between the Au-Cr film and the (functionalized) GO layer, and the resistance  $R_2$  between (functionalized) GO layer and GBF or  $\text{SiO}_2$  were measured. The normalized surface temperatures of the four sample sets are shown in Figure 2-14 and the extracted thermal resistances are reported in Table 2.1. A fourfold reduction was achieved in the thermal resistance between GO and GBF from  $3.8 \times 10^{-8}$  to  $0.9 \times 10^{-8} \text{ m}^2\text{KW}^{-1}$ . On the GO– $\text{SiO}_2$  interface, the functionalization remarkably reduced the thermal resistance by a factor of almost three, from  $7.5 \times 10^{-8}$  to  $2.6 \times 10^{-8} \text{ m}^2\text{KW}^{-1}$ . We also observed a better thermal coupling on the metal–dielectric interface between Au-Cr and GO due to the surface chemistry.

### 2.3.2 Heat spreading through different functional molecules.

To gain a deeper insight into the impact of molecular structure on the thermal transport along the molecules, we used APTES, 11-Aminoundecyltriethoxysilane and

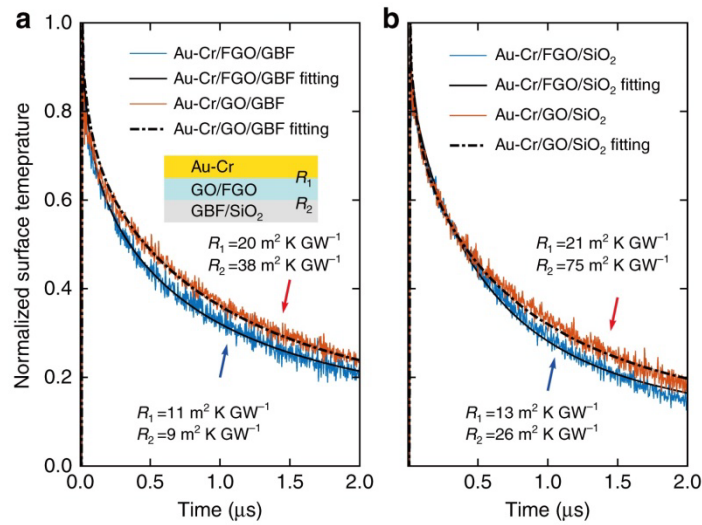


**Figure 2-14** Normalized surface temperature of PPR measurements of the thermal interface resistance. (a) Au-Cr/FGO/GBF and Au-Cr/GO/GBF samples and (b) Au-Cr/FGO/SiO<sub>2</sub> and Au-Cr/GO/SiO<sub>2</sub> samples. Inset: sample geometry for the PPR measurement. R<sub>1</sub> and R<sub>2</sub> refer to the thermal interface resistance between the Au-Cr film and the (APTES functionalized) GO layer, and that between (functionalized) GO layer and GBF or SiO<sub>2</sub>. The thermal resistances are also reported in Table 1.

**Table 2.1** Au/(F-)GO and (F-)GO/X interface thermal resistances

Au/(F-)GO and (F-)GO/X interface thermal resistances		
Interface	R <sub>1</sub> (m <sup>2</sup> KW <sup>-1</sup> )	R <sub>2</sub> (m <sup>2</sup> KW <sup>-1</sup> )
Au-Cr/GO/GBF	2.0E-8	3.8E-8
Au-Cr/FGO/GBF	1.1E-8	0.9E-8
Au-Cr/GO/SiO <sub>2</sub>	2.1E-8	7.5E-8
Au-Cr/FGO/SiO <sub>2</sub>	1.3E-8	2.6E-8

3-(Azidopropyl)-triethoxysilane as different functional agent on the GO to evaluate their heat-spreading performance on the same thermal test platform. The same concentration of  $0.1492 \text{ mol kg}^{-1}$  was used for all three types of molecules. Figure 2-15 shows the temperature reduction of the hotspot covered by GBFs with FGO using three different molecules. The results show that the heat spreader of GO functionalized with APTES has the best cooling performance. To properly understand this difference, an exploration of the internal vibrational properties of the molecule is crucial. We hence investigated how the differences in the phonon transmission impact the interfacial thermal transport. With this aim, we probed the phonon transmission  $\Xi(E_{\text{ph}})$  by atomistic Green's function to characterize the local heat conduction with and without the presence of the molecule. The phonon transmission functions through different molecules and the associated thermal conductance versus temperature are shown in Figure 2-15b-c. The phonon transmission at low phonon energies across the 11-Aminoundecyltriethoxysilane molecule is comparable to that across the APTES molecule, whereas at high phonon energies ( $>4 \text{ meV}$ ), the phonon transmission is considerably suppressed. Such a distinct phonon transport behavior is determined by the molecule chain length. By comparing the chemical structures, we can see that 11-Aminoundecyltriethoxysilane ( $-\text{N}-\text{C}_{11}-\text{Si}-\text{O}_3$ ) has the same functional groups as APTES ( $-\text{N}-\text{C}_3-\text{Si}-\text{O}_3$ ) but has a longer carbon backbone. Such a long chain length has a rather weak impact on the low-frequency phonons due to their very long wavelength but can strongly suppress the phonon transport at high frequencies. On the other hand, when comparing the phonon transmission through the junction of APTES and 3-(Azidopropyl)triethoxysilane ( $-\text{N}^-\text{N}^+\text{N}-\text{C}_3-\text{Si}-\text{O}_3$ ), it is evident to identify a stronger transmission at all frequencies. By comparing the chemical structures in Figure 2-15a, we can see that 3-(Azidopropyl)triethoxysilane has the same carbon backbone as APTES but has an azido group instead of an amino group. The azido group has strong interaction with the  $\text{sp}^2$ -bonded carbon lattice of graphene to form three-membered heterocycle structures. Given the similar backbone structure, the phonon eigenmodes in the molecule have not been significantly altered, but the transmission is enhanced due to the stronger thermal coupling to the graphene reservoirs. However, the introduction of nitrogen atoms into the  $\text{sp}^2$  carbon structure can strongly scatter phonons by distorting the structure of the graphene sheet, which leads to a poor thermal performance of the heat spreader.

Phonon transport analysis in APTES. We now investigate the detailed vibrational and electronic transport properties of the APTES molecule since it presents the best performance in heat spreading. We probed the phonon transmission  $\Xi(E_{\text{ph}})$  to characterize the local heat conduction with and without the presence of the APTES molecule. As shown in Figure 2-16, the transmission function  $\Xi(E_{\text{ph}})$  for the two adjacent graphene layers without any molecule displays a clear stepwise structure that provides the number of phonon channels. Low-energy phonons ( $E_{\text{ph}} \leq 10 \text{ meV}$ ) dominate heat conduction since the adjacent graphene flakes interact only through weak van der Waals forces that inhibit the transmission of high-frequency phonons. When the graphene layers are bridged by amino-silane molecules, the high-frequency phonons act as the major contributors in the heat conductance, creating more phonon channels through the covalent bond vibrations. This is in line with the transmission

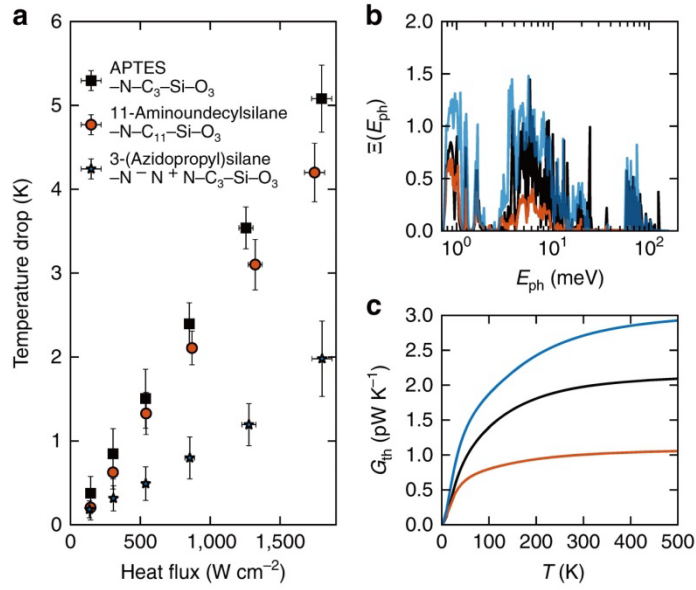


**Figure 2-15** Heat-spreading performance of GBF on FGO with different functional agents. The molecules are APTES, 11-Aminoundecyltriethoxysilane and 3-(Azidopropyl)triethoxysilane. (a) Measured temperature drop of heat spreaders with different functionalization molecules compared with that with non-functionalized GO. The error bars correspond to the s.d.'s of measurements on five samples for each molecule type. (b) Phonon transmission function for three different types of molecules used in the experiment. (c) Phonon thermal conductance through the molecules as a function of temperature. The color code of the data curves in b and c is the same as in a.

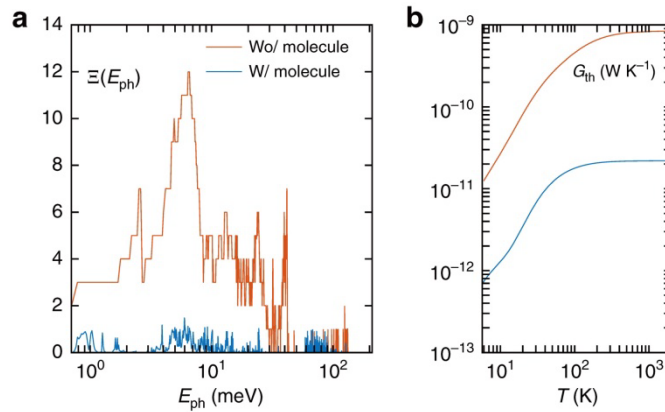


**Figure 2-16.** Phonon transport through the APTES molecule. (a) Phonon transmission versus phonon energy (red curve) between two adjacent graphene layers and (blue curve) through the APTES molecule bonding the two graphene layers. 'w/' and 'wo/' stand for with and without, respectively. (b) Thermal conductance  $G_{\text{th}}$  contributed by phonons versus temperature for the two cases

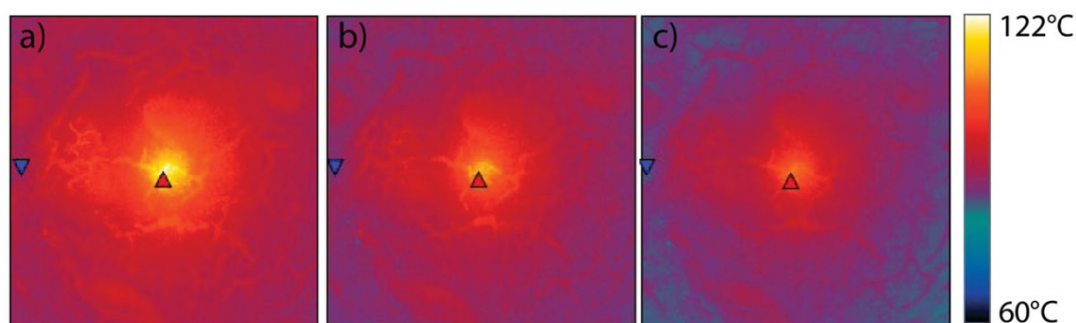


**Figure 2-17** IR images of (a) the bare platform, (b) platform with GBF and (c) platform with functionalized GBF. The peak temperatures for each platform are 121.9°C, 115.2°C and 110.9°C respectively, and the average temperatures of each testing platform are 97.2°C, 93.8°C and 91°C.

calculation of Segal et al. who observed a contribution to heat conduction by the higher-frequency phonons within the molecule coupled to the low-frequency phonons responsible for heat transport in the thermal reservoirs.

A thermal testing platform is designed to characterize the heat dissipating properties of functionalized GBF. To simulate the heat generation process of power devices, micro platinum (Pt)-based resistors are employed as the hotspot which can cause a significant temperature increase at one spot. The assembly of GBF onto the surface of the testing platform is realized through a self-developed tape assisting transfer process. GBF with square shape (1×1 cm) is firstly transferred onto a thermal release tape and then spin-coated with a thin layer of FGO (10~20 nm). After that, the functionalized GBF is transferred onto the thermal testing platform through releasing the thermal release tape by heating. In addition, a copper (Cu) heat sink is fixed on the top of GBF by mechanical springs to further dissipate the heat to the atmosphere. The usage of Cu heat sink allows the test platform to be operated at a high power density without failure.

The surface temperature distribution, peak and average temperature of the thermal testing platform are examined by infrared imaging (IR) camera. The operating currents for all the testing platforms are the same (120 mA) to maintain a constant heat generation speed. To ensure the same light emissivity from the substrate, the bottom surfaces of all the thermal testing platforms are also coated with graphite. IR images are taken when the testing platform reaches to the thermal steady state to minimize the deviations. The results are shown in Figure 2-17. As seen, the peak temperatures of bare platform, platform with GBF and platform with functionalized GBF are 121.9°C, 115.2°C and 110.9°C respectively, and the average temperatures of each testing platform are 97.2°C, 93.8°C and 91°C. It can be found that the peak temperature of the platform with functionalized GBF decreased more than 11°C than the bare platform and 5°C than that of pure GBF, indicating the efficient heat dissipation of functionalized GBF. These results show the great potential of using functionalized GBF as heat spreader for managing the thermal issues in power devices.

# Chapter 3

## Non-covalent Functionalization of CNMs

### 3.1 Non-covalent self-assembly of high-thermal-conductivity of graphene films

Thermal dissipation issues severely impact the performance and reliability of electronics, batteries and many other high power systems. One way to solve this problem is to integrate heat spreading materials that efficiently transport excessive heat away from power devices, thereby reducing the operating temperature of the system. To achieve this, the heat spreading material needs to have an ultra-high thermal conductivity in addition to a light-weight, flexible and robust structure to match the complex and highly integrated nature of power systems [99–101]. So far, however, there is no method to produce materials satisfying all of these criteria, at a large scale.

In this section, we introduced a novel, versatile and scalable method for the fabrication of large-area graphene films (GFs) with ultra-high in-plane thermal conductivity, and show that these could be used as a novel heat spreading material. The film formation relies on the phase change of large graphene oxide (GO) sheets in solution from random dispersion to liquid crystal structures, followed by thermal reduction at high temperatures and pressing. It enables large-scale production – we estimate an annual production capability of 2400 m<sup>2</sup> GFs. We show that the fabricated GFs have outstanding material properties, such as a thermal conductivity of over 3200 W/mK, an extremely good flexibility, and a mechanical tensile strength of over 70 MPa. The reported method and resulting GFs offer an efficient and

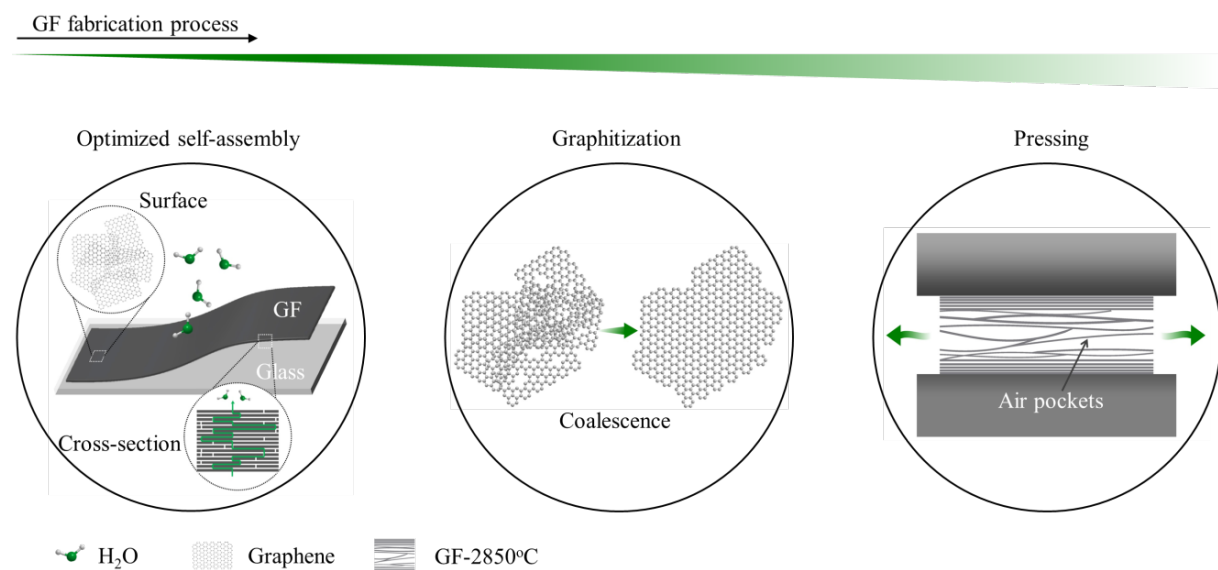


**Figure 3-1** Sketch of the fabrication process of GFs, including self-assembly, graphitization and pressing.

scalable heat dissipation solution for form-factor driven electronics and other power driven systems that is superior to commonly used materials.

Our method to fabricate highly thermally conductive GFs (Figure 3-1) is based on: i) an optimized self-assembly of large GO sheets into well-aligned thin film structures, ii) graphitization by a novel thermal reduction method at 2850°C, and iii) pressing.

Self-assembly of individual large GO sheets was deployed based on their liquid crystal properties [102]. To achieve extraordinary thermal and mechanical properties of the final GFs, we optimized the self-assembly process in several aspects, with regards to lateral sizes and thickness of the GO sheets, concentrations of the suspension, oxygen contents, and supporting substrates

### 3.1.1 Optimization of GF self-assembly process

The GO self-assembly process takes place at the gas-solution interface by following the continuous transition of GO suspensions from isotropic to liquid crystal during water evaporation. However, graphite oxide flakes fabricated from the Hummer's method are usually too thick to be able to form stable aqueous suspensions, which can cause phase separation and affect the self-assembly process. Therefore, it is essential to exfoliate the large graphite oxide to form thin layer GO sheets. However, most of the exfoliation process, such as ultrasonication, would also dramatically decrease the lateral size of GO and reduce the thickness at the same time [103,104]. Such small lateral size can bring strong adverse effect to the final thermal properties of GFs due to the severe phonon scattering induced by the grain boundaries of GO [105]. Previous studies revealed that even the coalescence of individual GO sheets at the graphitization temperature of carbon was not able to eliminate the grain boundaries that originated from the edges of the individual reduced GO sheets [105]. Therefore, a large lateral size of initial GO sheets is essential to reduce the ratio of interfaces and boundaries within the GFs, and ultimately, benefit for achieving the high thermal conductivity. In addition to this, GO sheets with a large lateral size show much higher affinity to get well-aligned structures than small sheets due to the high aspect ratio [102]. To obtain GO with a large lateral size, an efficient exfoliation process becomes necessary to decrease the thickness of starting graphite oxide flakes whilst ensuring minimum breakage of the exfoliated GO sheets.

Here, a high-speed shear mixing approach was developed to exfoliate graphite oxide and fabricate GO with a large lateral size. As shown in Figure 3-2a, the mixing head of the shear mixer was composed by a four-blade rotor sitting within a fixed stator with a distance about 100  $\mu\text{m}$ . During rotation, large graphite oxide flakes were sucked into the mixing head and driven towards the edge of the rotor/stator where the local shearing rate reached up to  $10^4 \text{ s}^{-1}$ . Upon such high shearing rate, it could easily overcome the weak interlayer Van der Waals' force between graphite oxide layers and exfoliate them into individual GO sheets while maintaining a large lateral size due to the very firmly  $sp^2$  bonded graphenic domains. Figure 3-2b-d show optical images of pristine graphite oxide flakes and GO sheets exfoliated by shear mixing and ultrasonication respectively. Pristine graphite oxide flakes present a lateral size with a diameter of 110  $\mu\text{m}$ . The large lateral size was attributed to the use of expanded graphite as the starting material, instead of commonly used graphite flakes. After exfoliation,

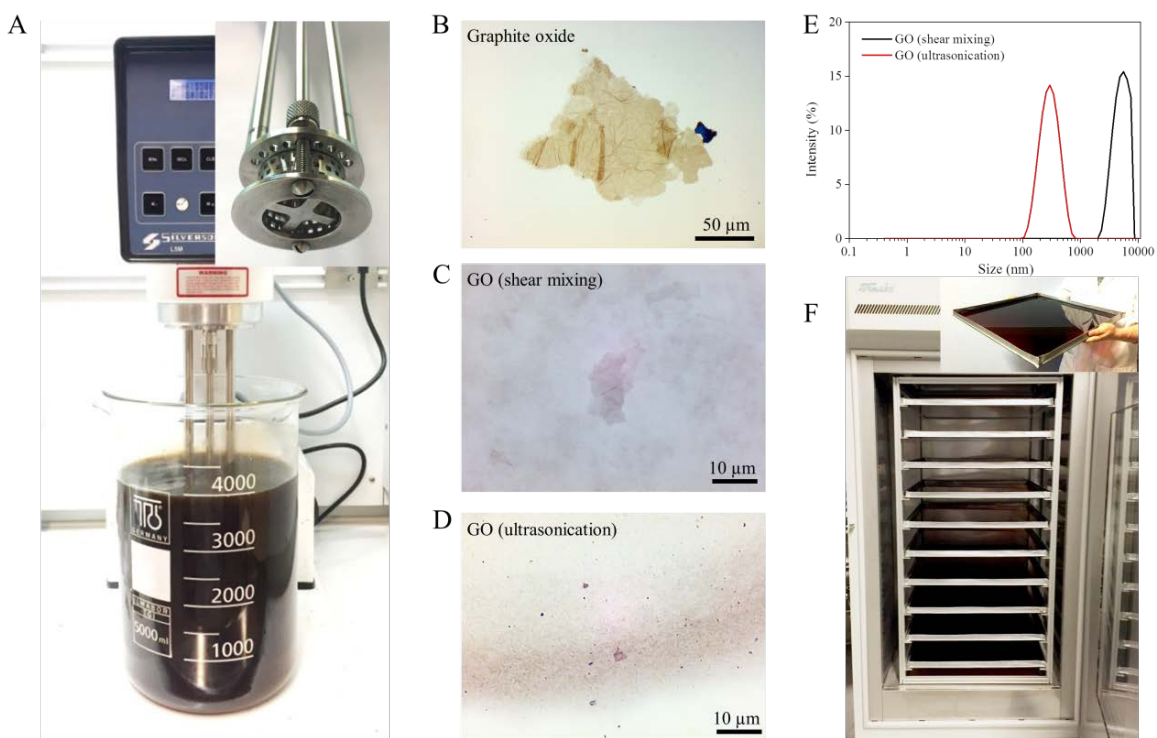


**Figure 3-2** (a) High speed shear mixing machine with a maximum capability of 12 L. The insert shows the mixing head of the shear mixer composed by a four-blade rotor sitting within a fixed stator. (b-d) Optical images of pristine graphite oxide (b), GO with an average size about 6  $\mu\text{m}$  fabricated by the high speed shear mixing approach (c), and GO with an average size about 300 nm fabricated by ultrasonication (d). (e) Particle size distribution of GO fabricated by the high speed shear mixing and ultrasonication respectively. (f) A 10-layer stacking 50 $\times$ 50 cm glass structure with dismantable frame assembled inside a furnace.

it was found from both the optical images (Figure 3-2c) and the particle size distribution curves (Figure 3-2e) that the lateral size of GO sheets fabricated by the high-speed shear mixing approach (6  $\mu\text{m}$ ) is orders of magnitude higher than that of ultrasonication methods (300 nm), showing the great advantages of the high-speed shear mixing approach on protecting the lateral size of GO during the exfoliation process. In addition, the thickness of the fabricated GO sheets by the high-speed shear mixing was less than 3 nm (<10 layers), showing the great exfoliation efficiency of the high-speed shear mixing approach. The ultrathin layer of GO sheets can improve the relative volume of turbostratic-stacking graphene during the self-assembly process, and thereby leads to superior final thermal and mechanical properties of GFs. In spite of that, the high-speed shear mixing approach also shows many more advantages than the commonly used ultrasonication method, including low power consumption, minimum temperature increase, high efficiency and mass production potential.

To evaluate the effect of concentration to the liquid crystal property of GO, a series of GO aqueous suspensions with varied concentrations in the range of 0.3-10 mg/mL were examined by a polarized optical microscope in transmission mode. As shown in Figure 3-3, GO sheets showed the typical birefringence effect of liquid crystals under crossed-polarizers, indicating the spontaneous formation of lyotropic nematic liquid crystals. The liquid crystal phenomenon was observed above a critical GO concentration of 1 mg/mL. Liquid

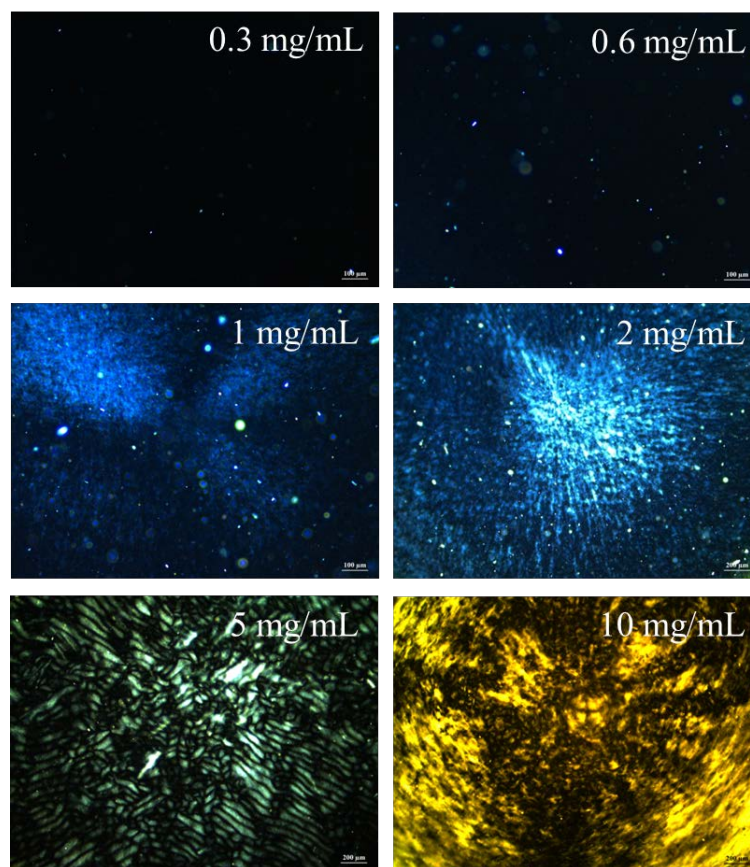


**Figure 3-3** Optical images of GO aqueous suspensions with varied concentrations in the range of 0.3-10 mg/mL, showing the effect of concentration change to the liquid crystal property of GO.

crystallization occurred at such a low GO concentration is due to the large lateral size of the GO sheets. Therefore, based on the liquid crystal property of GO in a wide range of concentrations, it was possible to regulate the final GF's thickness from hundreds of nanometers to hundreds of micrometers.

Proper GO oxygen contents are essential for both the self-assembly process and the final thermal performance of GFs. For example, the large amount of oxygen functional groups on the basal plane of GO is the main reason for GO to form stable aqueous suspension [106]. The lower the oxygen content, the worse is the stability of the suspension. The poor stability of the GO suspension can further decrease the alignment of GO sheets. Moreover, previous studies revealed that the  $sp^3$  bonded carbon can transform into stable  $sp^2$  bonded carbon upon high temperature annealing [105,107]. This would cause the coalescence of adjacent graphene sheets and form extended graphene layers, which contributes to a final high thermal conductivity of GFs. Therefore, relatively high oxygen content is essential for achieving well-aligned structures and high thermal conductivity of the final GFs. On the other side, very high oxygen contents can consume large amount of carbon atoms to form CO and CO<sub>2</sub> molecules during the thermal reduction process, which can cause large size shrinkage of the GF and also increase the overall consumption of GO [107]. Therefore, the oxygen contents need to be regulated into a certain range.

To figure out the proper oxygen content, three different graphene materials, including GO fabricated by Hummer's method, HGO by decreasing the amount of oxidation agents in

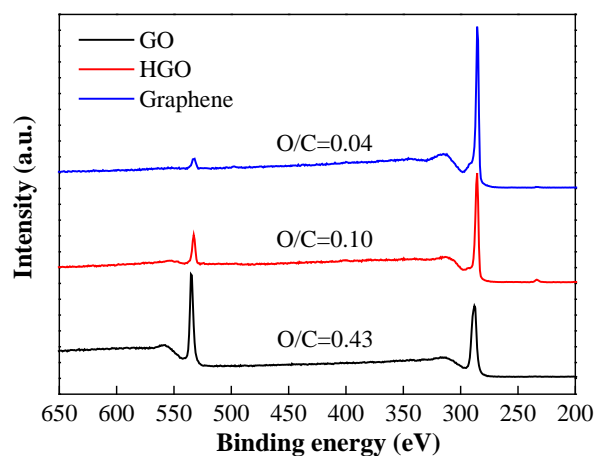


**Figure 3-4** XPS spectra of elemental composition of GO, HGO, and graphene fabricated in this work.

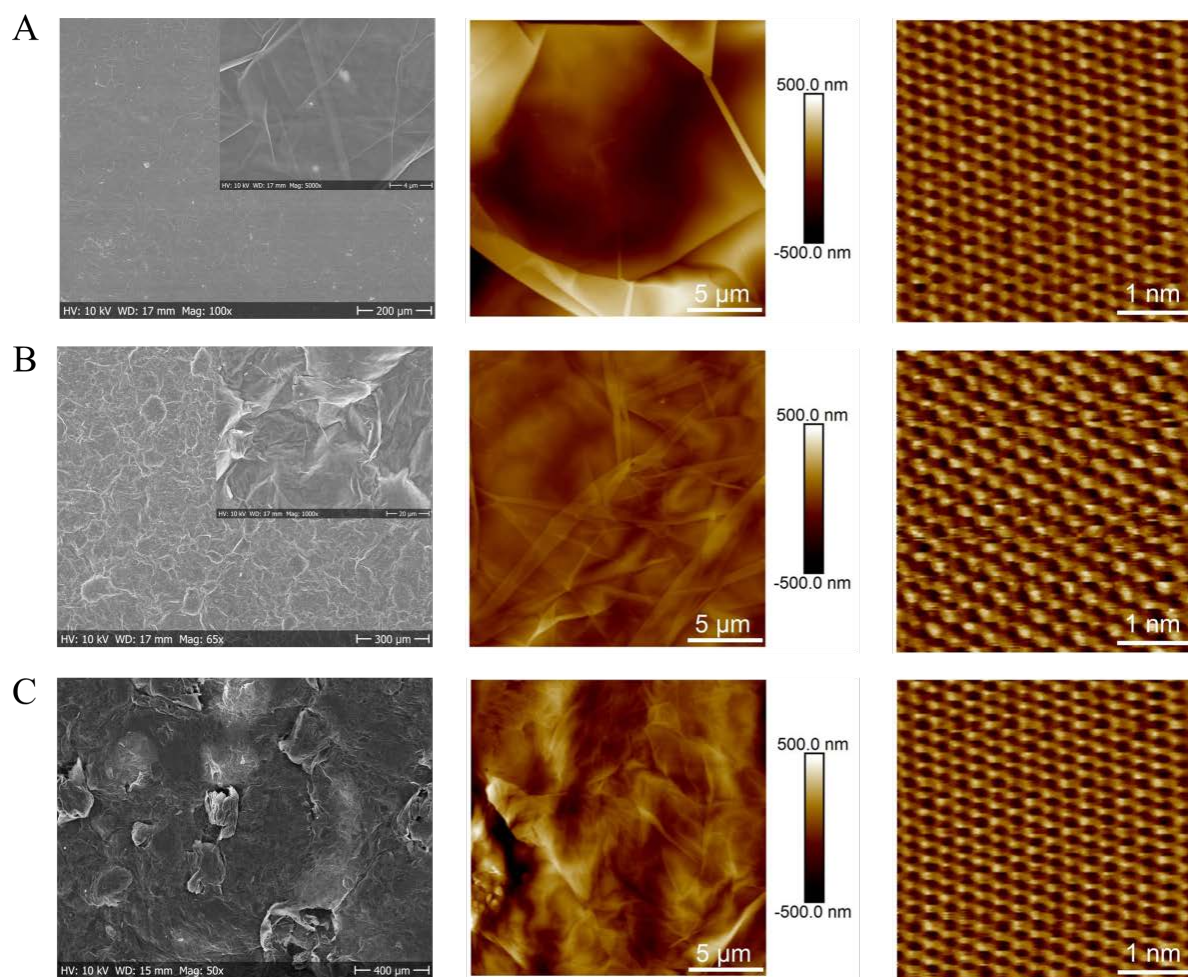


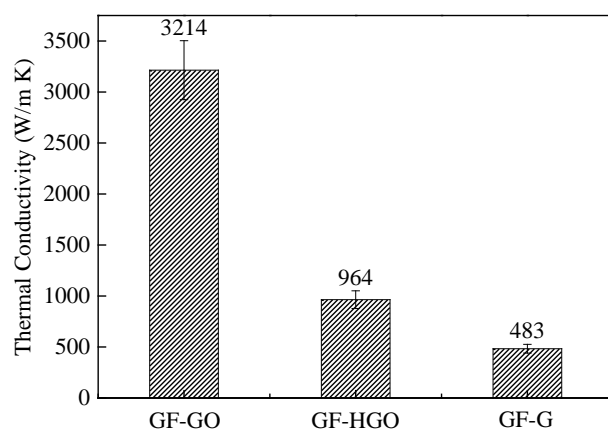
**Figure 3-5** SEM, AFM and STM images showing the surface morphology and atomic structures of GF-GO (A), GF-HGO (B), and GF-G (C).

Hummer's method, and graphene directly exfoliated from nature graphite, were used for making GFs (GF-GO, GF-HGO, and GF-G). The elemental compositions of different graphene materials were characterized by X-ray photoelectron spectroscopy (XPS). As shown in Figure 3-4, the O/C atom ratios of the different graphene materials are 0.43 for GO, 0.1 for HGO, and 0.04 for graphene.

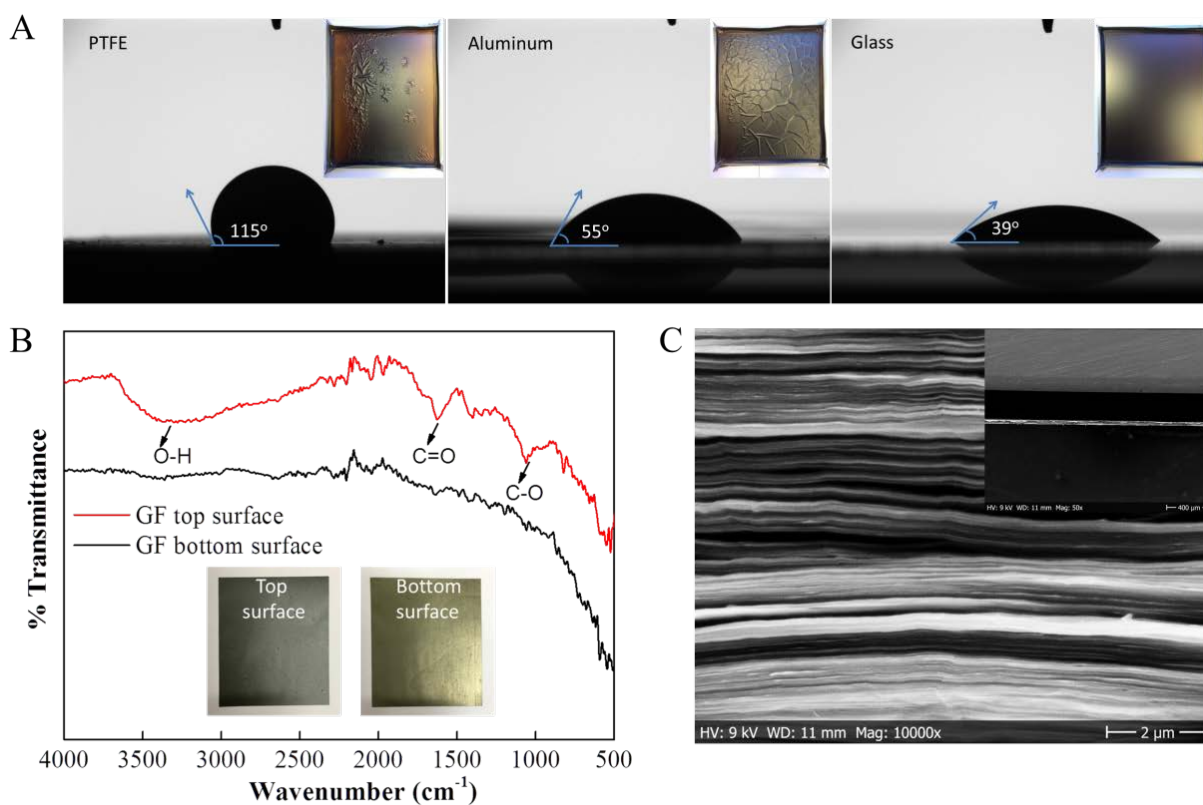
GFs based on different graphene materials were fabricated by following the process described in the method section, including self-assembly, graphitization at 2850°C and mechanical pressing. Figure 3-5 shows the surface morphology and atomic structures of GF-GO, GF-HGO, and GF-G. As shown, all GF samples display long-range honeycomb pattern with a periodicity of ~0.25 nm in the whole area of the recorded 4 nm × 4 nm scanning tunneling microscope (STM) image. At nanoscale, the structure is monocrystalline in all three samples, indicating good recovery of  $sp^2$  structure in all GF samples. However, the morphology at micro-scale shows quite big difference among the three samples. As shown in the SEM images, GF-GO shows highly flat surface with large smooth features. As a comparison, the surfaces of GF-HGO and GF-G are quite rough and filled with big wrinkles, particles and even cracks. The reason for such rough surfaces is the random assembly of HGO and graphene sheets during the film formation. Differently from GO, there is no liquid crystal property detected on HGO and graphene due to their low oxygen contents. Therefore, instead of forming well-aligned layer by layer structures, HGO and graphene tend to aggregate randomly and form big particles after removal of the solvents.

Figure 3-6 shows thermal conductivity of GF-GO, GF-HGO, and GF-G measured by the self-heating (IR) method (detailed measurement process in 5.4.1 section). It can be found that GF-GO shows a high thermal conductivity value of  $3214 \pm 289$  W/mK, which is about 3 times and 6 times higher than GF-HGO ( $964 \pm 87$  W/mK) and GF-G ( $483 \pm 43$  W/mK) respectively. Such a high thermal conductivity of GF-GO is attributed to its well-aligned structure. Therefore, relatively high oxygen content is essential for achieving well-aligned structures and high thermal conductivity of the final GFs. However, too high oxygen contents would lead to many other problems. For example, the calculated weight loss for GF-GO reaches about 50 wt% after the deoxygenation and the graphitization, which could cause the shrinkage of the film and increase the consumption of raw materials. Higher oxygen contents can also increase the number of defects, which further increase the grain boundaries of final GFs and lead to lower thermal conductivity.

The GF attaching substrate plays a crucial factor in the film flatness and uniformity due to different wetting angles of the GO solution on different substrate surfaces. To study this effect, GFs were self-assembled on three different substrates, including polytetrafluoroethylene (PTFE), aluminum, and glass. Figure 3-7a shows the wetting angles of 5 mg/mL GO droplets on different substrate surfaces and the insert shows the morphology of GFs attached on the different substrates. As shown, the GO droplet has the highest wetting angle ( $\theta_C=115^\circ$ ) on the very hydrophobic PTFE surface. The poor wetting behavior of PTFE surface could easily cause the folding and uneven spreading of the GO suspension, which would further lead to the formation of wrinkles and inhomogeneous thickness variation of the GFs. Aluminum substrate shows a better wetting property ( $\theta_C=55^\circ$ ) than the PTFE. However, due to the large coefficient of thermal expansion (CTE) of the aluminum [108], small temperature changes on the aluminum substrate surface would cause irregular stress distribution inside the film and



**Figure 3-6** In-plane thermal conductivity values of GF-GO, GF-HGO and GF-G.



**Figure 3-7** (A) Wetting angles of 5 mg/mL GO droplets on different substrate surfaces including PTFE, aluminum and glass. The insert shows the morphology of GFs attached on the different substrates. (B) FTIR spectra of the top and bottom surfaces of GF fabricated on the aluminum substrate showing the reduction effect of aluminum to GO. The insert shows the optical image of the top and bottom surfaces of GF fabricated on the aluminum substrate. (C) SEM image of the cross-section of GFs fabricated by following the optimized self-assembly process.

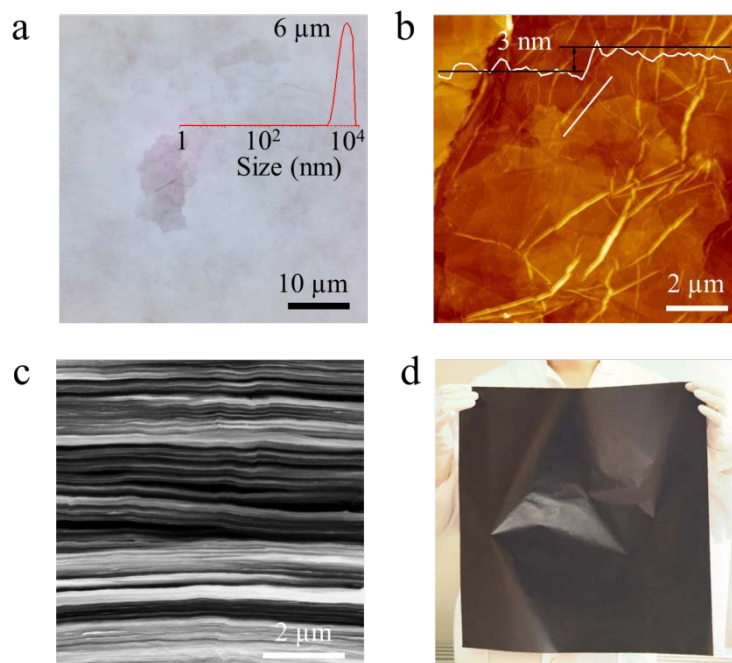


**Figure 3-8** (a) Optical image of GO with an average size about 6  $\mu\text{m}$  fabricated by high speed shear mixing approach. (b) AFM image of GO with a thickness less than 3 nm. (c) SEM image of the cross-section of fabricated GFs. (d) Optical image of the fabricated GFs with a size of 50 cm  $\times$  50 cm  $\times$  10  $\mu\text{m}$  showing the scalability of the process.

form wrinkles and even cracks on the surface of GFs. In addition, the aluminum substrate can even reduce GO during the self-assembly of GFs. Figure 3-7b shows Fourier transform infrared spectroscopy (FTIR) spectra of the top and bottom surfaces of the GF fabricated on the aluminum substrate. The top surface exposed to the air shows typical characteristic peaks of oxygen-containing functional groups, such as hydroxide, carbonyl and carboxyl groups, indicating the presence of GO sheets. However, those characteristic peaks of oxygen-containing functional groups almost vanished from the bottom surface that contacted with the aluminum substrate, showing a strong reduction effect of the aluminum substrate. Moreover, the insert shows the optical images of the top and bottom surfaces of the GF fabricated on aluminum substrate. Differently from the black color of the top GO surface, the bottom surface shows a shining metallic luster of graphite due to the reduction of aluminum that increased the visible light reflectivity. The reduction of aluminum substrate would change the originally hydrophilic GO surface to hydrophobic and decrease the stability of the GO suspension, which further lead to a poor alignment. Compared to PTFE and aluminum substrates, the glass substrate shows the best wetting property ( $\theta_c=39^\circ$ ), which would benefit the uniform distribution of the GO suspension on the glass surface. Moreover, the glass substrate has more advantages, such as low CTE value, flat and chemical inert surface, and strong bonding with GFs due to the interface hydrogen bonds. All these advantages would benefit to optimize the alignment and flatness of GFs on the glass substrate. The cross-section view of the GFs detached from the glass substrate shows a well-aligned layer structure with a uniform thickness (Figure 3-7c).

In brief, the freestanding GFs were manufactured via the self-assembly of shear exfoliated GO sheets with lateral sizes of  $> 6 \mu\text{m}$  (Figure 3-8a), thicknesses of  $< 3 \text{ nm}$  (Figure 3-8b), and

an oxygen content of 30 wt% on a glass substrate. The resulting GFs exhibited excellent layer alignment and flatness (Figure 3-8c), contributing to superior final thermal and mechanical properties. This optimized self-assembling process has many advantages, such as simplicity, cleanliness, high assembly efficiency, unlimited film size, showing great potential for large-scale production.

To demonstrate the scalability of the process, a 10-layer stacking glass substrate based frame was built and assembled in a furnace with a size of  $100 \times 60 \times 60$  cm. Figure 3-8d shows an example of fabricated large-area freestanding GFs with a size of  $50 \times 50 \times 10$   $\mu\text{m}$  exhibiting a flexible and robust structure. We show that with this process, GFs with thicknesses ranging from a few hundreds of nanometers to hundreds of micrometers can be fabricated.

### 3.1.2 Reduction of GFs

In order to obtain GFs with outstanding thermal conductivities along the in-plane direction, large grain sizes and low interlaminar interaction strength are required for GFs because heat conduction in graphene is essentially governed by phonon transport inside of the  $sp^2$  bonded hexagonal carbon lattice as well as phonon interfacial scattering [109–111]. To completely remove oxygen and enhance the grain size of the GFs, they were detached from the glass substrate and thermally reduced at a temperature of  $2850^\circ\text{C}$ . The success of the thermal reduction was then assessed by systematic structural characterizations with X-ray photoelectron spectroscopy (XPS), X-ray diffraction (XRD), Raman spectroscopy, scanning tunneling microscopy (STM) and atomic-force microscopy (AFM). These thermally reduced samples (GF- $2850^\circ\text{C}$ ) were compared to GFs treated by typical methods: chemical reduction by L-ascorbic acid (GF-VC) [112] and hydroiodic acid (GF-HI) [113,114], as well as thermal reduction at the carbonization temperature of  $1300^\circ\text{C}$  (GF- $1300^\circ\text{C}$ ) [115–117].

XPS measurements revealed that, after reduction, all GF samples showed a significant decrease of the oxygen content (O/C atom ratios) compared to the untreated GFs (Figure 3-9a). The deoxygenation efficiency was found to be increasing in the order GF-VC < GF-HI < GF- $1300^\circ\text{C}$  < GF- $2850^\circ\text{C}$ . The chemical reductions only showed limited deoxygenation efficiency for GFs because of the slow chemical penetration capability. In contrast, the thermal reduction revealed a more effective and homogenous deoxygenation to GFs. For GF- $2850^\circ\text{C}$ , the O1s peak could not be detected by the instrument, suggesting a negligible amount of remaining oxygen groups. The high temperature makes the oxygen containing functional groups unstable, and leads to chemical bond rupture and the release of the oxygen atoms in the form of CO and CO<sub>2</sub> molecules to the ambient [118]. The sharp and pronounced C=C/C-C peak at 284.6 eV in the high resolution C1s spectrum (Figure 3-9b) of GF- $2850^\circ\text{C}$  indicated the recovery of  $sp^2$  bonded carbon lattice structure in GFs upon  $2850^\circ\text{C}$  [119]. In addition, in the thermal reduction processes, the generation of any residuals is avoided, such as iodine in GF-HI (I3d3 and I3d5 peaks) [113,114] (Figure 3-9a), which may affect the properties of GFs after the reduction.

In order to investigate the crystallinity of the differently reduced GF samples, they were characterized by thin film XRD analysis (Figure 3-9c). The  $2\theta$  peak corresponding to the (002) plane reflection of graphite appeared at  $11.5^\circ$ ,  $11.6^\circ$ ,  $24.3^\circ$ ,  $25.9^\circ$ , and  $26.5^\circ$  in the

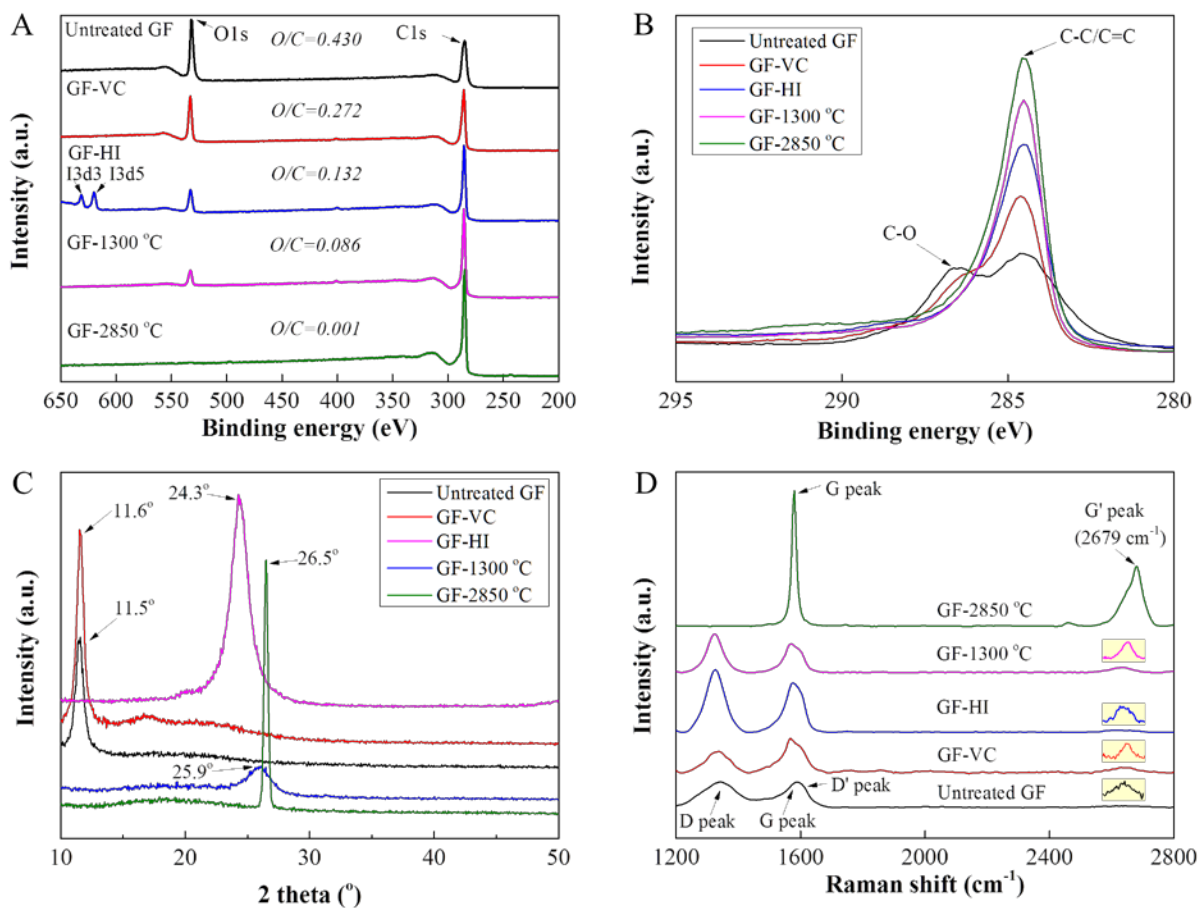


**Figure 3-9** Reduction of GFs. (A) XPS spectra of the elemental composition of different GFs. (B) The high resolution C1s spectra of different treated GFs. (C) XRD spectra of the crystallinity evolution and interlaminar consolidation of GFs under different treatments. (D) Raman spectra of GFs after different treatments.

spectra of the untreated GF, GF-VC, GF-HI, GF-1300°C, and GF-2850°C, respectively. The corresponding interlayer distances (*d*-spacing) of the graphene sheets, as calculated according to Bragg's law [120], are about 7.69 Å, 7.63 Å, 3.66 Å, 3.44 Å, and 3.36 Å, respectively. Only the sample GF-2850°C exactly matched the *d*-spacing in pure graphite [121] of 3.36 Å, and also exhibited the sharpest reflection peak. The expanded interface distances in the other samples can be due to the intercalation of oxygen atoms and the incorporation of water molecules or impurities [102,114].

To examine the grain size and layer stacking type of GF samples, Raman spectroscopy was employed (Figure 3-9d). The Raman spectra of the GFs were dominated by four features including the G peak (1580 cm<sup>-1</sup>) and G' peak (2679 cm<sup>-1</sup>) arising from the in-plane stretching motion of *sp*<sup>2</sup> carbon-carbon bonds, and two defect related peaks of D (1325 cm<sup>-1</sup>) and D' (1620 cm<sup>-1</sup>). The strong D and D' peaks in the spectrum of untreated GFs indicate a large amount of structural defects existing in the carbon lattice [122]. The ratios of D and G band intensities (*I*<sub>D</sub>/*I*<sub>G</sub>) are used for quantitative measurement of the amount of defects presented in graphitic materials. The *I*<sub>D</sub>/*I*<sub>G</sub> ratios were determined to be 1.00, 0.63, 1.23, 1.35, and 0.003 for the untreated GBF, GBF-VC, GBF-HI, GBF-1300°C and GBF-2850°C respectively. The relatively increased *I*<sub>D</sub>/*I*<sub>G</sub> ratios of GBF-HI and GBF-1300°C were caused by the increased amount of small-sized aromatic areas formed after reduction. In contrast to the other GF samples, the integrated intensity ratio of the D and G peaks (*I*<sub>D</sub>/*I*<sub>G</sub>) of GF-2850°C was determined to be the lowest. According to Cançado's equation [123], the calculated in-plane crystallite size (*L*<sub>a</sub>) of GF-2850°C reaches to 13.3 μm, indicating an efficient improvement of grain size in the GFs after graphitization. In addition, G' peak of GF-2850°C shows that GF-2850°C is a mixture of turbostratic-stacking graphene and AB Bernal stacking graphene [105]. Differently from AB Bernal stacking graphene, the absence of interlamellar Van der Waals' force in turbostratic-stacking graphene contributed significantly to a much decreased the phonon interfacial scattering. The relative volume of turbostratic-stacking graphene was determined to be ~30% in GF-2850°C (Figure 3-10). The presence of large-grain and turbostratic-stacking graphene is essential for the high in-plane thermal conductivity of GF-2850°C.

To assess the atomic structure of the various reduced GF samples, they were characterized by STM (Figure 3-11a-e) and compared to the standard reference of highly oriented pyrolytic graphite (HOPG) (Figure 3-11a). Most areas of GF-VC and GF-HI were found to contain random and disordered atomic-sized features (Figure 3-11b and Figure 3-11c) associated with different types of defects, in addition to some relatively ordered and isolated graphene domains of < 1 nm. Differently, the STM image of GF-1300°C (Figure 3-11d) showed apparently regular patterns in large areas but lacked the typical long-range honeycomb structures of HOPG [124]. It shows that the *sp*<sup>2</sup> healing effect at the carbonization temperature of 1300°C is not enough to completely repair the atomic defects of GBFs. This result is also consistent with the explanation of the increased *I*<sub>D</sub>/*I*<sub>G</sub> ratio in Raman spectrum after thermal reduction at 1300°C (Fig. 2D). The large amount of small-sized graphitic domains generated during the reduction leads to the increase of the number of six-fold aromatic rings that lie in close proximity to the defects, which further caused the increase of the intensity of D peak in Raman spectrum. For GF-2850°C (Figure 3-11e), a long-range honeycomb pattern was found with a periodicity of ~0.25 nm, which was completely free of

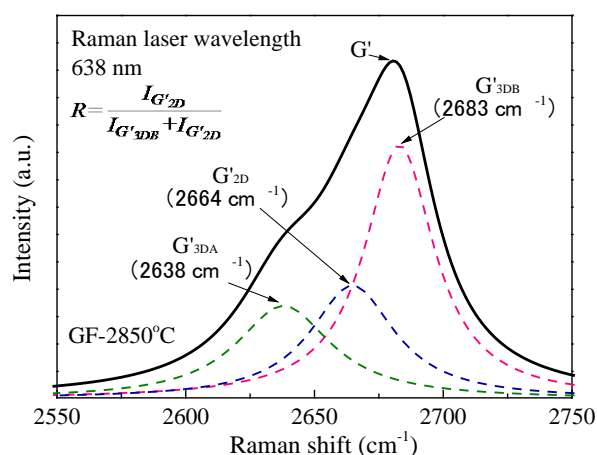


**Figure 3-10** The Raman G' peak of GF-2850°C shows that GF-2850°C is a mixture of turbostratic stacking graphite and AB Bernal stacking graphite. To evaluate the relative volume of turbostratic graphite in GF-2850°C, the G' peak of GF-2850°C was fitted by three Lorentzian components, including G'<sub>2D</sub> (2664 cm<sup>-1</sup>) corresponding to turbostratic graphite, G'<sub>3DA</sub> (2638 cm<sup>-1</sup>) and G'<sub>3DB</sub> (2684 cm<sup>-1</sup>) corresponding to AB Bernal stacking graphite. According to Cançado's equation [125] (insert in the figure), the relative volume of turbostratic graphite (*R*) was determined to be ~30% for GF-2850°C.

any defects in the area of the recorded 4 nm × 4 nm STM image.

In addition to the effect of atomic structures, wrinkles and interfaces also strongly affect the phonon scattering at the microscale, and the average size of smooth features on the surface of GFs is one key parameters to controlling their thermal performance [105]. Therefore, micro-sized morphology changes in the different GF samples were measured with AFM (Figure 3-11f-j). The untreated GFs (Figure 3-11f) exhibited a relatively rough topography with only very small smooth features (~1.5 μm), which were even smaller than the original size of the GO sheets (~6 μm). We assume that the small smooth features were caused by the wrinkle nature of GO sheets and the random overlapping of individual GO sheets during the film formation. Similarly, no significant increase of the size of smooth features was detected from the surface of the two chemically reduced GFs (Figure 3-11g-h), indicating that chemical reductions have no obvious effect to improve the surface flatness of GFs. For GF-1300°C (Figure 3-11i), larger smooth features and a flat topography was observed. In GF-2850°C (Figure 3-11j), most of the overlaps between neighboring graphene sheets were eliminated, and the size of smooth features largely increased from 1.5 to 16 μm, which is almost three times larger than the original size of the GO sheets. This shows that the high temperature reduction can lead to the coalescence of adjacent graphene sheets and transform the originally random stacked GO sheets to flat and extended graphene layers. Previous studies have reported that thermal treatment with a temperature above 2000°C has a smoothing effect on the surface of graphene by eliminating nanoscale wrinkles [107], which could also contribute to the high flatness of GF-2850°C. In addition, the size of observed smooth features of GF-2850°C upon AFM shows good consistence with the calculated grain size from Raman.

In conclusion, the developed thermal reduction at 2850°C exhibits many advantages

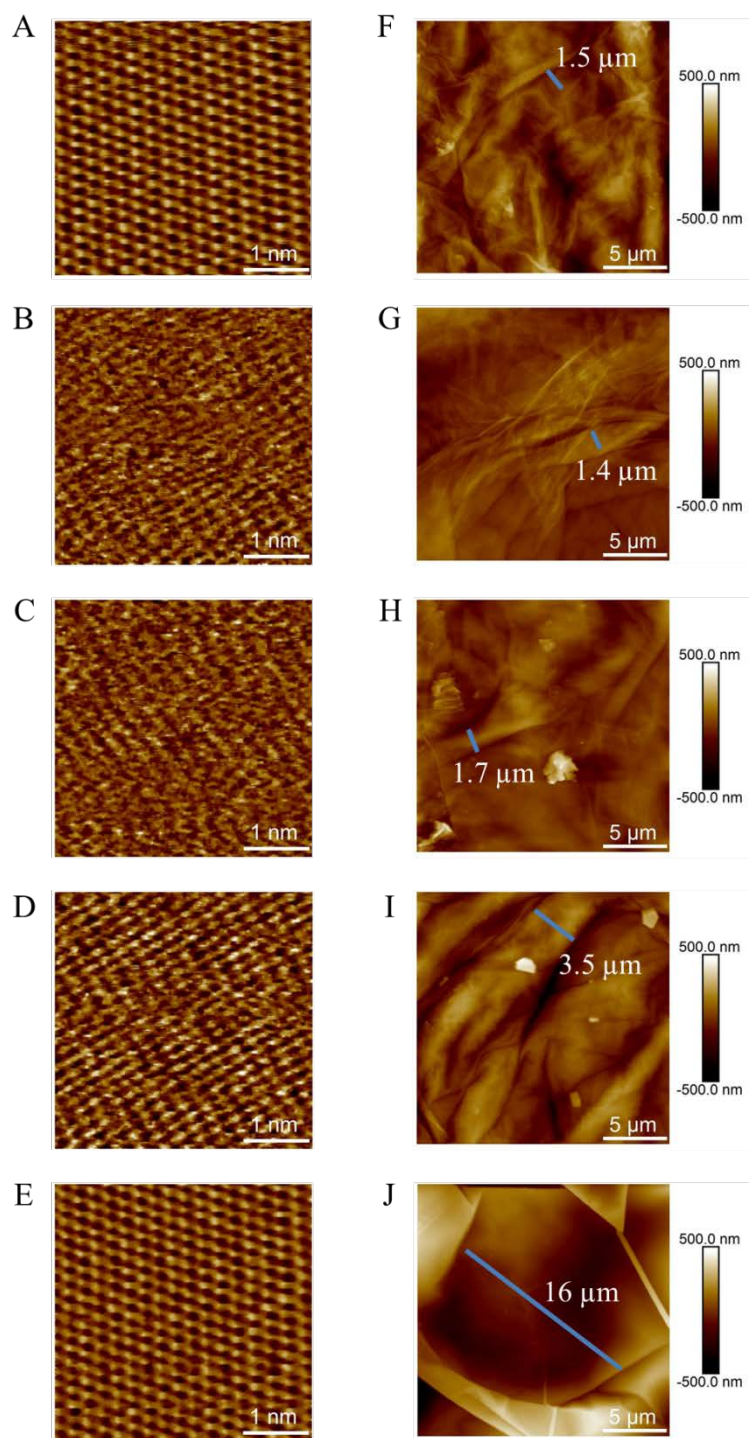


**Figure 3-11** The atomic structure and morphology change of GFs upon different treatments. (a-e) STM images showing atomic structures of different GFs. (a) HOPG. (b) GF-VC. (c) GF-HI. (d) GF-1300°C. (e) GF-2850°C. (f - G) AFM images showing morphologies of different GFs. (f) untreated GFs. (g) GF-VC. (h) GF-HI. (i) GF-1300°C. (j) GF-2850°C.

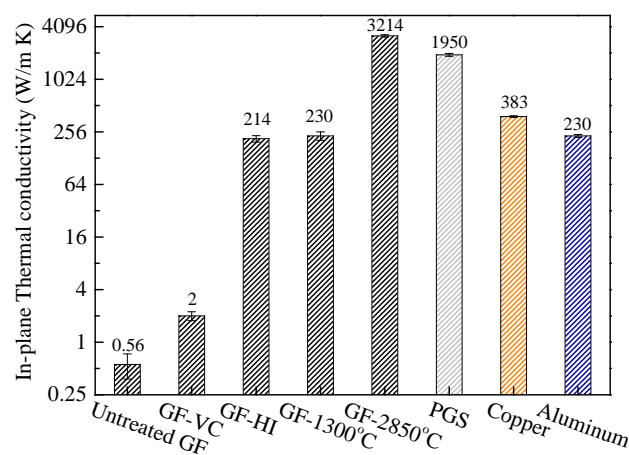


**Figure 3-12.** In-plane thermal conductivities of different GFs including untreated GFs, GF-VC, GF-HI, GF-1300°C, and GF-2850°C and the highly thermal conductive materials PGS, copper, and aluminum.

compared to other chemical and thermal reduction methods, such as: (i) simplicity, since the deoxygenation and graphitization of GFs occur all in one step; (ii) high efficiency on deoxygenation and extending grain size of GFs; (iii) cleanliness, since it avoids the use of toxic chemicals and also prevents the generation of any residuals which may affect the properties of GFs after the reduction; (iv) scalability.

### 3.1.3 Thermal conductivity of GFs

To investigate the thermal properties of GF-2850°C, their in-plane thermal conductivities were measured at different film thicknesses using a self-heating method based on infrared radiation (IR) (see supporting paper). The results were compared to conductivities from untreated GFs, GF-VC, GF-HI and GF-1300°C samples, to measurements using other methods, and to conductivities from commercially available thermally conductive pyrolytic graphite sheets (PGS). To aid the interpretation of the results, Molecular dynamics (MD) simulations regarding the effects of grain size and layer misfits/wrinkles to in-plane thermal conductivity were performed, and cross-section images of the GF-2850°C sample were investigated.

The untreated GF (Figure 3-12) revealed an extremely low thermal conductivity value of  $0.56 \pm 0.18$  W/mK, which is much lower than the calculated amorphous limit of graphene ( $\sim 11.6$  W/mK) [126], demonstrating the superior thermal insulation property of the untreated GF. This extremely low in-plane thermal conductivity of untreated GF is attributed to the significantly magnified phonon scattering effects at high oxygen coverages [126]. For GF-VC, GF-HI, and GF-1300°C, the in-plane thermal conductivity values were measured to  $2 \pm 0.2$  W/mK,  $214 \pm 18$  W/mK and  $230 \pm 25$  W/mK, respectively. Generally, the in-plane thermal conductivity values of the chemically reduced GFs were found to increase with decreasing oxygen contents. However, these values were found to be much lower than commercial PGS, copper and aluminum, showing the limited thermal performance of GFs treated by chemical methods.

The in-plane thermal conductivity for GF-1300°C was found to be close to the value for GF-HI despite significantly decreased oxygen content. We found that the relatively low in-plane thermal conductivity of GF-1300°C was mainly caused by a low density of the sample (Figure 3-13). The removal of oxygen lead to the expansion of the graphene layer distance and also formed micro-scaled air pockets, even cracks, which dramatically decreased the film density to 0.2 g/cm<sup>3</sup>. The following mechanical pressing could not improve the film density significantly because of a substantially decreased bonding strength between adjacent graphene sheets after removing hydrogen bonds that previously bond GO sheets. However, GF-2850°C showed an extremely high in-plane thermal conductivity of 3214 ± 289 W/mK, which represents an enhancement by almost four orders of magnitude compared to the untreated GF, and of more than one order of magnitude compared to the chemically reduced GFs and GF-1300°C.

To compare the in-plane thermal conductivity of GF-2850°C at different sample thicknesses and to exclude errors from the testing method, we varied the thickness of mechanically pressed GF-2850°C and used two additional testing methods, namely a self-heating method based on dependence of the resistance on the temperature (DRT) in vacuum and an improved thermal bridge (ITB) method (see supporting paper). Independent samples were fabricated and measured for each single test point to study the repeatability. We found that the GF-2850°C sample with the smallest thickness of 0.8 μm showed the highest in-plane thermal conductivity of 3214 ± 289 W/mK as measured with self-heating (IR) (Figure 3-14). The values measured with the other methods were 3300 ± 297 W/mK for self-heating (DRT) and 3109 ± 139 W/mK for the ITB method. For all thicknesses, the results of all methods were consistent, indicating a high accuracy of the developed thermal measurement. With increasing sample thicknesses, we found that the thermal conductivity decreased and levelled off at average values of 2234 ± 338 W/mK for thicknesses between 4 and 13 μm, approaching the value corresponding to HOPG of ~2000 W/mK. Further increase of thicknesses to 50 μm made the thermal conductivity of GF-2850°C decrease to 1691 ± 172 W/mK.

The very high thermal conductivity of GF-2850°C that even outperforms HOPG, at small film thickness, is attributed to the presence of turbostratic-stacking graphene in GF-2850°C. Previous studies have shown that multilayer graphene can reach to the same in-plane thermal conductivity as monolayer graphene if the interlaminar Van der Waals' force was sufficiently weak enough [111]. The absence of stacking order in turbostratic-stacking graphene leads to a very weak interaction between adjacent planes [122], which greatly reduced the phonon interface scattering and resulted in the ultra-high in-plane thermal conductivity of GF-2850°C that is superior to HOPG.

MD simulations showed further that the ultra-high in-plane thermal conductivity of GF-2850°C was also attributed to the generation of graphene with large grain sizes of above 13 μm (Figure 3-15). This is consistent with the result of a recent study that concluded that the increase in grain size from ~200 nm to ~10 μm lead to an exponentially increased thermal conductivity of graphene from ~610 to ~5230 W/mK [127]. MD simulations also revealed that the decreased thermal conductivity with the increase of film thickness was intimately related to an increased amount of wrinkles/misfits in the thick layers.

The ultrahigh in-plane thermal conductivity of GF-2850°C is also closely related to its

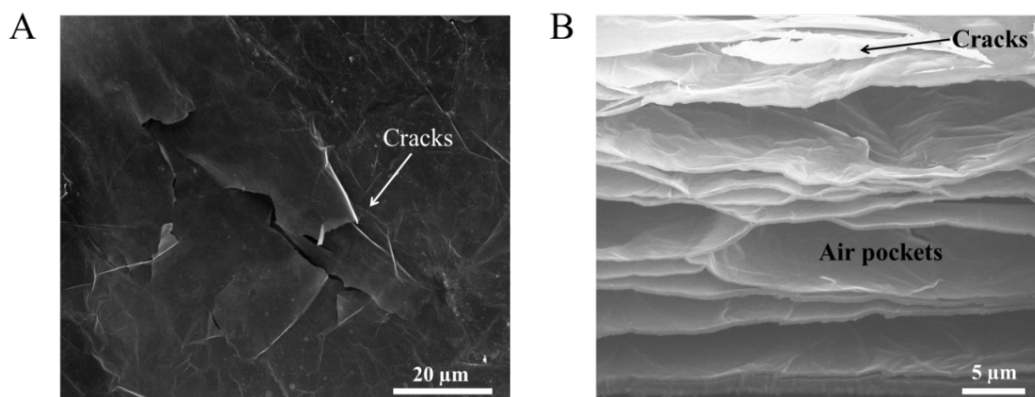


**Figure 3-13** (A) SEM image of surface morphology of GF-1300°C, showing the generation of cracks after heat treatment at 1300°C. (B) Cross-section SEM image of GF-1300°C after mechanical pressing. Air pockets generated during heat treatment cannot be removed even by mechanical pressing due to the weak bonds between individual graphene sheets. The surface of the film shows the cracks.

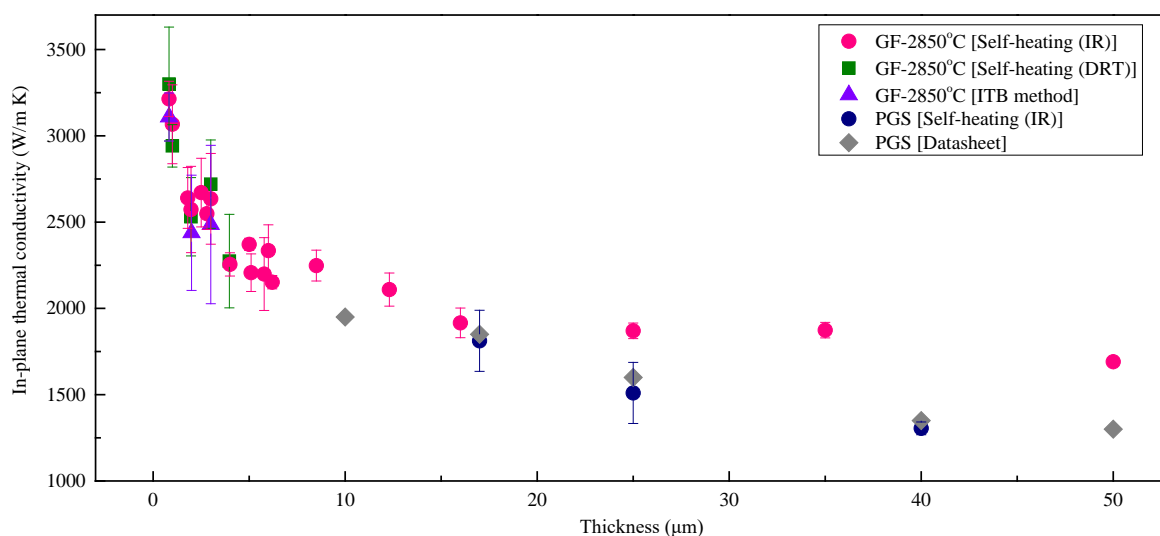


**Figure 3-14.** (A) In-plane thermal conductivities of GF-2850°C in the thickness range of 0.8-50 μm measured by self-heating (IR), self-heating (DRT) and ITB methods and in-plane thermal conductivity of PGS in the thickness range of 10-50 μm from the product datasheet and measured by the self-heating (IR) method.

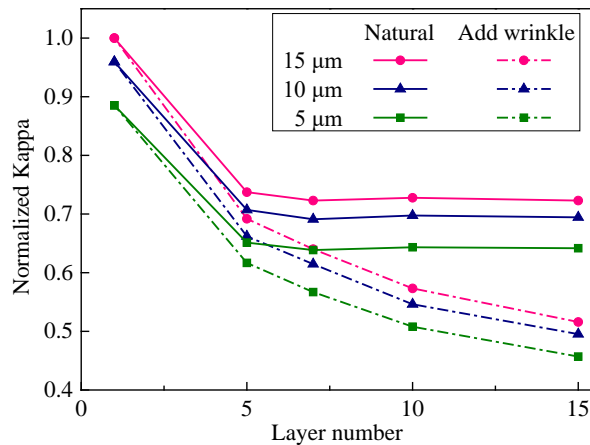


**Figure 3-15.** MD simulation results about the effect of wrinkles and grain size of graphene to thermal conductivity change at different layer numbers of graphene. With the increasing of the number of wrinkles inside the film, thermal conductivity of the layers shows significant decrease due to the increased phonon scattering induced by the wrinkles. A large grain size can give a higher thermal conductivity due to the relatively decreased amount of grain boundaries.

microstructural change. To study this effect, GF-2850°C samples with different thicknesses were cut by utilizing focused ion beam milling (FIB) and the cross-section were imaged by SEM (insert of Fig. 4). The pristine GF-2850°C sample before pressing was found to contain many air pockets, which altered the originally well-aligned GO sheets to loose layer structures.

Unlike GF-1300°C, the strong layer coalescence of individual graphene sheets in GF-2850°C gave the sample very high mechanical strength and prevented the generation of cracks. However, the presence of air pockets caused a significantly reduced in-plane thermal conductivity due to the substantially decreased film density and large phonon scattering. Mechanical pressing decreased the film thickness from about 2 μm to 0.8 μm. The compressed film exhibited a highly firm structure without any obvious air pockets. The firm and well-aligned structure contributed significantly to the ultra-high thermal conductivity of GF-2850°C. In addition to this, we noticed that the size and the amount of air pockets increased with the increase in the film thickness. Due to the strong air impermeability and robust structure of graphene, the removal of air pockets became much more difficult for thick GF samples. As a result, the irregular shape of air pockets increased the local phonon scattering by causing the folding and misfits of adjacent graphene layers. These phenomenon became more obvious in the thick samples, and thereby, leading to the gradual decrease of the thermal conductivity of the GF from 3214 W/m K to 1691 W/m K with the increase of film thickness from 0.8 μm to 50 μm.

In addition, the through-plane thermal conductivity of GF-2850°C measured by the pulsed photothermal reflectance (PPR) method was determined to be  $14.8 \pm 1.5$  W/mK, which is orders of magnitude lower than its in-plane thermal conductivity, indicating a strongly anisotropic thermal property (Figure 3-17). The presence of air pockets can also improve the thermal anisotropy of the film by significantly decreasing the through-plane thermal conductivity, giving GF-2850°C great advantages as novel heat spreading materials [116].

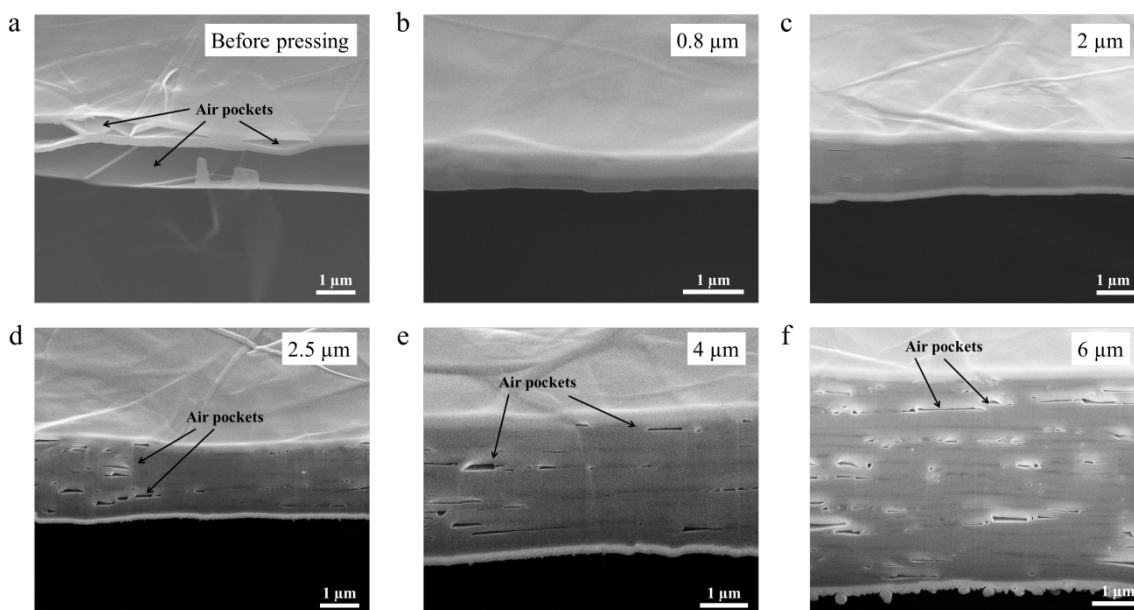


**Figure 3-16** (a) Cross-section image of GF-2850°C (0.8  $\mu\text{m}$ ) before pressing, (b to f) Cross-section image of GF-2850°C after pressing. (b) 0.8  $\mu\text{m}$ . (c) 2  $\mu\text{m}$ . (d) 2.5  $\mu\text{m}$ . (e) 4  $\mu\text{m}$ . (f) 6  $\mu\text{m}$ .

The comparison of the in-plane thermal conductivity of GF-2850°C to the commercially available PGS at higher film thicknesses of 10-50  $\mu\text{m}$  revealed a higher thermal conductivity for the GF-2850°C sample at all investigated thicknesses. We assume that the reasons for this are the gradually decreased densities of commercial PGS with increasing film thickness (Table 3.1 and Figure 3-18) as well as the significantly increased amount of curvatures and layer misfits when the film thickness is above 25  $\mu\text{m}$  [128]. In contrast to the PGS, an increase in thickness of GF-2850°C does not lead to an obvious increase in layer misfits in the GF-2850°C sample due to the pre-assembled and well-aligned film structure before graphitization. Therefore, the well-aligned graphene layer structure and high density contributed significantly to a greatly enhanced thermal conductivity for film thicknesses larger than 25  $\mu\text{m}$ .

To shed light on the difference in in-plane thermal conductivity of PGS and GF-2850°C, we also compared the cross-section images (Figure 3-19). We found that the surfaces of PGS samples from different suppliers were filled with large amounts of wrinkles and gaps (Figure 3-19a-f). The surface morphology of unpressed PGS revealed that those wrinkles/gaps were mainly located at the boundary of pebble-like structures which were generated during the PI pyrolytic process (Figure 3-19d). The presence of large amounts of wrinkles and gaps can significantly enhance the phonon scattering in the in-plane direction, and thereby, limiting the in-plane thermal conductivity of PGS. On the contrary, the horizontally aligned air pockets inside of GF-2850°C and highly smooth surfaces (Figure 3-20) show a smaller effect on the in-plane phonon transfer.

In conclusion, the outstanding thermal performance of GF-2850°C with an ultra-thin thickness represents more than 100% improvement compared to the best data ever reported in previous studies of different graphene assembled structures, such as graphene papers [115,116,129,130] and graphene fibers [131]. The in-plane thermal performance of

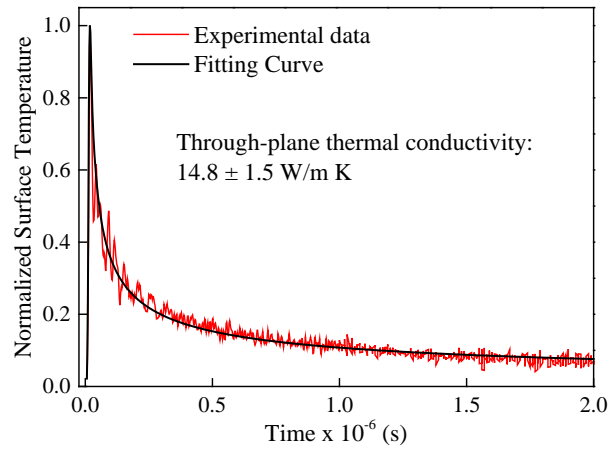


**Figure 3-17.** Normalized surface temperature of Au/6  $\mu\text{m}$  thick GF-2850 $^{\circ}\text{C}$ .

**Table 3.1.** The measured density change of GF and PGS at different thickness

GF-2850 $^{\circ}\text{C}$		PGS	
Thickness ( $\mu\text{m}$ )	Density ( $\text{g}/\text{cm}^3$ )	Thickness ( $\mu\text{m}$ )	Density ( $\text{g}/\text{cm}^3$ )
0.82	2.10	-	-
2	2.10	-	-
3	2.10	-	-
6	2.09	-	-
12.5	2.10	-	-
16	2.09	17	2.09
25	2.07	25	1.93
35	2.08	40	1.78
50	2.06	-	-

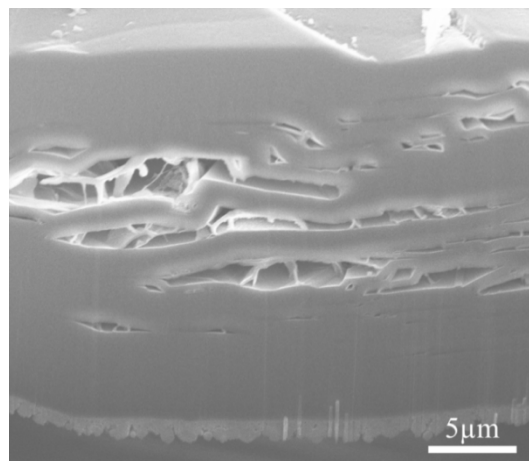


**Figure 3-18.** SEM cross-section image of PGS (25  $\mu\text{m}$ ). The presence of large number of air-pockets would gradually decrease the thermal conductivity by decreased density of the film.

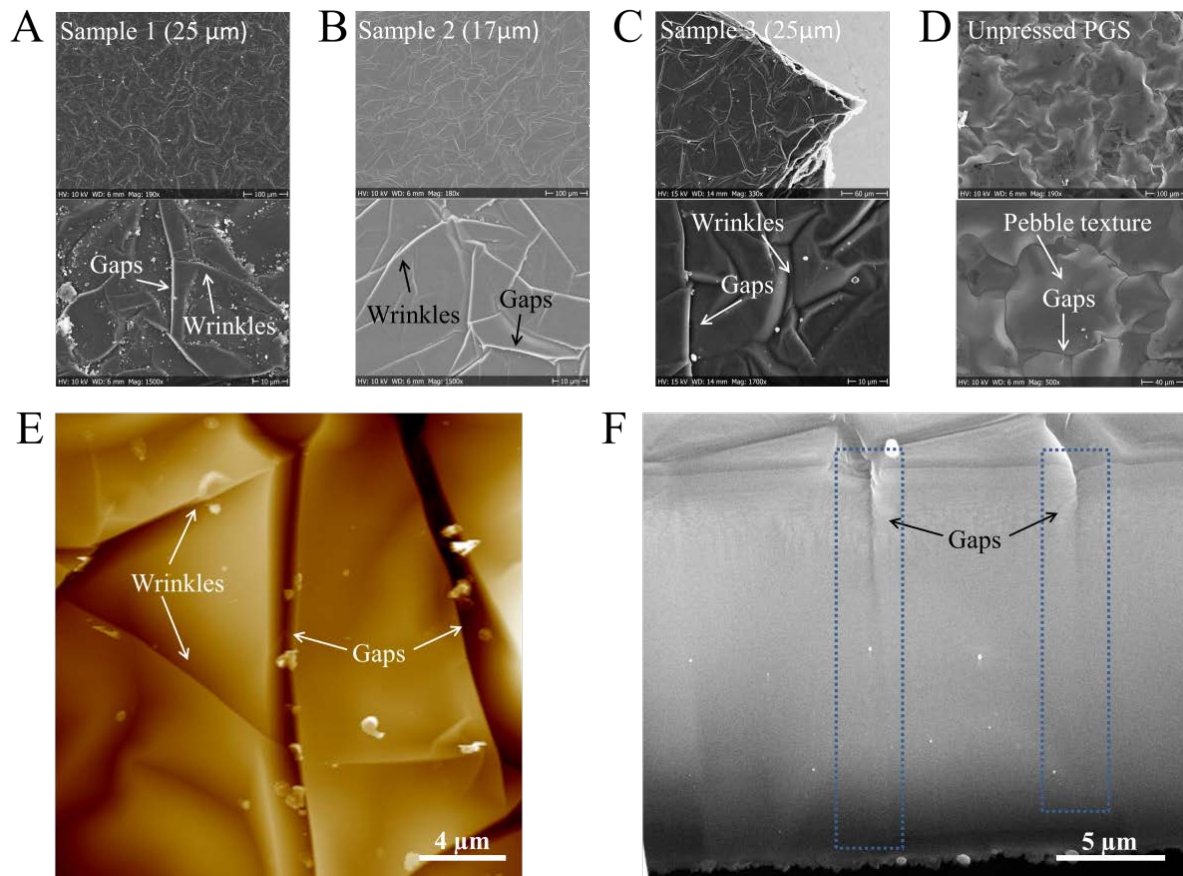


**Figure 3-19.** (A to C) SEM surface morphology images of commercial PGSs from different suppliers. It can be found that surfaces of all these PGS samples are filled with large amounts of wrinkles and gaps. (D) The surface morphology of unpressed PGS reveals that those wrinkles and gaps are mainly located at the boundary of pebble-like structures which were generated during the pyrolytic process. (E) AFM image of PGS showing the presence of wrinkles and gaps on the surface of PGS. (F) Cross-section SEM image of PGS.

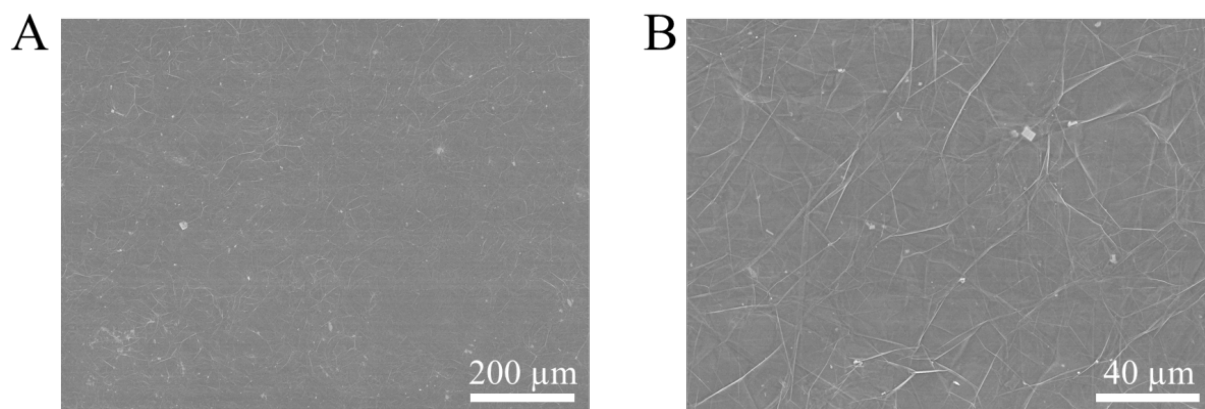


**Figure 3-20.** (A, B) SEM images of surface morphology of GF-2850°C after pressing showing a highly smooth surface.

GF-2850°C is also superior to most of commercially available high-thermal conductive materials. For example, it is over 12 and 8 times higher than that of aluminum and copper, respectively, and more than 2 times higher than graphite film produced by compressing natural highly oriented graphite flakes (300-1000 W/mK) [129]. Notably, the thermal conductivity of GF-2850°C even outperformed the best commercial PGS sample by 60%, showing the outstanding thermal performance as a novel high thermal conductive material.

### 3.1.4 GFs as superior heat-spreading material

To further demonstrate the superior thermal conductivity of GF-2850°C, we visualized the heat transfer along a sample strip in a homebuilt thermal testing platform, and compared the results to different highly thermally conductive materials, such as PGS, aluminum and copper foil. For testing, the samples were cut into long strips, coated with a thin layer of amorphous carbon to ensure consistent emissivity of the surfaces, and installed as a bridge for heat transfer between a heater and an aluminum heat sink (Figure 3-21a).

To compare the heat spreading capabilities between the different materials, we used sample strips of the same thickness of 25  $\mu\text{m}$  (Figure 3-21b-c). We found that GF-2850°C outperformed all tested highly thermally conductive materials, such as PGS, aluminum and copper foils. In particular, the temperature at the heater could be reduced from 82°C for aluminum to 37°C using GF-2850°C.

In order to demonstrate that by using the more thermally conductive GFs, the thickness of the heat spreading material can be decreased, we compared GF-2850°C samples with thicknesses of 0.8 and 2  $\mu\text{m}$  to 10  $\mu\text{m}$  thick aluminum foil (Figure 3-21d-e). We found that the 0.8  $\mu\text{m}$  thick GF-2850°C sample showed almost the same temperature profile and heat spreading capability as the 10  $\mu\text{m}$  thick aluminum foil. Based on the profile, the thermal

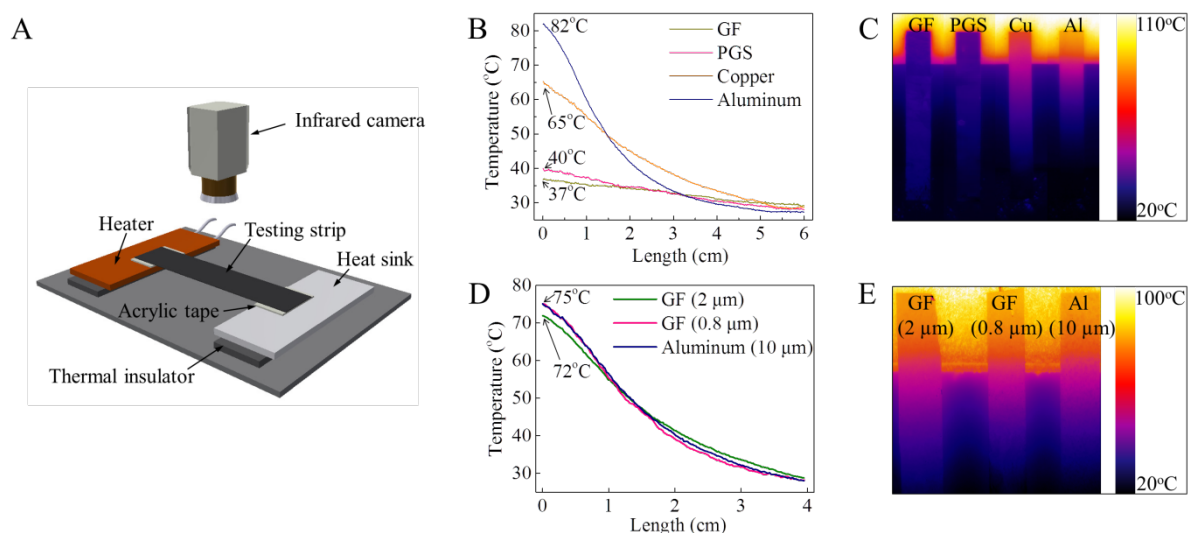


**Figure 3-21.** Demonstration of GFs as novel heat spreaders. (A) The sketch of thermal testing platform. (B to C) Temperature profiles of 25  $\mu\text{m}$  thick GF-2850°C, PGS, copper and aluminum foils (B) together with their IR images (C). (D to E) Temperature profiles of 0.8  $\mu\text{m}$  and 2  $\mu\text{m}$  thick GF-2850°C and 10  $\mu\text{m}$  aluminum foil (D) together with their IR images (E).

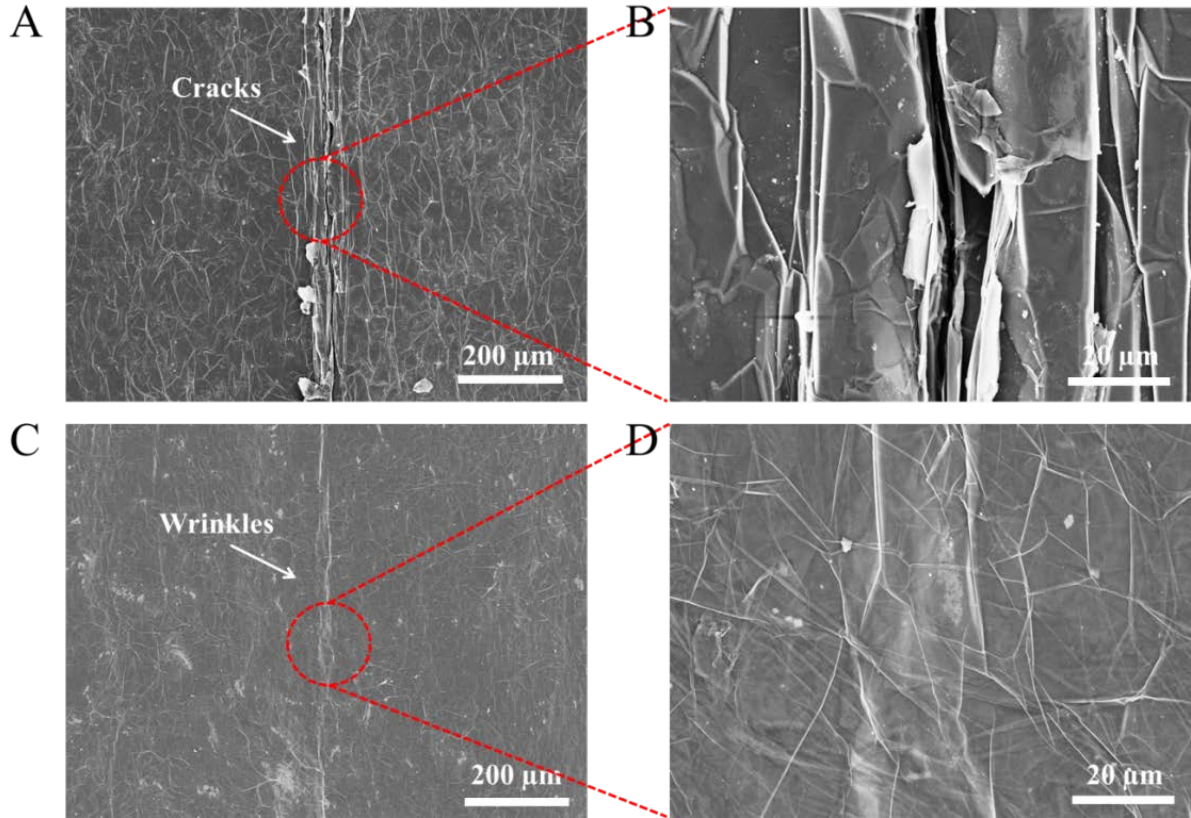


**Figure 3-22.** SEM images of surface morphology change of PGS (A-B) and GF-2850°C (C-D) after 10 times of folding/releasing tests. It can be found that clear breakages appeared on the surface of PGS while GF-2850°C maintained a good structural integrity after the folding test.

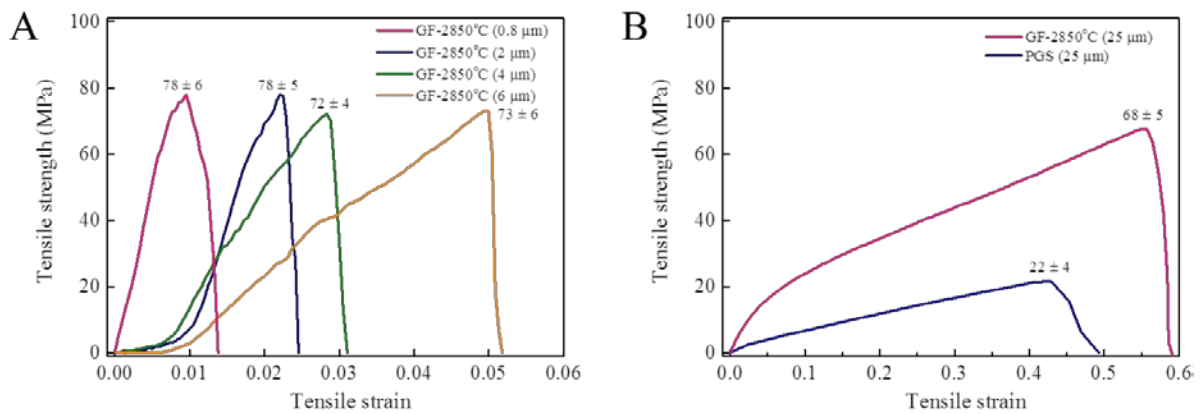


**Figure 3-23 (A)** Tensile strength of GF-2850°C with different thicknesses in the range of 0.8-6 μm. GF-2850°C with the thickness of 1-2 μm shows the highest tensile strength of 78 ± 6 MPa among all the tested samples. With the increase of the thickness, the tensile strength of GF-2850°C shows a slight decrease till 73 ± 6 MPa. (B) Tensile strength of GF-2850°C and PGS at the thickness of 25 μm. The tensile strength of GF-2850°C is 68 ± 5 MPa which is three times higher than PGS which only has a tensile strength of 22 ± 4 MPa.

**Table 3.2.** Tensile strength of GF-2850°C with different thicknesses and PGS with a thickness of 25  $\mu\text{m}$

Samples	Tensile strength (MPa)			Average tensile strength (MPa)
GF-2850°C (0.8 $\mu\text{m}$ )	78	72	83	$78 \pm 6$
GF-2850°C (2 $\mu\text{m}$ )	73	82	79	$78 \pm 5$
GF-2850°C (4 $\mu\text{m}$ )	68	72	75	$72 \pm 4$
GF-2850°C (6 $\mu\text{m}$ )	79	67	73	$73 \pm 6$
GF-2850°C (25 $\mu\text{m}$ )	64	68	73	$68 \pm 5$
PGS (25 $\mu\text{m}$ )	22	19	26	$22 \pm 4$

conductivity of 0.8  $\mu\text{m}$  thick GF-2850°C was calculated to 2875 W/m K, which was more than 12 times higher than that of aluminum, and is consistent with the previous thermal conductivity measurement. When the film thickness of GF-2850°C was increased to 2  $\mu\text{m}$ , it was found to even have a smaller temperature gradient than the 10  $\mu\text{m}$  aluminum foil and the surface temperature on the heater decreased by about 3°C compared to that of aluminum. These results show the outstanding thermal performance of ultra-thin GF-2850°C as a novel heat spreading material, which can offer new heat dissipation solutions for products where space (form-factor), for instance, is a critical parameter.

### 3.1.5 GFs are flexible and have superior mechanical strength

In order to investigate the mechanical properties of the GF-2850°C sample, we performed bending tests, determined tensile strengths, and compared the results to PGS. The bending test was carried out on an endurance testing machine, and we found that GF-2850°C exhibited excellent flexibility and reliability over 60000 cycles of 180° bending/releasing without any fractures. Folding tests were utilized to compare the flexibility of GF-2850°C with the PGS. We found that clear breakages appeared on the surface of the PGS while GF-2850°C maintained a good structural integrity after ten cycles of folding/releasing (Figure 3-22).

Tensile strengths of GF-2850°C with different thicknesses have been measured and compared to the PGS by using a high precision load/displacement measurement machine with a strain rate of 5 mm/s (Figure 3-23 and Table 3.2). GF-2850°C with the thickness of 1-2  $\mu\text{m}$  showed a maximum tensile strength of  $78 \pm 6$  MPa among all the tested samples. With the increase of the thickness, the tensile strength of GF-2850°C showed a slight decrease by 1-5 MPa due to the increased amount of air pockets (Figure 3-23a). Moreover, the tensile strength of GF-2850°C at the thickness of 25  $\mu\text{m}$  was found to be three times higher than that of PGS of the same thickness (Figure 3-23b).

To conclude, the GF-2850°C demonstrates good flexibility and high mechanical strength, and the significant improvement in mechanical strength compared to PGS is assumed to be a consequence of the presence of turbostratic-stacking graphene in GF-2850°C which allows the free movement of carbon atoms [111].

### **3.1.6 Conclusions**

The reported method offers a versatile and scalable approach to fabricate graphene films with high thermal conductivity, which can be used as heat spreading material in a wide range of applications. We estimate the annual production capability of GFs with the current setup to be approximately 2400 m<sup>2</sup> based on 240 working days per year with a production size of 2.5 m<sup>2</sup> per batch. For instance, a 10 μm film can be produced within two hours.

We have demonstrated that the developed large-scale GFs production process is superior to many other reported methods. For example, vacuum filtration of graphene suspensions [115,132,133], a typical method to fabricate GFs, exhibits an extremely low efficiency after a few seconds. Another method to fabricate GFs is electrospinning [129], which is a very complex process involving many GO pretreatment steps and the use of toxic and unrecyclable organic solvents. The wet-spun method [134] utilizes the coagulation/precipitation effects of GO in calcium chloride solutions to fabricate GFs, but it can introduce a lot of impurities in the films, which are difficult to remove, and cause adverse effects in the thermal performance of GFs. Also GFs fabricated by dip coating [135], inkjet printing [136] and spin coating [137] exhibit various short-comings such as difficulties in detaching them from the substrates. The shortcomings of previously reported methods have been overcome here by using the optimized self-assembly of GO sheets, in combination with high-temperature thermal reduction and pressing, thus providing a simple, clean, efficient and scalable process for the production of GFs. The resulting firm, large-grain and partly turbostratic-stacking GFs have outstanding thermal as well as mechanical properties. Specifically, the thermal conductivity reported here is the highest value reported so far for freestanding thin film structures assembled by graphene and superior to most of the commercially available thermal conductive materials. For example, the achieved thermal conductivity value is over 12 times and 8 times higher than that of aluminum and copper respectively and even outperforms the best commercial PGS sample by over 60%. This value also represents more than 100% improvement as compared to the best data of similar GF structures that ever reported in previous studies [129,131]. We believe that the in-plane thermal conductivity of GF-2850°C can further be improved by carefully tailoring its microstructures, such as increasing the relative volume of turbostratic-stacking graphene by employing large monolayer GO sheets as initial self-assembling material.

Taken together, the findings pave the way for large-scale production of high-thermal-conductivity GFs that could be deployed as efficient heat spreading materials in form-factor driven electronics and other high power driven system

## **3.2 Non-covalent functionalization of graphene for high thermal conductive adhesive**

Metal-based thermal conductive adhesive (TCA), also called as “polymer solder”, has been considered as one of the most promising alternatives of tin-lead solder alloys in electronic packaging areas due to many of its superior advantages, such as environmental

friendliness, lower operating temperature, fine pitch interconnect capability and cost-efficient processes[138,139]. However, in spite of all these merits, TCA still cannot entirely replace the use of tin-lead solder alloys, especially in some high-power applications requiring efficient heat dissipation capability, because of TCAs' relatively low thermal conductivity. Recently, considerable researches have been carried out to improve thermal performance of TCAs. All kinds of high thermal conductive materials have been fabricated and utilized as fillers of TCAs, such as carbon nanotubes (CNTs)[140,141], carbon nanofibers[142], silver nanowires [143]and graphene[144]. Among all the alternatives, graphene, as a two-dimensional nanomaterial, shows great advantages on improving thermal conductivity of TCAs. For example, graphene is composed by one or few atomic layers of  $sp^2$ -bound hexagonal carbon lattice. This structure allows phonon transfer inside graphene to be extremely efficient and leads to an outstanding in-plane thermal conductivity of about 5000 W/mK[145]. In addition, graphene possesses large surface areas, which can conduct large amount of the heat pathways inside polymer resin to improve the heat dissipation rate[146].

The quality of graphene is essential for the thermal performance of the TCAs. Any defects and impurities can significantly decrease thermal conductivity of graphene, and lead to poor thermal enhancement to TCAs. There are many different methods that are widely used for fabricating graphene, such as chemical exfoliation, peeling-off by scotch tape, chemical vapor deposition, and mechanical exfoliation. Taking into consideration of their quality, efficiency, and cost, mechanical exfoliation process shows great potentials.

Here, we fabricated stabilizer-free and few-layer graphene nanosheets and utilize them as fillers to improve the thermal conductivity of silver based TCAs. To overcome the interlaminar van der Waals' force between graphite layers, the exfoliation of graphene was carried out by shear mixing of graphite flakes in a mixed solvent which has the similar surface energy between the solvent and graphene nanosheets, Due to the good surface energy matching, graphite flakes could be fast and efficiently exfoliated into individual layers and uniformly dispersed in the solvent. Compared to many reported processes, the fabrication process developed in this thesis shows great advantages, such as high process efficiency, mass production, low-cost, clean and safe process.

The fabricated graphene was used together with silver flakes as hybrid fillers to improve TCA's thermal conductivity. Meanwhile, to minimize the adverse effect of nanofillers to TCA's viscosity, the molecule structures of TCAs was optimized to decrease the interaction strength with graphene nanosheets. The developed graphene enhanced TCA shows the advantages of high thermal conductivity, lower density, good dispensing ability and cost effective, suggesting its potential application in thermal management of power devices and electronic packaging area

### **3.2.1 Mechanical exfoliation of graphene**

The appropriate selection of solvent is essential for the liquid exfoliation process of graphite. Previous researches reported that liquid exfoliation of graphite can only occur when the mixing enthalpy between graphite and solvents is very small[147]. Equation 1 describes the relation between the mixing enthalpy and material properties:

$$\frac{\Delta H_{mix}}{V_{mix}} \approx \frac{2}{T_{flake}} \left( \sqrt{E_{Sur}^G} - \sqrt{E_{Sur}^{Sol}} \right)^2 \Phi \quad (1)$$

Where  $\Delta H_{mix}/V_{mix}$  is the enthalpy of mixing (per unit volume).  $T_{flake}$  is the thickness of the fabricated graphene nanosheets and  $\Phi$  is the volume fraction of graphene.  $E_{Sur}^G$  and  $E_{Sur}^{Sol}$  are the surface energy of graphene and solvents respectively. The equation shows that the liquid exfoliation process is strongly dependent on the balance of graphene and solvent surface energies. For graphene,  $E_{Sur}^G$  is defined as the required energy for overcoming the Van der Waal's force between the adjacent graphite layers. According to many reports in literature, the surface energy of graphene is about 70-80 mJ/m<sup>2</sup>[147–149]. Therefore, the ideal solvents need to have a similar surface energy as graphene. For solvents,  $E_{Sur}^{Sol}$  is commonly related to their surface tension values, as shown in Equation 2:

$$r = E_{Sur}^{Sol} - TS_{Sur}^{Sol} \quad (2)$$

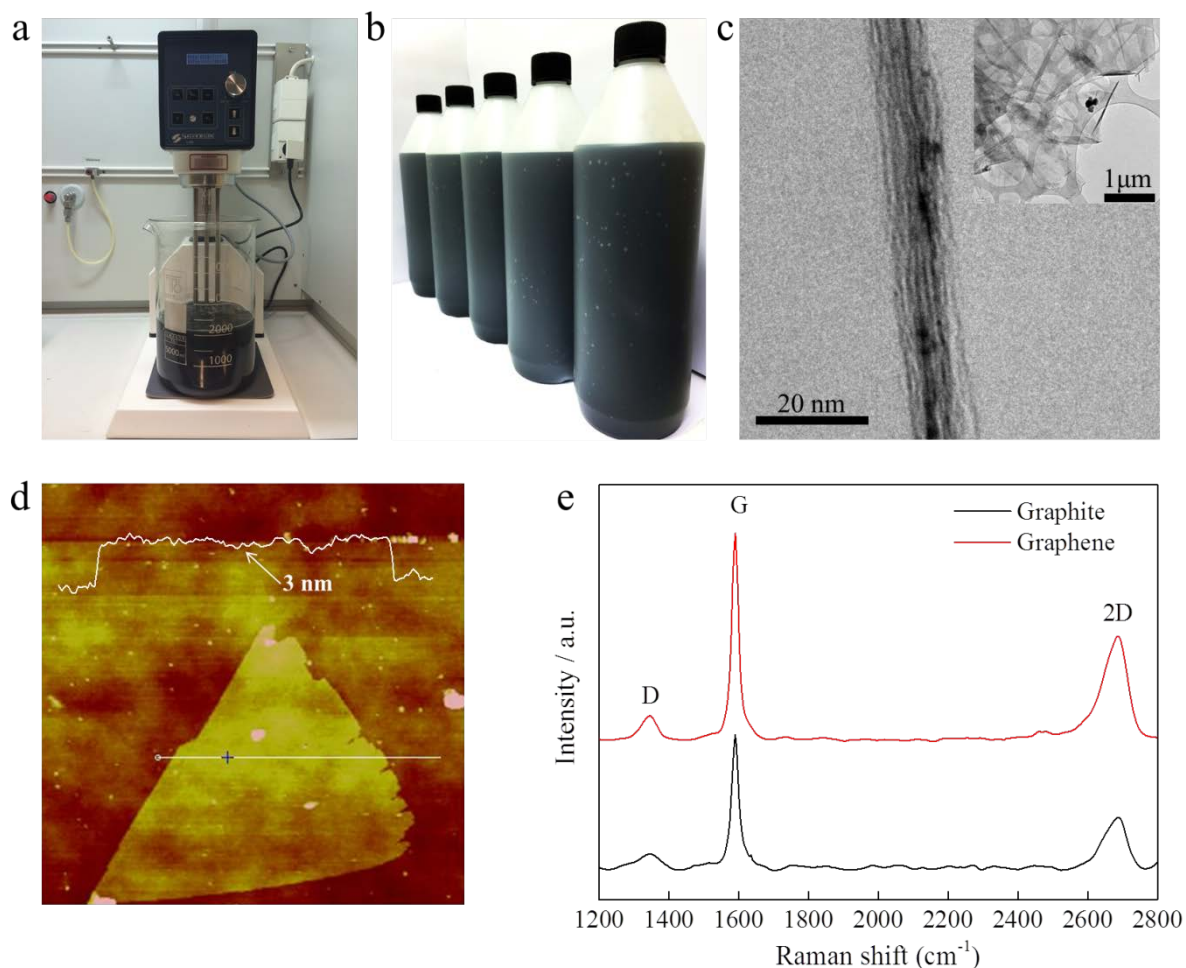
Where  $r$  is the surface tension of solvents,  $T$  is the temperature and  $S_{Sur}^{Sol}$  is the solvent surface entropy which has a universal value about 0.1 mJ/m<sup>2</sup>K for most of the solvents[150]. Therefore, the desirable solvents should have a surface tension value in the range of 40-50 mJ/m<sup>2</sup>. Table 3.3 shows the surface tension values of many common solvents. To fabricate graphene nanosheets in a clean and safe way, the solvents used for the liquid exfoliation process not only need to meet the surface tension requirement, but also should be easily removable (low boiling point) and safe for the operators (lower risk). From Table 3.3, we find that some solvents, such as benzyl benzoate, NMP, GBL and DMF (90%) aqueous solution, show appropriate surface tension values fitting in the range of 40-50 mJ/m<sup>2</sup>. However, these solvents are difficult to remove from graphene due to their relatively high boiling points. Consequently, the solvent residuals can lead to the deterioration of graphene's thermal and electrical conductivities[151]. Furthermore, the using of these solvents in mass production is not safe for both human and environment. The other solvents which have lower boiling points, such as IPA, ethanol, acetone and water, cannot meet the requirement for the surface tension. To solve the problem, a mixed solvent consisting of ethanol and water was used for liquid exfoliation in this work. An appropriate surface tension value of 46.0 mJ/m<sup>2</sup> was shown by the mixed solvent when the ethanol weight percentage reaches to 11%. This is an ideal value for the liquid exfoliation of graphite. Importantly, the mixed solvent is also easily removable and very safe for the operators.

Figure 3-24a-b show the optical images of the graphene-ethanol aqueous dispersions produced by using the high-speed shear mixer. These dispersions have an average graphene concentration of 40 µg/ml. For each batch, the shear mixer could produce maximally 12 L of the graphene-ethanol aqueous dispersion, indicating the potential for the mass production of graphene. The high exfoliation efficiency of the shear mixer was attributed to the super high shear rate ( $>10^4$  s<sup>-1</sup>) generated by the head of the mixer. During rotation, graphite flakes were sucked into the mixing head and driven towards the edge of the rotor/stator. The intense local shearing rate between the rotor and stator led to the collision and exfoliation of graphite flakes. Compared to the commonly used ultrasonication methods, the high-speed shear mixing approach has many advantages, such as high efficiency, low power consumption, minimum temperature increase, and mass production.

Figure 3-24c shows the TEM images of the fabricated graphene. From the insert image, it

**Table 3.3.** The surface tension values, boiling points and risk categories of common solvents.

Solvent	Surface tension (mJ/m <sup>2</sup> )	Boiling points (°C)	Risk category
Benzyl benzoate[152]	46.0	323	High
NMP (N-Methyl-2-pyrrolidone)[153]	40.1	204	Very high
GBL ( $\gamma$ -Butyrolactone)[154]	46.5	204	High
DMF (Dimethylformamide)(90%) + Water[155]	40.6	154	Very high
Water[147]	72.0	100	Low
IPA (Isopropanol)[147]	21.7	82.6	High
Ethanol[147]	22.3	78.4	High
Acetone[147]	23.7	56	High
Ethanol (11%) + Water	46.0	78.4 ~100	Low



**Figure 3-24.** (a-b). Optical images of the graphene-ethanol aqueous dispersions produced by using the high-speed shear mixer. (c) TEM images of the fabricated graphene. The insert image shows overlapped graphene nanosheets with folded edges. (d) AFM image of the graphene nanosheets. (e) Raman spectrum of graphene and graphite.

can be found that the overlapped layer structure is composed of many individual graphene nanosheets with folded edges. The black spots attached to the surface of graphene could be amorphous carbon. At higher magnification, the parallel lines oriented in the same direction are the cross-sections of the graphene nanosheets, indicating the multi-layer structure of the graphene nanosheets. Figure 3-24d shows the AFM image of the graphene nanosheets. From the image, it is observed that the graphene nano-sheet has a lateral size of 2-3  $\mu\text{m}$  and the thickness of the graphene nanosheets is about 3 nm. This result shows that the number of graphene layers is less than 10. Raman spectroscopy was used to examine the quality of the obtained graphene nanosheets. As shown in Figure 3-24e, the Raman spectrum of graphene exhibits three characteristic peaks, including D peak at  $1350\text{ cm}^{-1}$ , G peak at  $1589\text{ cm}^{-1}$  and 2D peak at  $2686\text{ cm}^{-1}$ . The D peak shows the presence of defects which could be derived from the graphite precursor since the same D peak appeared in the graphite spectrum. And the G peak associating with the ordered graphitic lattice keeps a sharp peak with almost identical position and width as graphite, indicating the good graphitic crystalline structures. The D/G peak intensity ratio ( $I_D/I_G$ ) corresponding to the defect change is about 0.12, which is much less than most chemical reduction graphene[156,157]. In addition, the 2D peaks of graphene and graphite have almost the same position and shape, further indicating that the obtained products are few-layer graphene. This is because the change of 2D peak becomes hard to distinguish in Raman spectra when graphene have more than 5 atomic layers[158]. Therefore, all these results show that the high speed shear mixing approach can successfully produce high quality and few layer graphene in the ethanol aqueous solution.

### 3.2.2 Thermal performance of graphene enhanced TCAs

Generally, TCA consists of conductive fillers providing electrical and thermal conductivities and polymer matrixes giving mechanical support. The polymer matrix used in this work is specially designed by adjusting the proportion of each component, such as epoxy resin, curing agent, diluents and various additives, to maintain a very low initial viscosity. Different G-TCA samples with varied graphene weight percentages were fabricated. To be clear, all G-TCA samples have the same filler weight percentage (76 wt%), and graphene powders were used to partly replace the silver proportion. The weight percentage of graphene was varied in the range of 0.1-3 wt%. Even higher weight percentages are not interested in this work due to the dramatically increased viscosities caused by Nano-fillers. Thermal conductivity values of different G-TCA samples were measured by Laser-Flash technics, and the results were shown in Figure 3-25a. It can be found that thermal conductivity values of G-TCA samples increase with the increase of graphene ratios. The TCA sample with 3% graphene (TCA-3.0%G) shows the highest thermal conductivity about 8 W/m K, which is almost four times higher than reference TCAs (76% Ag). Figure 3-25b shows the thermal conductivity values of G-TCA samples at different working temperatures. All G-TCA samples were heated and measured from 20  $^{\circ}\text{C}$  to 100  $^{\circ}\text{C}$  by Laser-flash technic. In each temperature, G-TCA samples were measured for three times. It has been found that all G-TCA samples showed stable thermal conductivity values with a small variation less than 10%, indicating that graphene have good compatibility with the polymer matrix of TCA at the normal working temperatures.

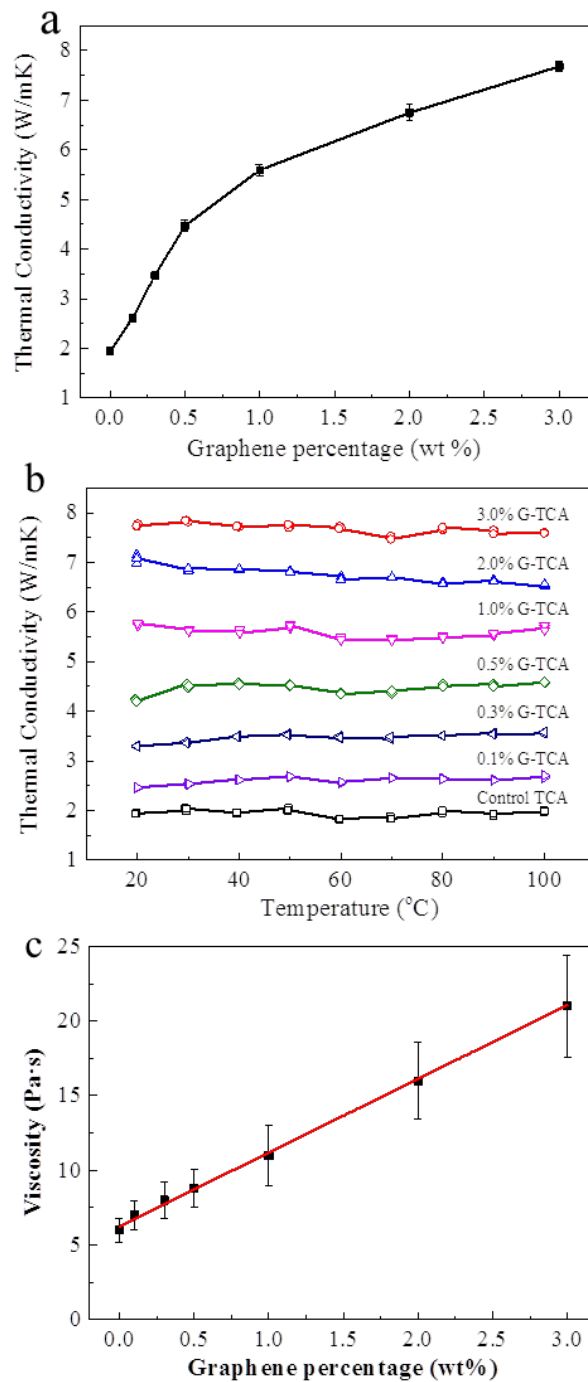


**Figure 3-25.** (a) Thermal conductivity values of G-TCA with different graphene percentages. (b) Thermal conductivity values of different G-TCA samples at different working temperatures (c) Viscosity change of G-TCAs as a function of graphene weight percentages

To realize automatic production, many electronic packaging/assembly lines require TCA to be easily dispensed. Therefore, it is essential to minimize the adverse effect of nano-fillers to the viscosity of G-TCA pastes. In this work, the polymer matrix was designed to have small surface interaction with graphene nanosheets. Figure 3-25c shows the viscosity change of G-TCAs as a function of graphene weight percentages. All G-TCA samples were tested under a rotating speed of 5 rpm at 20 °C. It has been found that the viscosity of G-TCAs increased almost linearly with the increase of graphene weight percentages. The G-TCA sample with 3 wt% of graphene shows the highest viscosity about 21 Pa·s. This value is still in the range of commercial TCA’s viscosity.

### 3.2.3 Demonstration

A Joule heating setup was built to simulate TCA’s function in a real electronic component and demonstrate the heat dissipation properties of the TCAs. As shown in Figure 3-26a, A TCA strip with a size of 50mm\*5mm\*2mm was mounted onto two pieces of copper blocks. The TCA strip was designed to have a large aspect ratio of 10 so that it could be assumed that the heat flow only happens in X direction and temperature in the other directions are homogeneous. The copper blocks are used as heat sinks to remove heat from TCA strips, which is a standard industrial strategy for cooling of power devices. During the test, a stable working power of 2.5 W was applied to the setup and generated a temperature profiles in the TCA strip. Two different samples were measured and compared, including control TCA and 3% G-TCA. The surface temperature profiles of TCA were recorded by the Infrared camera. The results are shown in Figure 3-26b-c, the temperature at the center point of the control

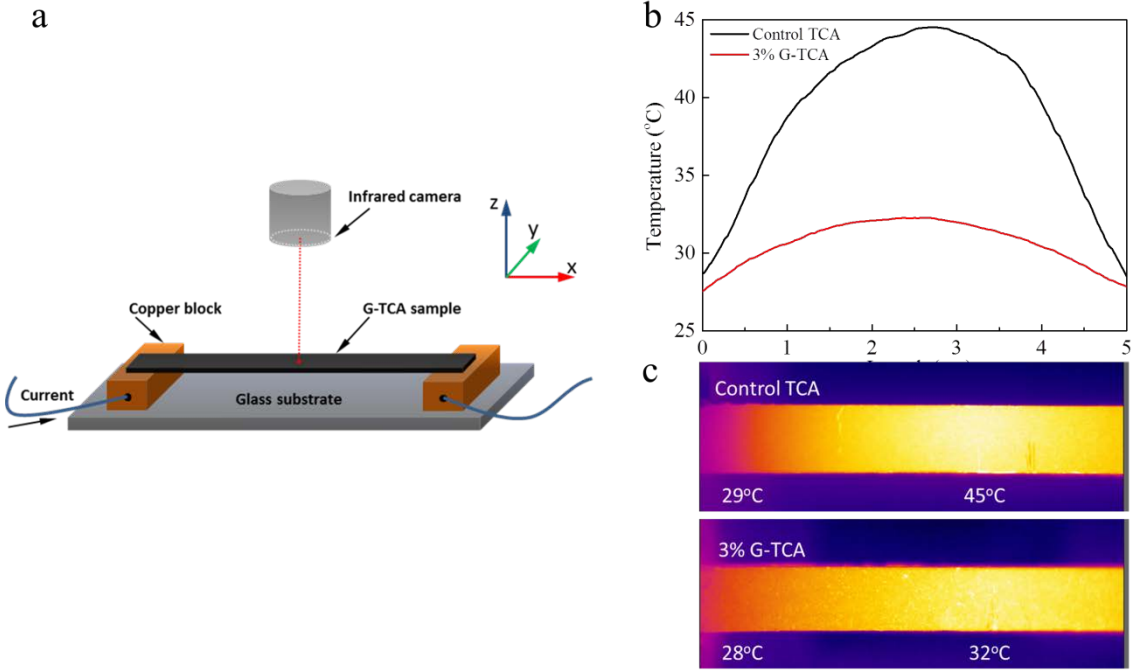


**Figure 3-26.** (a) The sketch of the Joule heating setup to demonstrate the heat dissipation properties of the TCAs. (b) The surface temperature profiles of TCAs recorded by the Infrared camera. (c) IR images of control TCA and 3% G-TCA.

TCA is 45°C. As a comparison, the 3% G-TCA has a central temperature of 32°C which is about 13°C lower than the control TCA. In particular, the temperature difference between the center and edge for the 3%G-TCA (4°C) is only one quarter the value of the control TCA (16°C). According to the four-probe measurement, the control TCA and 3%G-TCA have the same electrical sheet resistance (0.006  $\Omega/\square$ ), meaning that the total amounts of heat generated by the two TCA strips are equal. Therefore, the much smaller temperature difference of 3%G-TCA sample along the X direction represents its highly improved heat dissipation ability. This result was attributed to the presence of sufficient graphene nanosheets which could fill the interspaces caused by the irregular morphologies of silver flakes and improve the heat conduction through different fillers. Therefore, the G-TCA could be widely used for thermal management of many power devices to decrease their working temperatures and extend the useable life of the devices

### **3.2.4 Conclusions**

In this section, stabilizer-free and few-layer graphene nanosheets were fabricated through high-speed shear mixing of graphite flakes in a mixed solvent. The graphene fabrication process developed in this paper has many advantages, such as high process efficiency, mass production, low-cost, clean and safe process. The fabricated graphene was used together with silver flakes as hybrid fillers to improve TCA's thermal conductivity. TCA sample with a hybrid filler ratio of 73% Ag and 3% graphene shows the highest thermal conductivity of 8 W/m K, which is almost four times higher than reference TCAs. In addition, the developed G-TCAs possess low viscosities which facilitate making uniform and fine patterns with existing dispensing techniques. In general, the developed G-TCA has the benefits of high thermal conductivity, lower density, good dispensing ability and cost effective, suggesting its potential application in thermal management of power devices and electronic package.

## **3.3 Non-covalent functionalization of carbon nanotube for flexible electronic application**

Non-covalent functionalization processes utilize various functional molecules or active species as assembly mediators to functionalize the surface of CNMs via non-covalent interactions such as hydrophobic,  $\pi$ - $\pi$  stacking, and wrapping interaction. The assembled mediators would then act as binding points for anchoring other molecules or nanomaterials. Different from the covalent functionalization processes, the great advantage of non-covalent functionalization processes is to protect CNTs structure and properties from destruction. Therefore, there is a growing interest on development of non-covalent assembly processes. Here, a new surface modification process for synthesizing intrinsically flexible multi-functionalized CNT based hybrid nanowires is presented. The key benefit of the hybrid nanowire lies in their high electrical conductivity and flexible structures to maintain stable electrical and mechanical performances under significant structural deformation. The fabrication processes of multi-functionalized CNT based hybrid nanowires are schematically

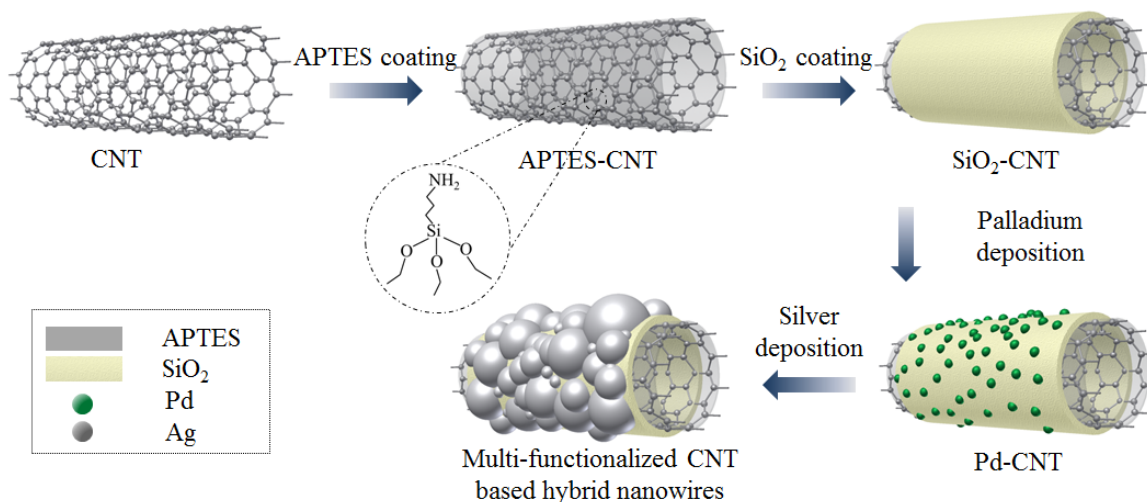


**Figure 3-27:** Schematic of the various modification steps in the synthesis of multi-functionalized CNT based hybrid nanowires. The surface of CNTs was coated with APTES, silica, palladium nanoparticles and silver nanoparticles.

illustrated in

Figure 3-27. The surface of CNTs was successively wrapped with firstly a cross-linkable (3-aminopropyl)triethoxysilane (APTES) layer, then a silica layer, followed by palladium nanoparticle and silver nanoparticle deposition. Every functional material in a hybrid nanowire has been specifically chosen for its beneficial properties: CNTs act as a flexible framework as well as additional electron pathways. APTES improves the dispersion of CNTs in polar solvents through bringing in hydrophilic silane and amino groups on the surface of CNTs. The mesoporous silica layer is used as templates for the attachment and deposition of metallic nanoparticles. Palladium nanoparticles served as catalysts to provide nucleation sites for silver growth. Finally, silver nanoparticles are the main conductive media to improve the contact surface of the hybrid nanowires and build high-efficiency conductive networks.

### 3.3.1 Functionalization of CNT surface by APTES and SiO<sub>2</sub>

Pristine CNTs have very large aspect ratios and highly inactive surfaces, which make them uneasy to form homogeneous and stable dispersion. To address such a challenge, the required surface activation of CNTs needs to be carried out. In previous reports, this was generally achieved through an oxidation pretreatment of CNTs or surfactant assisted separation processes[159,160]. However, such treatments always lead to severe structural damage as well as poor electrical and mechanical performance to CNTs. In this work, CNTs were coated with a cross-linked APTES polymer layer (APTES-CNTs). The large amounts of hydrophilic groups of APTES, such as Si-OH and -NH<sub>2</sub>, would assist CNTs to be homogeneously dispersed in polar solvents. Importantly, the APTES layer can be completely removed in the follow-up process without having any adverse effects on the CNT's properties. The reaction mechanism of forming APTES-CNTs is schematically illustrated in Figure 3-28a. CNTs exhibit a negatively charged surface in ethanol at high pH value (pH > 7), which can attract the positively charged APTES monomer through electrostatic absorption[161]. The attracted APTES monomers cross linked with each other under alkaline conditions and formed a

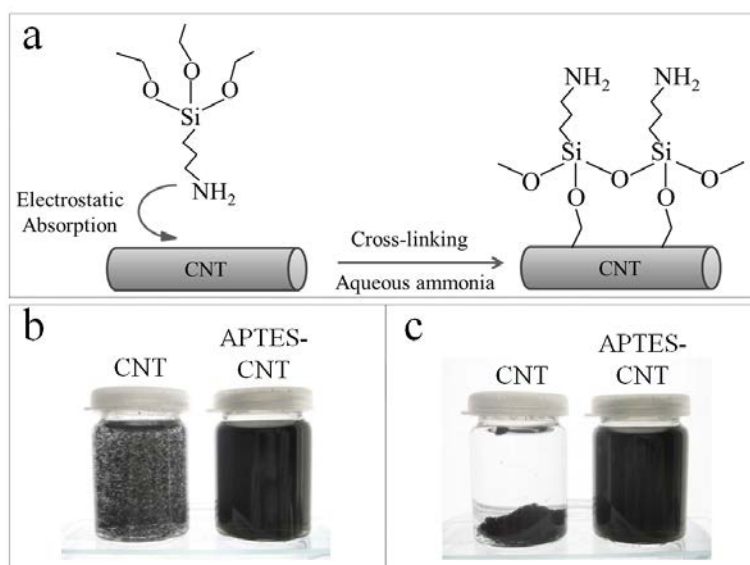


**Figure 3-28:** (a) The reaction mechanism of forming APTES layer on CNT surface. Positively charged APTES monomer could be attracted by the negatively charged CNTs through electrostatic absorption. Crosslinking of APTES monomers would take place under alkali condition, and an APTES coating layer can be formed at the surface of CNTs. (b) Dispersion of CNTs in ethanol before and after APTES coating. A homogeneous CNTs ethanol solution was obtained after modification with APTES. (c) Solution stability of CNTs in ethanol without and with APTES coating for the period of one month after preparation. No delamination or sediment was detected in the ethanol dispersion of APTES-CNTs.

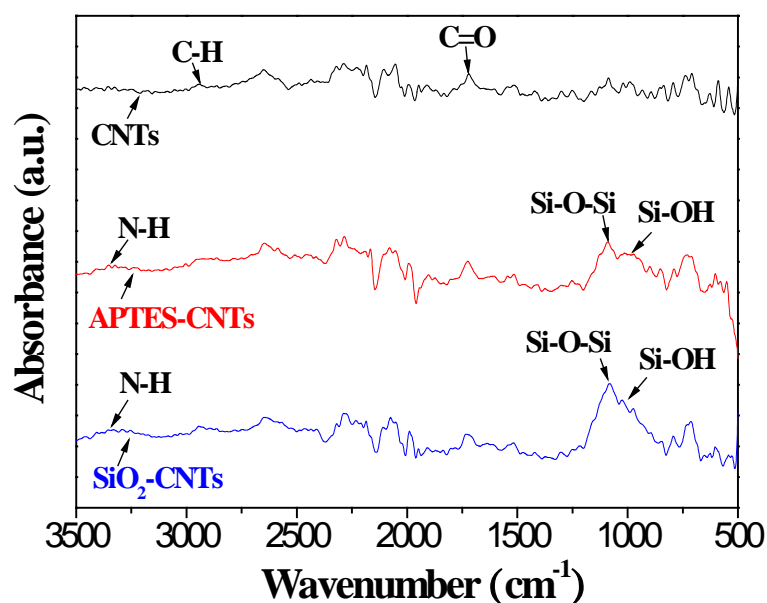


**Figure 3-29:** FTIR analysis of pure CNT, APTES-CNT and SiO<sub>2</sub>-CNT. Compared to the FTIR spectrum of pure CNT, APTES-CNT shows the Si-OH stretching and asymmetric Si-O-Si stretching peaks at 980 cm<sup>-1</sup> and 1080cm<sup>-1</sup> respectively, and also the N-H stretching peak between 3400-3500cm<sup>-1</sup>. After silica coating, the peak corresponding to Si-O-Si stretching becomes more intense in the spectrum of SiO<sub>2</sub>-CNT. These results indicate the successfully coating of APTES and silica layer.

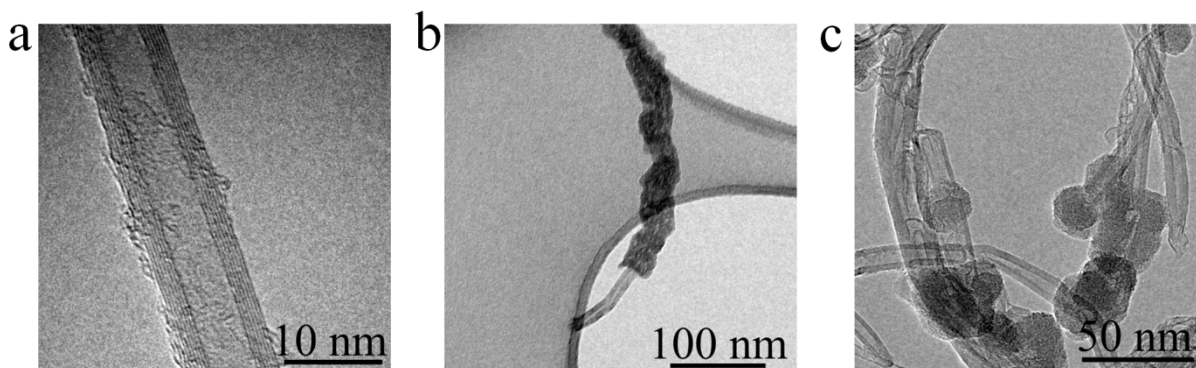


**Figure 3-30:** (a) A pure CNT with a diameter of 10nm. (b) SiO<sub>2</sub>-CNTs. An amorphous silica layer with a thickness about 10nm was deposited at the surface of APTES-CNTs. (c) Control experiment of silica coating directly on CNTs without APTES modification. A random and unselective SiO<sub>2</sub> deposition on CNTs with huge bundles was observed

coating layer on the surface of CNT. Figure 3-28b shows the difference of the CNT dispersions in ethanol before and after APTES coating. A homogeneous CNT ethanol solution was obtained after functionalizing with APTES. Additionally, the APTES-CNT suspension exhibits good stability for the period of one month after preparation (Figure 3-28c). No sediments were detected in the ethanol dispersion of APTES-CNTs, which indicates the effectiveness of the APTES coating onto the CNT surfaces.

After being functionalized with APTES, silica coating was carried out onto the surface of the CNTs (SiO<sub>2</sub>-CNTs) through the hydrolysis reaction of tetraethyl orthosilicate (TEOS) under alkaline conditions to act as templates for metal nanoparticles deposition[162]. FTIR was employed to confirm both the attachment of APTES and formation of SiO<sub>2</sub> around the composite (Figure 3-29). The peaks at 1700 cm<sup>-1</sup> and 2900 cm<sup>-1</sup> corresponding to C=O and C-H groups indicate that the CNT has defects due to the production processes used by the CNT supplier. After functionalizing with APTES, the peaks corresponding to Si-OH stretching and asymmetric Si-O-Si stretching appeared at 980 cm<sup>-1</sup> and 1080cm<sup>-1</sup> respectively. Moreover, a broad band located between 3400-3500cm<sup>-1</sup> represents N-H stretching of the amino group in APTES. After TEOS treatment, the peak corresponding to Si-O-Si stretching becomes stronger due to the formation of a silica layer.

Transmission electron microscopy (TEM) study was carried out to understand the morphology changes of CNTs before and after the silica coating process. The image of pure CNTs shown in Figure 3-30a indicates a smooth surface with a diameter of 10 nm. In comparison, a shell structure along the axial direction of the nanotubes can be observed from Figure 3-30b, which indicates a successful silica coating on the CNT. The thickness of the silica shell was found to be about 10 nm which can be varied through changing the concentration of TEOS. The impact of the APTES layer to the silica coating was also examined via a control experiment of coating the silica directly on CNTs without APTES modification layers. It has been found that the deposition of SiO<sub>2</sub> was random and individual CNTs tended to form big bundles (Figure 3-30c). Therefore, it can be inferred that APTES layers were not only assisting the dispersion of CNTs, but also acting as an adhesion layer for the silica coating process.

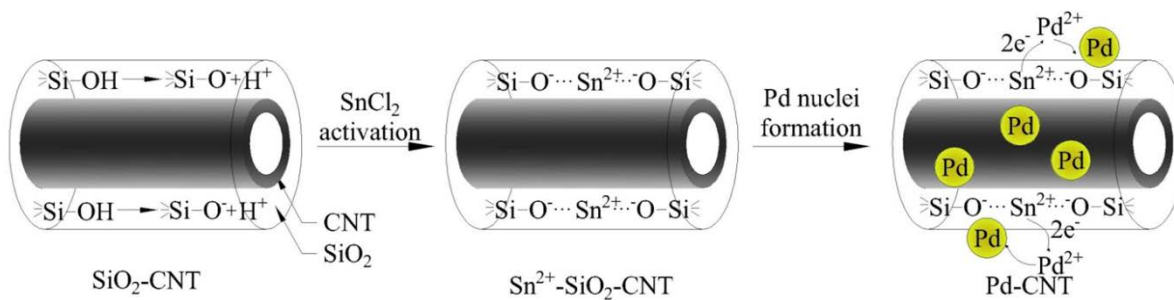


**Figure 3-31:** Reaction mechanism of palladium nanoparticles deposition in silica layer.

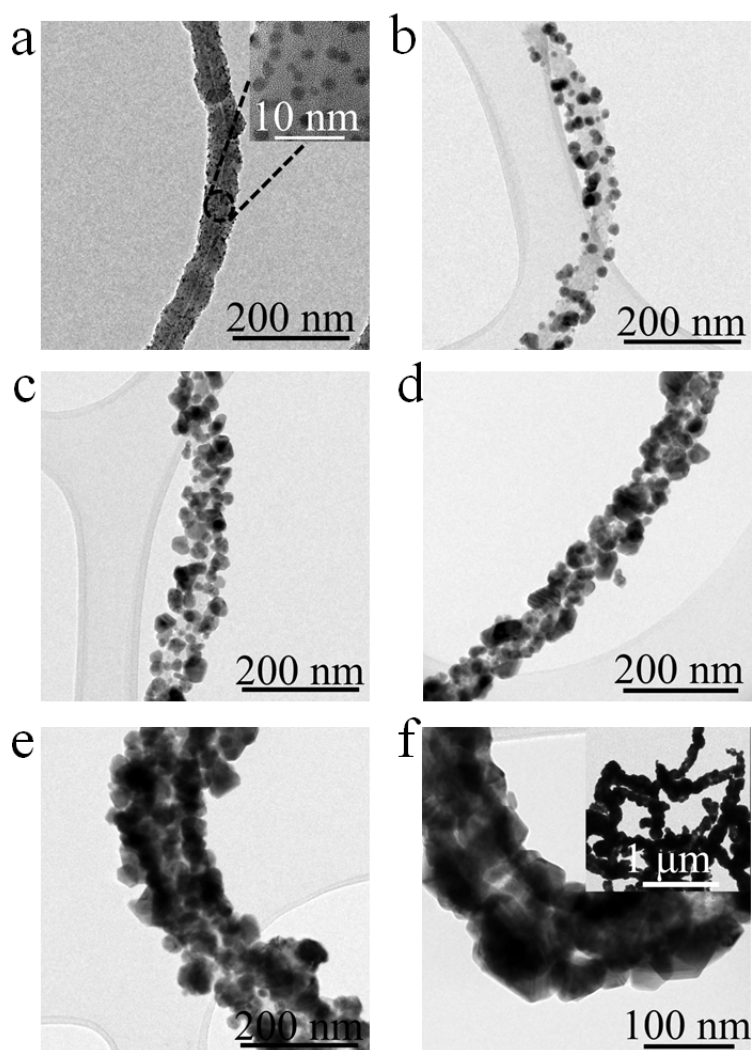


**Figure 3-32** (a) Pd-CNTs. Dense and uniform palladium nuclei were deposited in silica layer and no free particle were observed. The inset shows that the average size of palladium nuclei is about 3nm. (b-f) Multi-functionalized CNT based hybrid nanowires prepared with different silver nitrate concentrations. b: 1 g/L; c: 2 g/L; d: 5 g/L; e: 10 g/L; f: 15g/L, the inset shows the zoom out image of hybrid nanowire connection.

### 3.3.2 Deposition of silver nanoparticles on the functionalized CNTs

The SiO<sub>2</sub> layer exhibits a strong binding ability with positively charged ions due to the attraction of Si-OH group, and also a mesoporous structure which would facilitates the targeted metal nanoparticle growth[163,164]. Figure 3-31 illustrates the deposition of palladium nanoparticles on CNT (Pd-CNTs). Metallic palladium (Pd) nanoparticles were generated through the reduction of Pd<sup>2+</sup> ions by Sn<sup>2+</sup> ions which were pre-trapped in the silica layer.

TEM image in Figure 3-32a shows the morphology change of CNT after palladium deposition. A large quantity of Pd nanoparticles with an average particle size of 3nm was uniformly deposited in the SiO<sub>2</sub> layer. Those Pd nanoparticles would act as nucleation sites for the proceeding silver growth on CNTs. Finally, multi-functionalized CNT based hybrid nanowires were obtained through electroless silver plating. Mild reaction conditions were maintained during silver nanoparticle growth to ensure the uniform and complete silver deposition on the CNTs. The degree of silver nanoparticles coverage on the CNT surfaces was found to be very critical for optimizing the electrical performance of the hybrid nanowires. Hence, a series of multi-functionalized CNT specimens were prepared with increased silver nitrate concentrations from 1 g/L to 15 g/L to study the effect of silver nitrate concentration on the metallic coverage of the CNTs. TEM observation shows that the morphologies of the CNTs changed as the silver nitrate concentrations were varied (Figure 3-32b-f). When a lower

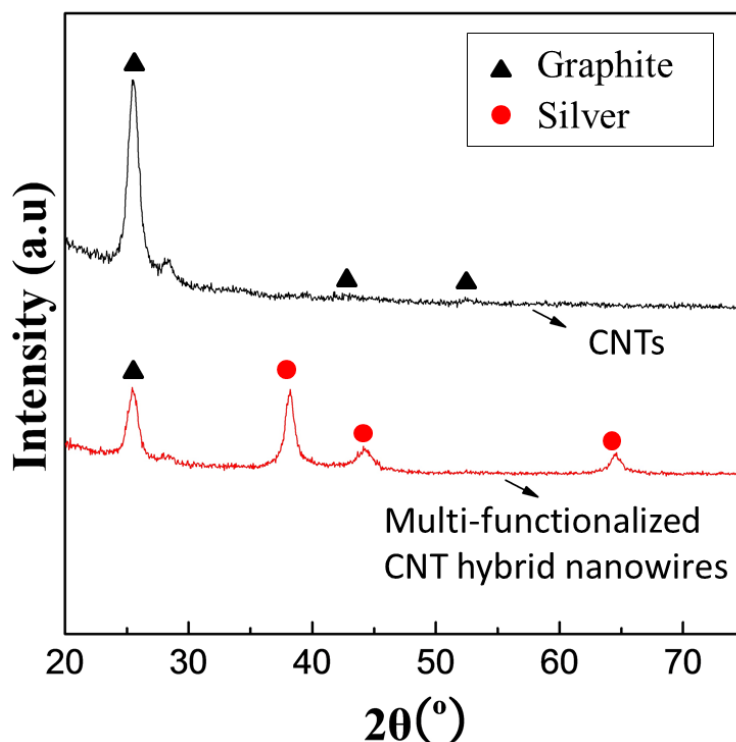


**Figure 3-33** XRD patterns for pristine CNTs and the multi-functionalized CNT hybrid nanowires respectively. Peaks located at 38.2°, 44.4° and 64.5° in the sample of multi-functionalized CNT hybrid nanowires are referred to the (111), (200) and (220) planes of the fcc structure of metallic silver, and also the diffraction peak at 26.5° is referred to (002) of graphite.

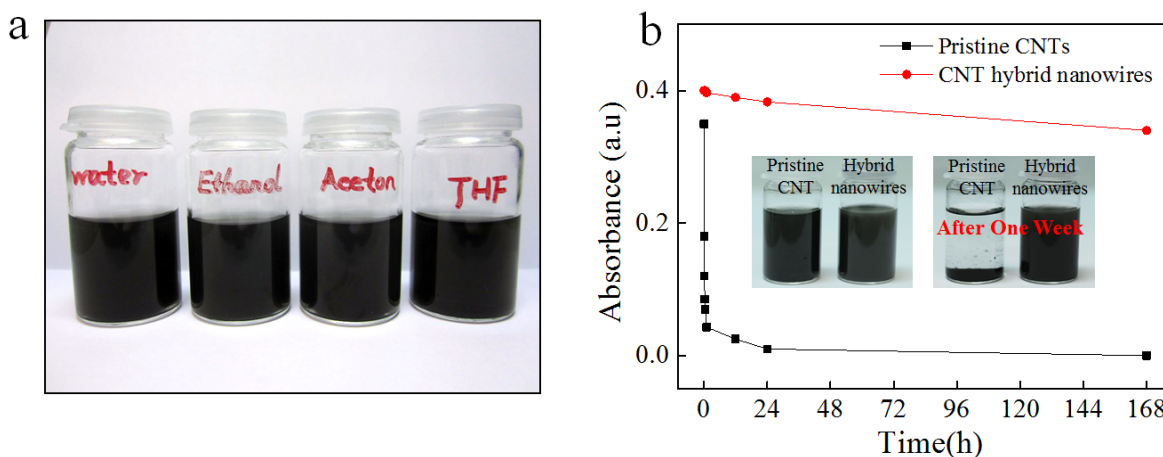
silver nitrate concentration (1 g/L) was used, small silver nanoparticles with an average size of 20 nm were formed due to presence of inadequate silver precursor sources (Figure 3-32b). Upon increasing the concentration of silver nitrate from 1 g/L to 10 g/L, the average size of silver nanoparticles was increased from 20 nm to 50 nm with an enlarged surface coverage (Figure 3-32c-e). When the silver nitrate concentration reaches to 15 g/L (Figure 3-32f), a layer of densely packed silver nanoparticles was formed around the whole CNTs surface. No free silver nanoparticles or obvious agglomerations were detected after using a higher silver nitrate concentration.

Figure 3-33 shows the XRD patterns for pristine CNTs and the multi-functionalized CNT hybrid nanowires respectively. Peaks located at  $38.2^\circ$ ,  $44.4^\circ$  and  $64.5^\circ$  in the sample of multi-functionalized CNT hybrid nanowires are referred to the (111), (200) and (220) planes of the fcc structure of metallic silver, and also the diffraction peak at  $26.5^\circ$  is referred to (002) of graphite. The XRD pattern of Ag-CNTs hybrid nanowires indicates that the silver nanoparticles deposited over the CNT surface have a highly pure crystallinity. These results show advantages of our process on both protecting CNT's structure and coating complete metallic nanoparticle layers compared with the previous reports[165–167].

### 3.3.3 Fabrication of flexible and stretchable electrical circuits

As the demands of modern electronic systems call for increasing functionality, smaller system size, higher device connectivity, better user experience, and all at lower cost, flexible and stretchable circuits (FSCs) are becoming a high-growth technology in the area of electrical interconnects. This is due to their compact nature and high electrical-connection density over the traditional rigid printed circuit boards[168]. Comprising of a deformable substrate and conductive traces, FSCs possess an excellent deformation ability that will facilitate many new applications in the field of portable and wearable electronics, such as paper-like displays[169], smart clothing[170], stretchable solar cells[171], camera eyes[172] and biomedical sensors[173]. However, although the merits of FSCs are significant, there are some challenges that urgently need to be solved. One of the most critical points of this technology is the electro-mechanical reliability of the elastic interconnections, which are challenged in particular by relatively high and complex mechanical loading, such as, bending, compression and elongation[174].

Restricted by the demands of FSCs for high electro-mechanical performance, solutions to address the above problem are very challenging. Traditional strategies have been to use electroplated sinuous metallic wires deposited on deformable polymers, which had demonstrated high electrical conductivity under large tensile strains[175,176]. However, due to the lack of protection, the metallic wires usually suffer severe structural damage under repeated stretching/releasing cycles, which led to a poor reliability of FSCs and even complete failure. The recent development of patterning techniques has introduced alternative strategies for directly making FSCs patterns with a variety of highly conductive nanomaterials[177,178]. K. Kordás reported that elastic patterns of carbon nanotubes on a plastic film obtained a resistance of  $R_s = 4 \times 10^4 \Omega/\square$  (resistivity of  $4 \times 10^4 \Omega \cdot \mu\text{m}$ )[179]. J. Wu fabricated a graphene electrode with a peak electrical performance of  $R_s = 800 \Omega/\square$  (resistivity of  $5.6 \Omega \cdot \mu\text{m}$ )[180]. L. Hu achieved a minimum resistance of  $R_s = 50 \Omega/\square$  (resistivity of  $2 \times 10^2$



**Figure 3-34:** (a) Multi-functionalized CNT hybrid nanowires homogeneous dispersions in water, ethanol, acetone and tetrahydrofuran (THF) solvents. Due to the existence of hydrophilic APTES layer, the as-fabricated multi-functionalized CNT hybrid nanowires show good dispersability in various polar solvents with a concentration of 7mg/mL and form uniform suspension. (b) Time-resolved UV-Visible absorbance intensities of pristine CNTs and CNT hybrid nanowires ethanol dispersions at the wavelength of 500 nm. The two dispersions have the same concentration of 0.2 mg/mL and dispersed with ultrasonication before the test. The hybrid nanowire ethanol dispersion showed higher initial absorbance intensity than that of pure CNTs in ethanol, indicating a good dispersion quality of the hybrid nanowires. Moreover, the absorbance intensity of pure CNTs had a significant decrease after 1 h and disappeared after 1 week, representing the delamination of the dispersion. As a comparison, the hybrid nanowire dispersion showed relatively stable UV-Visible absorbance intensities during one week, which indicated the good stability of the hybrid nanowire dispersion. The inset images show the stability comparison of pristine CNTs and CNT hybrid nanowires ethanol dispersions (7 mg/mL) for one week.

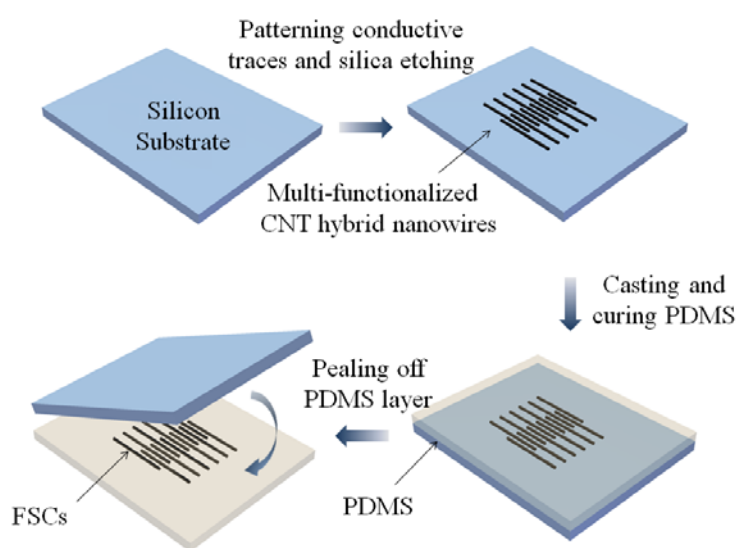


**Figure 3-35:** Schematic of the preparation of FSCs based on the hybrid nanowires and PDMS.

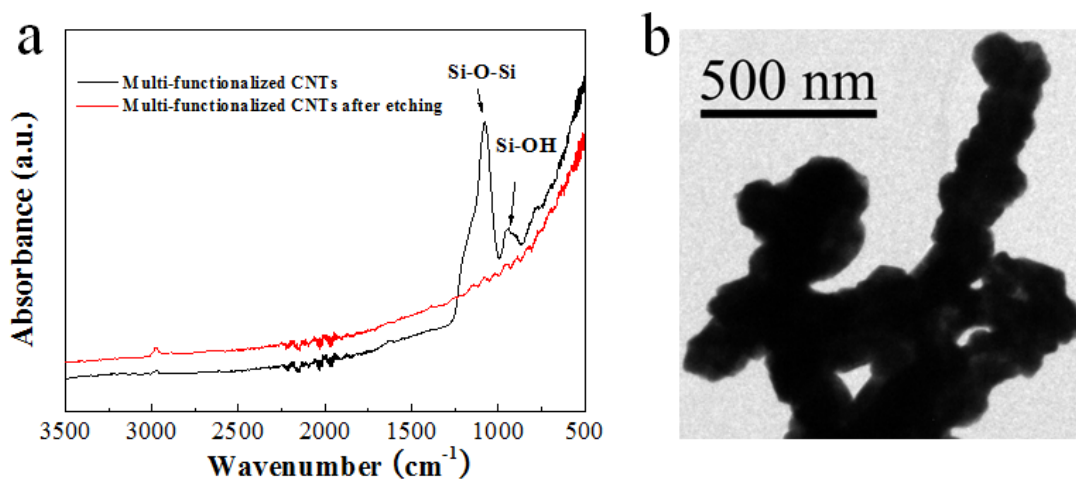


**Figure 3-36** (a) FTIR analysis of multi-functionalized CNT hybrid nanowires before and after HF etching. Two characteristic peaks at  $1000\text{ cm}^{-1}$  corresponding to Si-O-Si and Si-OH groups disappeared after HF etching of the multi-functionalized CNT hybrid nanowires, which identified the complete removal of silica layer, and also, no other characteristic peaks were found after HF etching indicates that the surface modification process and the HF etching process had no effect to the structure of CNTs. (b) TEM image of CNT based hybrid nanowires after HF etching. It can be seen that the hybrid nanowires still retain a complete silver nanoparticle coating layer after removing both the silica and APTES layer by HF etching.

$\Omega\cdot\mu\text{m}$ ) with a transparent and flexible silver nanowire based electrodes[181]. However, some challenges raised from the material themselves still limit their applications; carbon based nanomaterials, like pristine carbon nanotubes (CNTs) and graphene, can easily form agglomerations that are hard to disperse. This makes it difficult to form uniform patterns, and their relatively high contact resistance to metals might also lead to the poor electrical performance of FSCs. Metal nanowires lack flexibility and suffer structural damage at large strain that can cause the complete failure of FSCs. To satisfy the requirements for developing FSCs with stable electro-mechanical properties and high reliability, it is therefore desirable to synthesize hybrid nanomaterials that possess the high conductivity of metals together with good flexibility and dispersability.

Owing to the presence of abundant hydrophilic groups, such as Si-OH and  $-\text{NH}_2$ , the as-fabricated multi-functionalized CNT based hybrid nanowires were found to be easily dispersed in various polar solvents and form homogenous suspensions (Figure 3-34a). Ultra violet-Visible (UV-Vis) spectroscopy analysis further shows that the hybrid nanowire ethanol dispersions have good uniformity and stability (Figure 3-34b). These results made it possible to fabricate FSCs with uniform structures via direct patterning processes.

A mask patterning process was developed and utilized for FSCs fabrication, which is schematically illustrated in Figure 3-35. The prepared hybrid nanowire ethanol dispersion were filtrated and deposited onto silicon substrates through patterning of a shadow silicon mask. After removing the mask, the deposited structure on the substrate was then washed with a diluted hydrofluoric acid (HF) solution and dried in air to both completely remove all forms of silica (both APTES and silica layers) and restore the flexibility & conductivity of multi-functionalized CNT based hybrid nanowires.

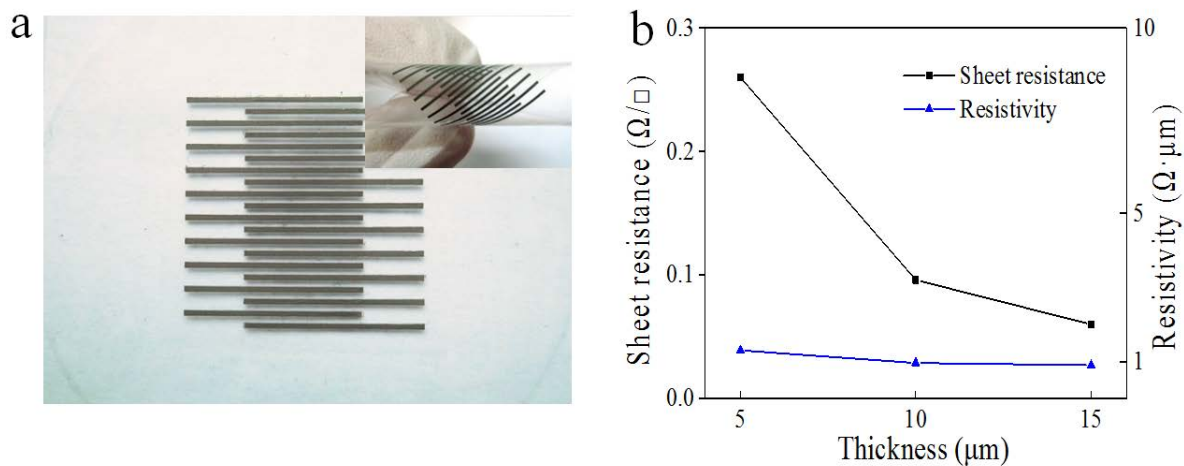


**Figure 3-37:** (a) FSCs with 10/10 lines, each line has a length of 1.5 cm and a width of  $500\mu\text{m}$ . The insets show the optical images of bent ( $180^\circ$ ). (b) Sheet resistance and resistivity change as a function of the hybrid nanowire conductive layer's thickness. The FSCs showed a stable initial resistivity value under a small variation of thicknesses (5  $\mu\text{m}$ ), indicating the good interconnection of individual hybrid nanowires at around 10  $\mu\text{m}$ .

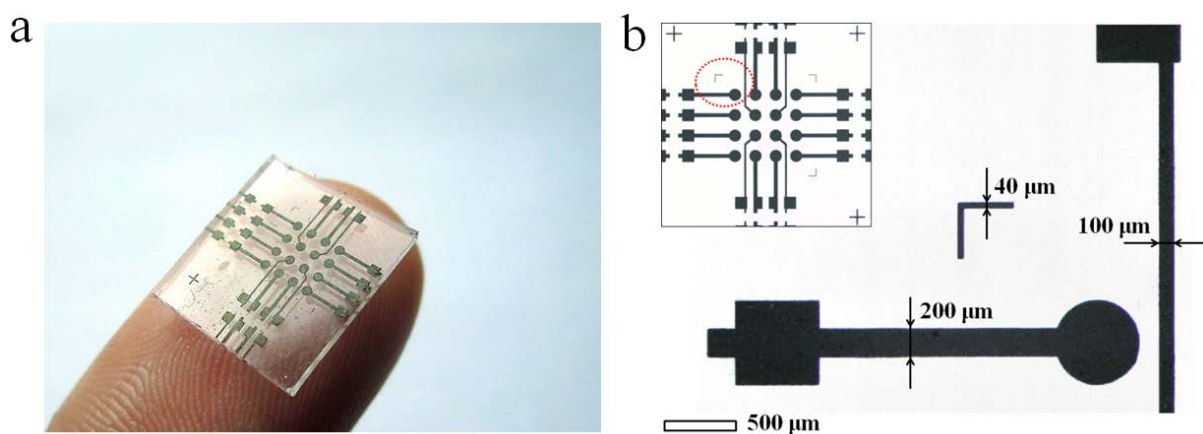


**Figure 3-38** (a-b) Optical image of FSCs ( $8 \times 8\text{mm}$ ) with a different pattern, which indicates the ability of multi-functionalized CNT hybrid nanowires for making arbitrary and fine patterns. Each unit of FSCs consists of line structures with varied widths, and the minimum width demonstrated in the unit is 40  $\mu\text{m}$ . The thickness of the pattern is about 10  $\mu\text{m}$ . Two-probe test of this smaller FSC shows the same resistivity result as the conductive traces with a diameter of 500  $\mu\text{m}$ , indicating the capability of the hybrid nanowires for making different patterns.

FTIR analysis were carried out for multi-functionalized CNT samples before and after HF etching, results were shown in Figure 3-36a. Two characteristic peaks at  $1000\text{ cm}^{-1}$  corresponding to Si-O-Si and Si-OH groups disappeared after HF etching of the multi-functionalized CNT based hybrid nanowires, which identified the complete removal of the silica layer. Moreover, no other characteristic peaks were found after HF etching indicates that the surface modification process and the HF etching process had no effect to the structure of CNTs. Figure 3-36b shows the TEM image of CNT based hybrid nanowires after HF etching. It has been found that the hybrid nanowires still retain a complete silver nanoparticle coating layer after removing both the silica and APTES layer by HF etching. PDMS was then cast onto the top of the silicon substrate and infiltrated through the gap in the patterned structures to provide mechanical support. After curing, the PDMS layer was peeled off from the substrate. The conductive traces were embedded below the PDMS surface to form conductive FSCs. Figure 3-37a shows parallel patterns of a 20-wire array with each wire having a length of 15 mm and a width of  $500\mu\text{m}$ . The effect of thickness variation to the resistivity change was also studied. As shown in Figure 3-37b, different conductive traces with different thicknesses ranging from  $5\mu\text{m}$  to  $15\mu\text{m}$  were fabricated, and their respective resistivity and sheet resistance were plotted by the four-probe method. The resistivity was found to be almost constant in this range, which indicates good interconnection of the individual hybrid nanowires. Therefore, the thickness of patterned conductive traces was regulated around  $10\mu\text{m}$  through controlling the volume of the solution to give stable electro-mechanical properties and ensuring the good reliability of the FSCs. In the following discussion, sheet resistance for  $10\mu\text{m}$  thick traces will be used as the main electrical performance indicator. The average thickness of PDMS substrate is  $500\mu\text{m}$ . The inset in Figure 3-37a shows FSCs at the bending state. It can be seen that the conductive line remains both continuous and uniform when rolled up till  $180^\circ$ , with no indication of breakage or voids. Figure 3-38a shows another example of FSCs with different patterns. Each unit of FSCs consists of line structures with varied widths, and the minimum width demonstrated in the unit is  $40\mu\text{m}$  (Figure 3-38b). It shows the potential ability of multi-functionalized CNT based hybrid nanowires for fine patterning.

### 3.3.4 Electro-mechanical properties and reliability of FSCs

The degree of silver nanoparticle coverage on CNT surfaces plays a crucial factor in the electrical performance of FSCs. To study this effect, different FSPC samples were prepared by using multi-functionalized CNT based hybrid nanowires with varied degrees of silver coverage ( $C_{\text{AgNO}_3} = 0 \sim 15\text{ g/L}$ ). The sheet resistance of each sample was tested by the four-probe method, and results were shown in Figure 3-39. It has been found that the sheet resistances of FSCs decrease rapidly with increasing silver nitrate concentrations, compared to the reference sample made from pure CNTs ( $1316\ \Omega/\square$ , resistivity of  $1.3 \times 10^4\ \Omega \cdot \mu\text{m}$ ). For samples prepared with silver nitrate concentrations of 1 g/L, 2 g/L, 5 g/L and 10 g/L, the sheet resistance values are  $100.81\ \Omega/\square$ ,  $4.07\ \Omega/\square$ ,  $0.38\ \Omega/\square$  and  $0.15\ \Omega/\square$  respectively and the percolation threshold for an exponential decrease in resistance was located at 2g/L. It indicates that silver nanoparticles at the CNT surface were interconnecting and provide the main contribution to electrical conductivity when the silver nitrate concentration reached 2

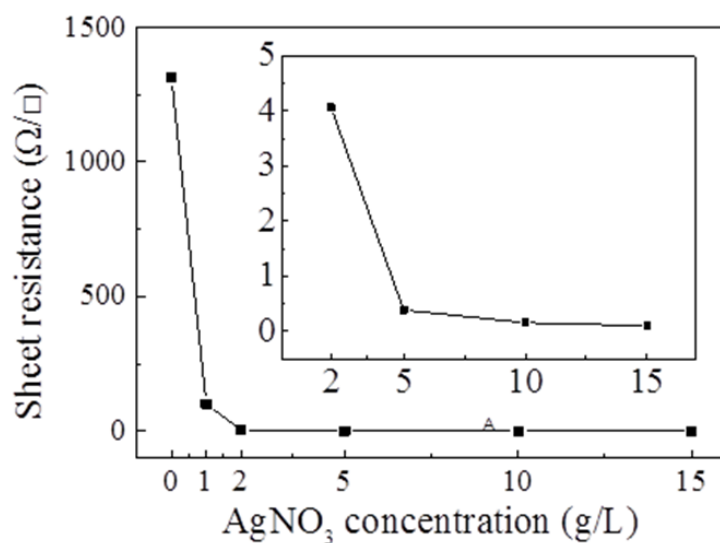


**Figure 3-39** Electrical tests show a decrease of sheet resistance with the increase of silver nanoparticles coverage on CNT. A minimum resistance of  $0.096 \Omega/\square$  (equivalent resistivity of  $0.96 \Omega \cdot \mu\text{m}$ ) at 0% strain was obtained when CNT was totally covered by silver.

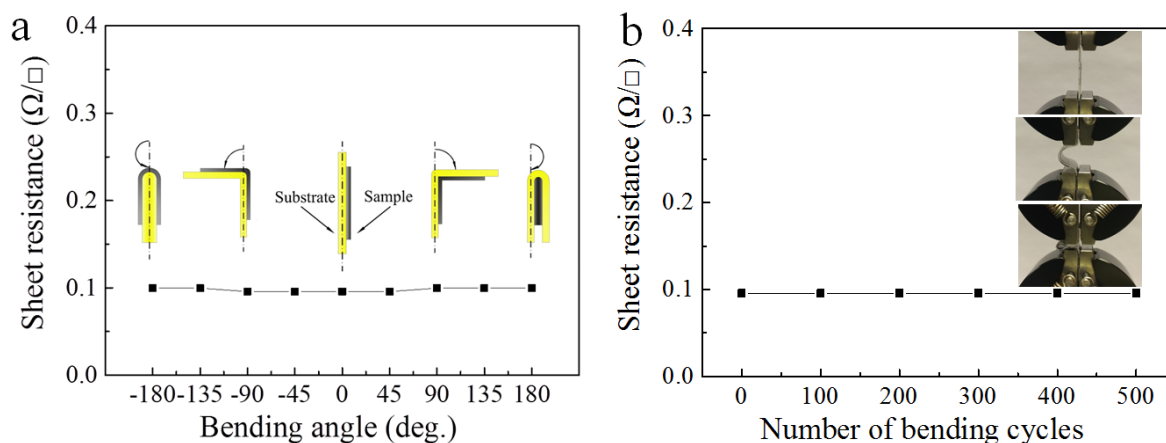


**Figure 3-40:** (a) The sheet resistance change of FSCs ( $C_{\text{AgNO}_3}=15\text{g/L}$ ) as a function of bending angle. A small variation of sheet resistance less than 3.8% was observed when FSCs were bent up to  $180^\circ$ , which indicated the stable electro-mechanical properties of FSCs. (b) Resistance results of FSCs upon bending cycles. FSCs demonstrate a high reliability after 500 cycles of bending/releasing.

g/L. The minimum sheet resistance ( $0.096 \Omega/\square$ , resistivity of  $0.96 \Omega \cdot \mu\text{m}$ ) was reached when CNTs were fully covered with silver nanoparticles ( $C_{\text{AgNO}_3} = 15 \text{ g/L}$ ), which means that a complete silver nanoparticle coating layer can minimize the contact resistance and provide sufficient conductive channels inside the conductive traces. These results are consistent with the morphology change of multi-functionalized CNT based hybrid nanowires as observed in Figure 3-32b-f. Moreover, high temperature annealing can further decrease the sheet resistance of the conductive traces due to the sintering of silver nanoparticles. However, a rigid silver shell can hinder the flexibility of the hybrid nanowires, which would lead to a poor electro-mechanical performance under large structural deformation.

### 3.3.5 Flexibility and reliability of FSCs

The bending effect on the sheet resistance of FSCs comprising of multi-functionalized CNT based hybrid nanowires ( $C_{\text{AgNO}_3} = 15 \text{ g/L}$ ) was investigated further on a high precision load/displacement measurement machine with a strain rate of  $5 \text{ mm/s}$ . Figure 3-40a shows the sheet resistance variation of FSCs as a function of bending angles ( $-180^\circ \sim 180^\circ$ ). Notably, a small variation of resistance less than 3.8% was observed when the sample was bent up to  $180^\circ$ , and it recovered after straightening. Notably, after 500 cycles for a bending angle of  $180^\circ$ , the electrical resistance remained constant, as shown in Figure 3-40b. These results show the excellent electro-mechanical stability of hybrid nanowires during bending tests compared with conventional materials used in flexible electronics, even graphene which shows a resistance increase of 20% after the third bending cycle due to the crack formation[182].

The microstructural analysis of the FSCs further helps to understand the reasons for their

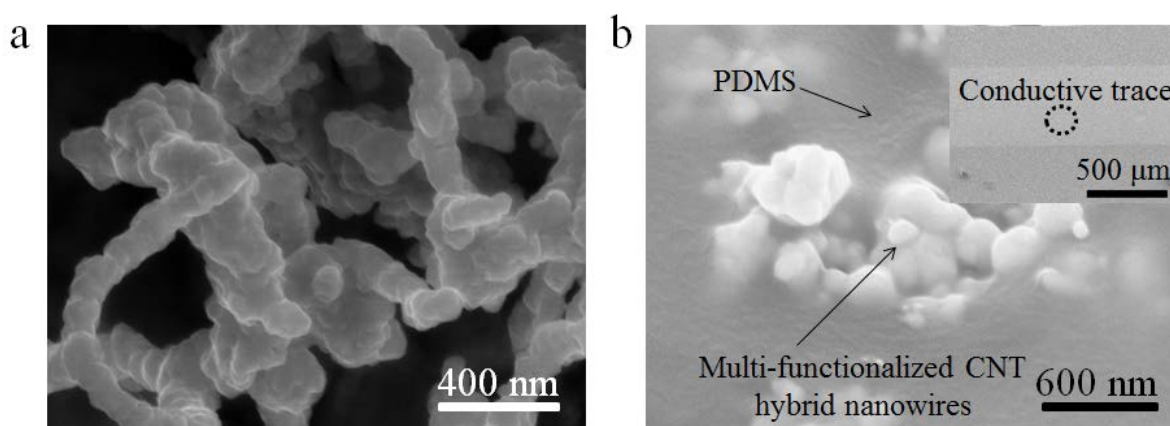


**Figure 3-41** (a) SEM image of the hybrid nanowires after patterning. The hybrid nanowires were entangled with each other to form a conductive network. (b) SEM images of FSCs after PDMS infiltration. The multi-functionalized CNT hybrid nanowires are protected by PDMS through embedding into the PDMS layer. Due to the penetration of PDMS into the conductive traces, the internal space inside the conductive traces was fully occupied by PDMS which could provide as mechanical support for individual hybrid nanowire during large structure deformation. It would make the FSCs to be more reliable than the ordinary plated metal traces on PDMS substrate. The inset image shows the image of FSCs. The average diameter of each conductive trace is  $500 \mu\text{m}$ .

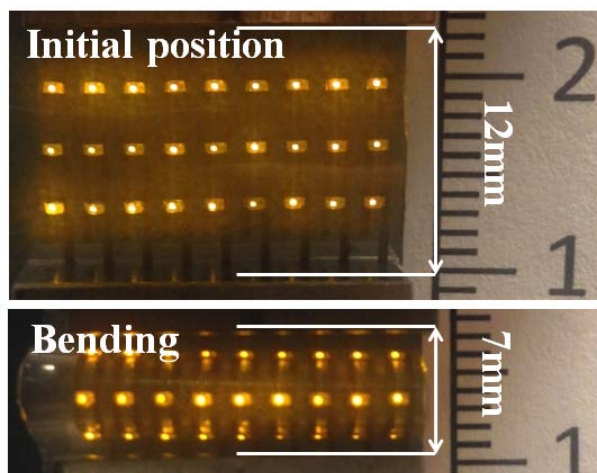


**Figure 3-42:** Optical images of LED array integrated at FSCs with and without bending. LEDs remained lit with the same illumination intensity as at 0% strain when the demonstrator was bent to 180°. It indicates the stable electrical performance of the FSCs.

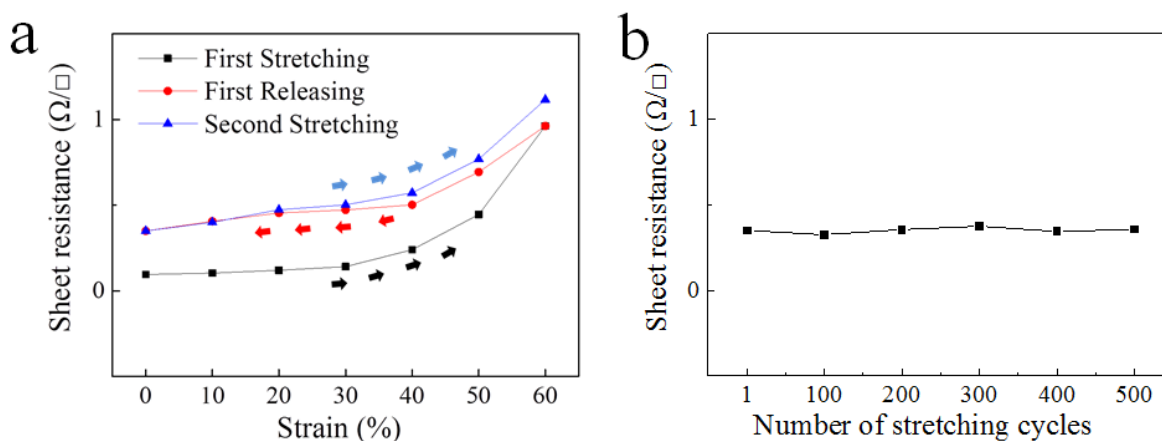


**Figure 3-43** (a) Resistance change of FSCs ( $\text{CAgNO}_3=15\text{g/L}$ ) as a function of applied strains. The resistance remained stable ( $\sim 0.1 \Omega/\square$ ) under 30% stretching. Further increasing the tensile strain to 60%, the resistance showed an increase from  $0.1 \Omega/\square$  to  $0.96 \Omega/\square$ . Upon the release of the strain, the sheet resistance was partially recovered and stabilized at  $0.35 \Omega/\square$  with 0% strain. (b) Reliability of FSCs under repeated stretching/releasing cycles. After the first stretching/releasing cycle, FSCs showed a stable sheet resistance ( $0.35 \Omega/\square$  at 0% strain) with less than 8% variation after 500 repeated cycles.

outstanding electrical performance. As shown in Figure 3-41a, the hybrid nanowires entangled with each other to form a conductive network after patterning and acted as the main electron pathways for FSCs. Figure 3-41b shows the surface morphology of FSCs after PDMS infiltration. It can be seen that PDMS has penetrated through the conductive layer and filled all along the inside gaps of the conductive network. The complete filling of PDMS provides enough mechanical support for absorbing stresses and protecting the multi-functionalized CNT based hybrid nanowires from structural damages under large deformation.

To demonstrate the electrical resistance change of FSCs during bending, an array of LEDs was assembled on the top of the parallel wires and sealed with PDMS layer. Figure 3-42 shows the lit image of LEDs before and during bending. It was found that LED demonstrators showed the same illumination intensity at the bending state as the initial state, which indicates the stable electrical performance of FSCs. This result was also consistent with the bending test (Figure 3-40a).

### 3.3.6 Stretchability and reliability of FSCs

The electrical performance of FSCs ( $C_{\text{AgNO}_3} = 15 \text{ g/L}$ ) was also investigated as a function of tensile strain on the high precision load/displacement measurement machine at the same strain rate of 5 mm/s. Figure 3-43a shows the results at a maximum strain of 60%. During the first stretching/releasing cycle, the resistance remained stable ( $\sim 0.1 \text{ } \Omega/\square$ ) under 30% stretching. Further increasing the tensile strain to 60%, the resistance showed an obvious increase from  $0.1 \text{ } \Omega/\square$  to  $0.96 \text{ } \Omega/\square$ . Upon the release of the strain, the sheet resistance was partially recovered and stabilized at  $0.35 \text{ } \Omega/\square$  with 0% strain. After the first cycle of stretching/releasing, the electrical resistance was restored to a stable value, with a resistance increase of  $\sim 30\%$  under 30% stretching. The stable electrical performance under 30% of strain indicates that it can be intrinsically attributed to the reserved elongation of the hybrid nanowires due to their flexible and curved structures (Figure 3-41a). Moreover, the obvious resistance increase could be caused when strain ratio exceeded 60% due to the partially breaking or cracking of the silver nanoparticle layer on CNT's surface, which can possibly lead to an electrical breakdown. Mechanical breakage of FSCs took place when PDMS was stretched beyond the maximum elongation ratio of 100%. Additional stretch/release cycles in the range of 0-60% were performed to evaluate the reliability of FSCs. For up to 500 repeated stretching cycles, FSCs showed relatively stable sheet resistance ( $0.35 \text{ } \Omega/\square$  at the strain of 0%) with a small variation of less than 8% (Figure 3-43b), with no observed indication of failure. These results demonstrate good reliability and stable electro-mechanical properties of the hybrid nanowire based FSCs when compared to other reported CNT and silver nanowire composites[183–185]. For example, many of single-walled carbon nanotube (SWCNT) flexible composites showed order-of-magnitude higher initial resistivity and significant increase of resistance after the first stretching cycle due to the large contact resistivity of individual CNTs[183,184]. Furthermore, the stretchable electrode based on a silver nanowire-polymer composite presented a poor electro-mechanical stability for stretching (1000 times increase of resistivity at the strain of 80%) and low reliability under strain cycles (3 times increase of resistivity at the first 500 cycles with a strain of 30%) due to the

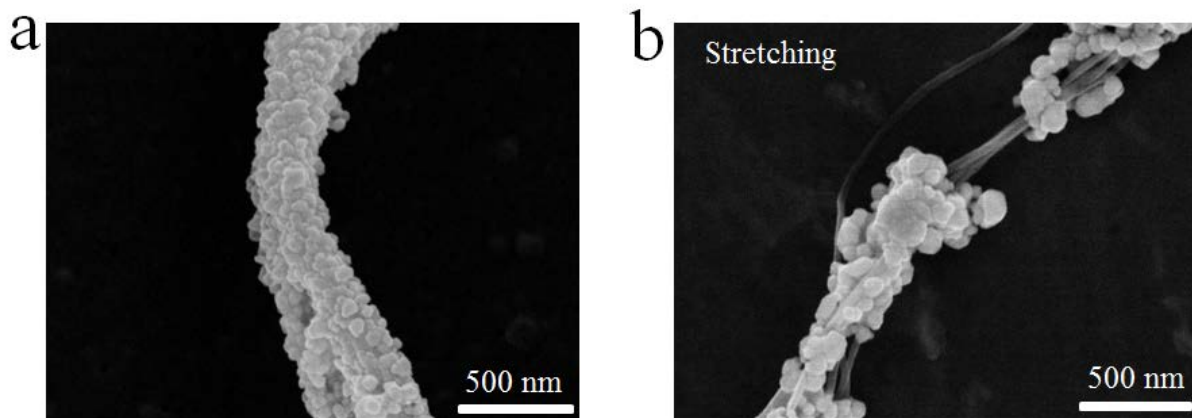


**Figure 3-44:** (a) SEM images of the multi-functionalized CNT based hybrid nanowire after HF etching. The hybrid nanowire still holds a complete silver-nanoparticle layer even though some defects were identified. (b) When a small tensile strain (<30%) was applied, the original bent hybrid nanowires was firstly straighten towards the direction of strain, which showed stable electro-mechanical properties of FSCs within 30% strain. With the strain ratio further increasing till 60%, the silver-nanoparticles layer was broken to short pieces, and they had a shift along the axis of CNTs towards the direction of stretching. The interspaces between each piece prevent further structural damage. Moreover, it can be seen that CNT bundles have a close connection with each silver piece after removing APTES and silica layers and act as bridges to provide more pathways for electron transmission.

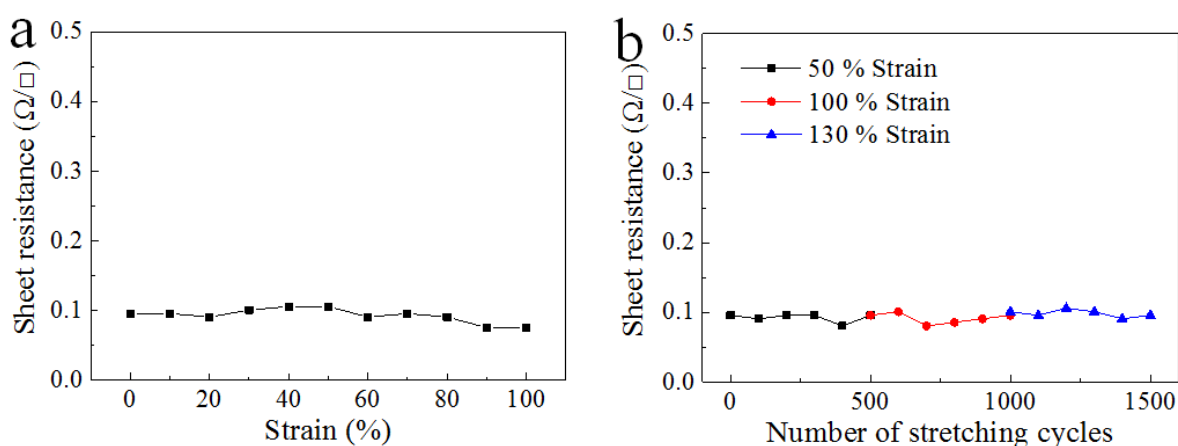


**Figure 3-45:** (a) Resistance change of FSCs on the pre-stretched silicon rubber substrate as a function of applied strain. FSCs showed a highly stable sheet resistance ( $\sim 0.1 \Omega/\square$ ) with a small variation of 7% under 100% stretching. Such stable electro-mechanical properties are attributed to the flexibility of the hybrid nanowires. (b) Resistance results of FSCs on the pre-stretched silicon rubber substrate under repeated stretch and release cycles. During the first 500 cycles, the FSCs were stretched with 50% strain and showed a constant resistance ( $R/R_0 \approx 1$  at 0% strain), and for the second 500 cycles, FSCs were stretched to an increased strain ratio of 100% and also showed a stable resistance ( $R/R_0 \approx 1$  at 0% strain). At the last 500 cycles, FSCs were stretched with a further increased strain of 130%. The resistance still remained stable with a slight increase of 10% ( $R/R_0 = 1.1$  at 0% strain).

detachment of the nanowire contacts and crack formation during stretching[185].

In order to understand the electrical conduction mechanism of FSCs, morphology analysis of the multi-functionalized CNT based hybrid nanowires before and under stretching was performed by scanning electron microscopy (SEM), with the results shown in Figure 3-44a-b. It can be seen that the multi-functionalized CNT based hybrid nanowires still retain a complete silver nanoparticle coating layer after removing both the silica and APTES layer by HF etching. Subsequently when the FSCs were stretched, the original bent hybrid nanowires were straightened towards the direction of the tensile strain. The bent structure of the hybridnanowires helps to maintain a stable electrical resistance of FSCs within a tensile strain of 30%. With further increase of the tensile strain, the original silver nanoparticles layer was broken into short pieces that had moved along the axis of CNTs towards the direction of tensile strain. The breakage of the silver nanoparticle coating layer led to the increase of resistance beyond a strain ratio of 30%. However, more stretch/release cycles did not cause a complete failure or any further resistance increase in the FSCs. It has been found that these short pieces were still attached to the surface of CNTs after stretching, instead of forming individual nanoparticles. Under large strains, the interspaces between each piece had enough room for their movement, preventing further structural damage. Moreover, the network of CNTs still acted like bridges to connect each piece and provide more pathways for electron transmission. This also partially helped to maintain a low resistance of FSCs at larger strains.

### **3.3.7 Improved stretchability and reliability of FSCs**

To further improve the electrical stability as well as the stretchability, FSCs were transferred onto a pre-stretched PDMS substrate with a tensile strain of 100%. The sheet resistance of the sample was evaluated and shown in Figure 3-45a. It has been found that FSCs showed a stable sheet resistance ( $\sim 0.1 \Omega/\square$ ) with a small variation of 7% under 100% stretching. This result represents a three-fold of improvement in the electro-mechanical properties of FSCs compared to the previous case when the non-pre-stretched FSPC was strained to 30%. Such stable electro-mechanical performance of FSCs is attributed to the highly flexible structure of the hybrid nanowires and protection of PDMS. Further increase of the pre-strain ratio of the PDMS substrate could result in an even more stable electrical performance and improved stretchability. Moreover, the maximum strain was increased to 800% before causing mechanical breakdown of pre-stretched FSCs due to the use of even softer PDMS (ELASTOSIL®RT 4600A/B).

The electrical reliability test was also carried out on the high precision load/displacement measurement machine with a strain rate of 5 mm/s to evaluate the reliability of FSCs on the pre-stretched silicon rubber substrate, with the results shown in Figure 3-45b. During the first 500 cycles, the FSCs were stretched with 50% strain and showed a constant resistance ( $R/R_0 \approx 1$  at 0% strain), and for the second 500 cycles, FSCs were stretched to an increased strain ratio of 100% and also showed a stable resistance ( $R/R_0 \approx 1$  at 0% strain). At the last 500 cycles, FSCs were stretched with a further increased strain of 130%. The resistance still remained stable with a slight increase of 10% ( $R/R_0 = 1.1$  at 0% strain). Such stable electrical performance of the FSCs is attributed to the intrinsic flexibility of the multi-functionalized CNT based hybrid nanowires and the sufficient protection from the PDMS layer. These

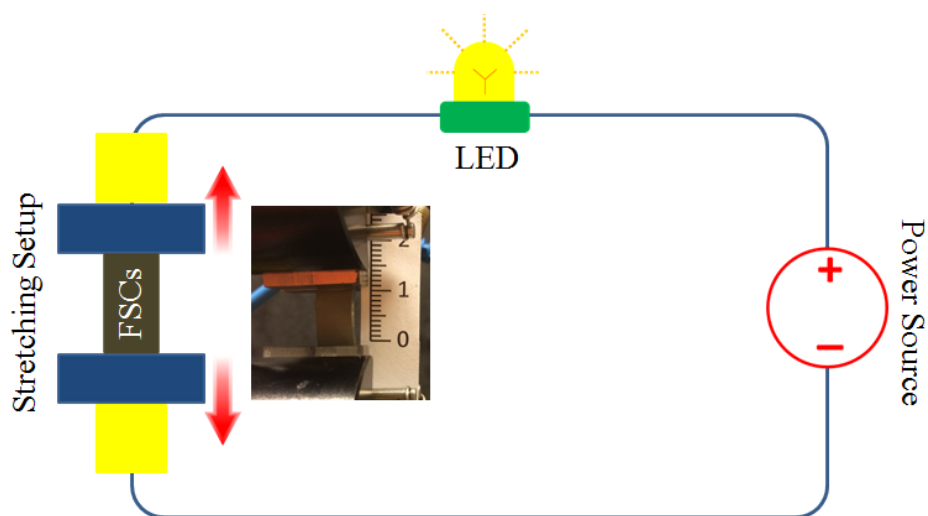


**Figure 3-46:** Schematic drawing of the LED circuit for the stretching demonstration. FSCs were fixed between two clamps of the stretching setup and connected with a commercial power source and LED. The working voltage of the LED is 2V.

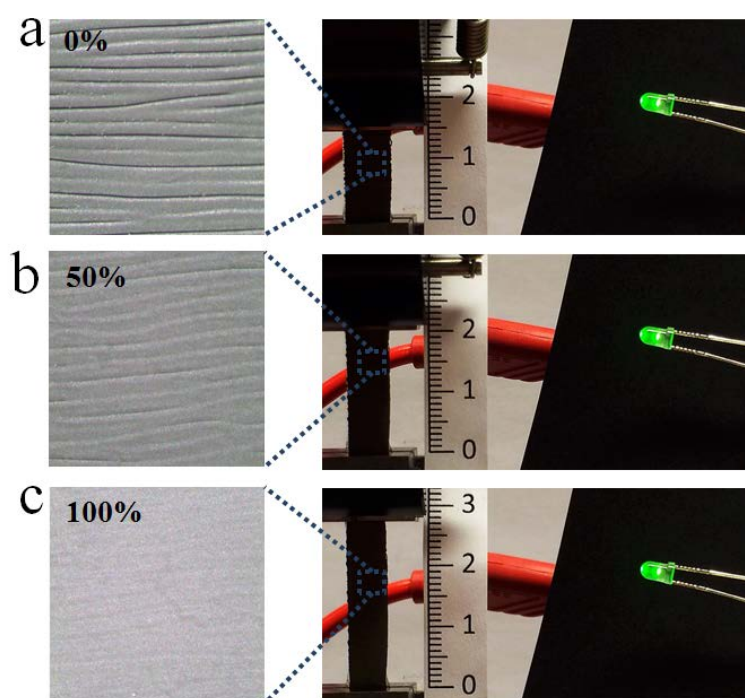


**Figure 3-47:** (a-b) LED demonstrator and surface morphology change of FSCs under stretching (see video S1). Compared to the initial light state (strain = 0%), the LED demonstrator remained the same illumination intensity under different stretching ratios (50% and 100%). The optical image of the conductor surface showed that some wrinkles appear against the direction of stretching at the initial state and disappear as the strain decreased. The good reliability of the FSCs on the pre-stretched substrate was attributed to the excellent flexibility of hybrid nanowires and the sufficient protection from PDM

results indicate the stable and superior electro-mechanical properties of FSCs under larger stretching ratios compared to other reports on elastic conductors in literature[72][184–193]. For example, electronic whiskers based on patterned carbon nanotube and silver nanoparticle show a three times increase in resistance at a small strain of 2.4% due to the increase of distance between individual silver nanoparticles[186]. Pre-stretched PDMS substrate with copper coating suffer poor reliability caused by cracks formation during repeated stretching/releasing cycles[176]. Stretchable conductors comprising of silver nanowires suffer an irreversible increase of resistance after the first stretch/release cycle due to the rigid structure of silver nanowires, and they also show poor electro-mechanical performance and low electrical stability[185,187]. Many metal/polymer composite films exhibit lower reliability than the hybrid nanowire based FSCs[188–190]. A variety of reported FSCs comprising of CNTs and elastic polymers show resistance that are orders of magnitude higher than that of multi-functionalized CNT based hybrid nanowires based FSCs[184,191–193].

A LED demonstrator was built to illustrate the resistance change of the FSCs on a pre-stretched PDMS substrate, which was stretched at different strain ratios with the assist of high precision load/displacement measurement machine. Figure 3-46 shows the schematic of the circuit of the LED demonstrator comprising of the conductive trace fixed between two clamps of the load/displacement machine, an LED and power source. The conductive trace was cyclically stretched with a strain rate of 5mm/s. The working voltage of the LED is 2V.

The lit images and the surface morphology of the conductive trace are shown in Figure 3-47a-b. Compared to the initial light state (strain = 0%), the LED remained the same brightness under different strain ratios (50% and 100%). Due to the prestretched PDMS substrate, the surface of conductor showed some wrinkles running opposite to the direction of stretching in the initial state (0% strain) and these started to disappear as the percentage strain was increased. Those wrinkles would raise challenges to the direct connection between conductive wires and functional devices. Therefore, it is essential to combine both non-prestretched and prestretched FSCs for meeting various requirements of real applications. The sufficient protection from the PDMS layer prevented the conductive layer from getting any structural damage.



# Chapter 4

## Conclusions and Outlook

The thesis focuses on developing flexible and scalable chemical approaches to functionalize CNMs for different applications, ranging from electronics to composite and biomedicine. According to the bonding difference between CNMs and the functional components, the functionalization methods can be divided into two groups, which are covalent functionalization and non-covalent functionalization.

Covalent functionalization of the CNM's surface is based on reactions with the oxygen-containing groups bonded directly to the  $\pi$ -conjugated skeleton of the CNMs. The first part in this chapter introduced an efficient surface activation process using simultaneous oxidation and ultrasonication to activate the CNT surface. It shows much higher activation efficiency than the traditional acid etching processes. Self-assembly of silver nanoparticles on CNT surface were achieved in a complex silver coating solution where a stable silver nanoparticle deposition speed was maintained due to the sustained ion release property of metal-ion chelates. As a result, finely grained and uniform silver nanoparticles were successfully deposited on the surface of activated CNTs. The developed silver/CNT composites show strong antibacterial property to E.coli bacteria. The second part of the chapter presents covalent functionalization of graphene oxide for cement reinforcement. The key benefit of FGO lies in its ability to form covalent bonds with C-S-H whilst having minimum effect on the workability of mortar paste. The reinforcement of FGO leads to significant mechanical strength improvement. With up to 40% increased cement early and ultimate strength due to the incorporation of FGO, Fast demolding and manufacture of lighter, slimmer constructions become highly possible, which give major competitive advantages in many applications when the commodity demand is lower and expensive transport costs are kept down. The decreased consumption of cement would also result in a reduction of CO<sub>2</sub> emissions. The third part of the chapter focuses on covalent functionalization of graphene based films that act as heat spreaders for hotspot cooling. The covalent bonding between GBF and the substrate is realized via the linkage of a silane coupling agent which can significantly reduce the thermal interface resistance and improve the cooling effect. Such results show great potential in the thermal management of high-power density devices.

Non-covalent functionalization utilizes various functional molecules or active species as assembly mediators to functionalize the surface of CNMs via non-covalent interactions, such as hydrophobic,  $\pi$ - $\pi$  stacking, van der Waals' force and wrapping interaction. The first part in this chapter presents a method of non-covalent self-assembly of high-thermal-conductivity of graphene films. The fabrication of the graphene film is based on phase change of graphene oxide sheets from random dispersion to liquid crystal in aqueous solution, and followed by graphitization and pressing. It yields smooth, large-grain and turbostratic-stacking GFs with an in-plane thermal conductivity over 3200 W/mK, which is superior to currently existing thermally conductive pyrolytic graphite sheets by over 60%. The fabricated GFs also have

excellent flexibility and mechanical tensile strength. It thus opens for addressing major heat dissipation issues in current form-factor driven electronics and other high power driven systems. The second part of this chapter introduced the non-covalent functionalization of graphene for high thermal conductive adhesive. Liquid exfoliated few-layer graphene was utilized as fillers to improve the thermal conductivity of the thermal conductive adhesive. To overcome the Van der Waals' force between graphene layers, proper solvents with similar surface tensile as graphene were selected as the exfoliation solvents, which demonstrated excellent exfoliation efficiency and solution stability. Thermal conductivity of thermal conductive adhesive with 3% of graphene was increased about four times than the reference sample, which demonstrated superior heat dissipation properties. The viscosity of the paste was regulated in an acceptable range by decreasing the interaction of nanofillers and polymer binder molecules. The third part of this chapter presents a non-covalent functionalization process for synthesizing intrinsically flexible multi-functionalized CNT based hybrid nanowires. The multi-functionalized CNT based hybrid nanowires were synthesized with different functional materials on the surface of CNTs to produce a metal nanoparticle coating layer and form uniform dispersions whilst possessing the CNT's original structural integrity and high flexibility. The synthesized multi-functionalized CNT based hybrid nanowires possess many excellent properties, such as good dispersability and stability in various polar solvents, large flexibility and high electrical conductivity. These extraordinary properties facilitate the application of hybrid nanowires in the fabrication of flexible and stretchable circuits with high resolution, which show good flexibility and stable electrical performance under different structural deformation.

Future work will be focused on improving the current functionalization processes of CNMs for diverse applications. For example, the surface activation processes presented in the thesis may bring adverse effects to CNT's structure and properties, such as decreased aspect ratio, poor mechanical strength and low electrical conductivity. To minimize such effects, the oxidation degree of CNTs needs to be regulated through controlling the activation time and temperature. The fabricated metal coated CNT hybrids have the advantages of light weight and low costs, which can be used for replacing the traditional pure metal fillers in the conductive adhesive. To meet the requirement of the adhesive for high electrical and thermal conductivity, the metal coverage ratio on the surface of CNTs needs to be improved till to form complete metal shells. The second part of future work is to study size effect of GO to the cement reinforcement, and also focus on different types of cement applications, such as self-compacting concrete. The third part of future work is to improve the functionalization of GBFs. The original APTES functionalization process requires the usage of GO to build covalent bonds with the silica substrate. However, it is well-known that GO is a poor media for phonon transfer due to the effect of oxygen. Therefore, new functional agents need to be explored to replace APTES and GO to improve the heat dissipating performance of GBFs. We will setup production lines for large scale fabrication of GFs, Finally, the developed multi-functionalized CNT based hybrid nanowires have demonstrated good flexibility and high electrical conductivity. More applications using the hybrid nanowires will be investigated, such as electrodes, sensors, catalysts, thermal management and biomedical materials.

# Acknowledgements

I would like to thank my supervisor and examiner Prof. Johan Liu for giving me the opportunity to work in such a challenging and exciting research area, and particularly, for his continuous support and advices. Special thanks give to my co-supervisors Prof. Luping Tang and Dr. Lilei Ye for their valuable inspiring scientific discussions during whole of my various projects.

Also, I want to express my thanks to Dr. Björn Carlberg and Dr. Carl Zandén for giving me help on managing the chemistry laboratory and many advices at the beginning of my research life. I also want to thank Dr Si Chen for his precious knowledge on packaging materials and machine support.

I would like to thank Dr. Di Jiang, Dr. Majid Kabiri Samani and Peng Su for their support and collaboration on our research topics as well as our friendship. I also want to express my thanks to Dr. Hu Li and Prof Klaus Leifer from Uppsala University, Dr. Santosh Pandit from Chalmers, Dr. Shuping Wang from Chalmers, Dr. Volodymyr Kuzmenko from Chalmers, Shirong Huang and Guangjie Yuan from Shanghai University, Prof Jie Chen and Prof Xiangfan Xu from Tongji University, and Prof Baowen Li from University of Colorado for their sincere help and collaboration in variety projects I am involved.

Also I would like to thank to all my former and present colleagues at the Electronics Materials and Systems Laboratory: Carl Zandén, Wei Mu, Michel Edwards, Yong Zhang, Shuangxi Sun, Yifeng Fu, Changhong Zhao, Murali Murugesan, Ning Wang, Nikolaos Logothetis, Zhili Hu, Xin Luo, Qi Li, Andreas Nylander, Josef Hansson, Yuqing Shi, and many others for their friendship, support, discussion and collaboration.

Many thanks are given to Svante Pålsson, Christer Andersson, Kaija Matikainen, and Göran Petersson who work at the Nanofabrication Laboratory in MC2 for their invaluable support on chemical order, laboratory safety and instrument maintenance.

Last but not least, I would like to thank my family for their unconditional love and encouragement throughout my research.



# Bibliography

- [1] N. Ferrer-Anglada, V. Gomis, Z. El-Hachemi, U.D. Weglikovska, M. Kaempgen, S. Roth, Carbon nanotube based composites for electronic applications: CNT–conducting polymers, CNT–Cu, *Phys. Status Solidi A*. 203 (2006) 1082–1087. doi:10.1002/pssa.200566188.
- [2] L. Aryasomayajula, K.-J. Wolter, Carbon Nanotube Composites for Electronic Packaging Applications: A Review, *J. Nanotechnol.* 2013 (2013) e296517. doi:10.1155/2013/296517.
- [3] K. Zhang, M.M.F. Yuen, N. Wang, J.Y. Miao, D.G.W. Xiao, H.B. Fan, Thermal interface material with aligned CNT and its application in HB-LED packaging, in: *Electron. Compon. Technol. Conf. 2006 Proc. 56th*, 2006: p. 6 pp.-. doi:10.1109/ECTC.2006.1645644.
- [4] Z. Gao, Y. Zhang, Y. Fu, M. Yuen, J. Liu, Graphene heat spreader for thermal management of hot spots in electronic packaging, in: *2012 18th Int. Workshop Therm. Investig. ICs Syst. THERMINIC*, 2012: pp. 1–4.
- [5] K.M.F. Shahil, A.A. Balandin, Thermal properties of graphene and multilayer graphene: Applications in thermal interface materials, *Solid State Commun.* 152 (2012) 1331–1340. doi:10.1016/j.ssc.2012.04.034.
- [6] L. Dai, Functionalization of Graphene for Efficient Energy Conversion and Storage, *Acc. Chem. Res.* 46 (2013) 31–42. doi:10.1021/ar300122m.
- [7] J. Hou, Y. Shao, M.W. Ellis, R.B. Moore, B. Yi, Graphene-based electrochemical energy conversion and storage: fuel cells, supercapacitors and lithium ion batteries, *Phys. Chem. Chem. Phys.* 13 (2011) 15384. doi:10.1039/c1cp21915d.
- [8] H.-J. Choi, S.-M. Jung, J.-M. Seo, D.W. Chang, L. Dai, J.-B. Baek, Graphene for energy conversion and storage in fuel cells and supercapacitors, *Nano Energy.* 1 (2012) 534–551. doi:10.1016/j.nanoen.2012.05.001.
- [9] L. Yin, Y. Wang, G. Pang, Y. Koltypin, A. Gedanken, Sonochemical Synthesis of Cerium Oxide Nanoparticles—Effect of Additives and Quantum Size Effect, *J. Colloid Interface Sci.* 246 (2002) 78–84. doi:10.1006/jcis.2001.8047.
- [10] S. Qiu, Z. Zhou, J. Dong, G. Chen, Preparation of Ni Nanoparticles and Evaluation of Their Tribological Performance as Potential Additives in Oils, *J. Tribol.* 123 (1999) 441–443. doi:10.1115/1.1286152.
- [11] Z. Liu, X.Y. Ling, X. Su, J.Y. Lee, Carbon-Supported Pt and PtRu Nanoparticles as Catalysts for a Direct Methanol Fuel Cell, *J. Phys. Chem. B.* 108 (2004) 8234–8240. doi:10.1021/jp049422b.
- [12] J. Wang, M. Musameh, Carbon nanotube screen-printed electrochemical sensors, *The Analyst.* 129 (2004) 1. doi:10.1039/b313431h.
- [13] J.T. Robinson, F.K. Perkins, E.S. Snow, Z. Wei, P.E. Sheehan, Reduced Graphene Oxide Molecular Sensors, *Nano Lett.* 8 (2008) 3137–3140. doi:10.1021/nl8013007.
- [14] X. Sun, Z. Liu, K. Welsher, J.T. Robinson, A. Goodwin, S. Zaric, H. Dai, Nano-graphene oxide for cellular imaging and drug delivery, *Nano Res.* 1 (2008) 203–212. doi:10.1007/s12274-008-8021-8.

- [15] Z. Liu, S. Tabakman, K. Welsher, H. Dai, Carbon nanotubes in biology and medicine: In vitro and in vivo detection, imaging and drug delivery, *Nano Res.* 2 (2010) 85–120. doi:10.1007/s12274-009-9009-8.
- [16] F. Chen, Z.-C. Wang, C.-J. Lin, Preparation and characterization of nano-sized hydroxyapatite particles and hydroxyapatite/chitosan nano-composite for use in biomedical materials, *Mater. Lett.* 57 (2002) 858–861. doi:10.1016/S0167-577X(02)00885-6.
- [17] P. Gatenholm, D. Klemm, Bacterial Nanocellulose as a Renewable Material for Biomedical Applications, *MRS Bull.* 35 (2010) 208–213. doi:10.1557/mrs2010.653.
- [18] J. Weiss, P. Takhistov, D.J. McClements, Functional Materials in Food Nanotechnology, *J. Food Sci.* 71 (2006) R107–R116. doi:10.1111/j.1750-3841.2006.00195.x.
- [19] H.J. Fecht, K. Brühne, *Carbon-based Nanomaterials and Hybrids: Synthesis, Properties, and Commercial Applications*, CRC Press, 2014.
- [20] K. Ariga, M. Li, G.J. Richards, J.P. Hill, Nanoarchitectonics: A Conceptual Paradigm for Design and Synthesis of Dimension-Controlled Functional Nanomaterials, *J. Nanosci. Nanotechnol.* 11 (2011) 1–13. doi:10.1166/jnn.2011.3839.
- [21] Y. Zhao, J. Liu, Y. Hu, H. Cheng, C. Hu, C. Jiang, L. Jiang, A. Cao, L. Qu, Highly Compression-Tolerant Supercapacitor Based on Polypyrrole-mediated Graphene Foam Electrodes, *Adv. Mater.* 25 (2013) 591–595. doi:10.1002/adma.201203578.
- [22] Y. Hu, O.A. Shenderova, Z. Hu, C.W. Padgett, D.W. Brenner, Carbon nanostructures for advanced composites, *Rep. Prog. Phys.* 69 (2006) 1847. doi:10.1088/0034-4885/69/6/R05.
- [23] V.S. Vavilov, The properties of natural and synthetic diamond, *Phys.-Uspekhi.* 36 (1993) 1083. doi:10.1070/PU1993v036n11ABEH002207.
- [24] N. Park, J. Ihm, Electronic structure and mechanical stability of the graphitic honeycomb lattice, *Phys. Rev. B.* 62 (2000) 7614–7618. doi:10.1103/PhysRevB.62.7614.
- [25] W.J. Bartz, Solid lubricant additives—effect of concentration and other additives on anti-wear performance, *Wear.* 17 (1971) 421–432. doi:10.1016/0043-1648(71)90048-2.
- [26] B.C. Thompson, J.M.J. Fréchet, Polymer–Fullerene Composite Solar Cells, *Angew. Chem. Int. Ed.* 47 (2008) 58–77. doi:10.1002/anie.200702506.
- [27] S. Margadonna, K. Prassides, Recent Advances in Fullerene Superconductivity, *J. Solid State Chem.* 168 (2002) 639–652. doi:10.1006/jssc.2002.9762.
- [28] T. Wharton, L.J. Wilson, Highly-Iodinated Fullerene as a Contrast Agent For X-ray Imaging, *Bioorg. Med. Chem.* 10 (2002) 3545–3554. doi:10.1016/S0968-0896(02)00252-3.
- [29] R. Singh, J.W. Lillard Jr., Nanoparticle-based targeted drug delivery, *Exp. Mol. Pathol.* 86 (2009) 215–223. doi:10.1016/j.yexmp.2008.12.004.
- [30] B.G. Demczyk, Y.M. Wang, J. Cumings, M. Hetman, W. Han, A. Zettl, R.O. Ritchie, Direct mechanical measurement of the tensile strength and elastic modulus of multiwalled carbon nanotubes, *Mater. Sci. Eng. A.* 334 (2002) 173–178. doi:10.1016/S0921-5093(01)01807-X.

- [31] K.I. Bolotin, K.J. Sikes, Z. Jiang, M. Klima, G. Fudenberg, J. Hone, P. Kim, H.L. Stormer, Ultrahigh electron mobility in suspended graphene, *Solid State Commun.* 146 (2008) 351–355. doi:10.1016/j.ssc.2008.02.024.
- [32] F. Kreupl, A.P. Graham, G.S. Duesberg, W. Steinhögl, M. Liebau, E. Unger, W. Hönlein, Carbon nanotubes in interconnect applications, *Microelectron. Eng.* 64 (2002) 399–408. doi:10.1016/S0167-9317(02)00814-6.
- [33] A.A. Balandin, S. Ghosh, W. Bao, I. Calizo, D. Teweldebrhan, F. Miao, C.N. Lau, Superior Thermal Conductivity of Single-Layer Graphene, *Nano Lett.* 8 (2008) 902–907. doi:10.1021/nl0731872.
- [34] Continuous, Highly Flexible, and Transparent Graphene Films by Chemical Vapor Deposition for Organic Photovoltaics - ACS Nano (ACS Publications), (n.d.). <http://pubs.acs.org/doi/abs/10.1021/nn901587x> (accessed July 5, 2015).
- [35] High Mobility, Printable, and Solution-Processed Graphene Electronics - Nano Letters (ACS Publications), (n.d.). <http://pubs.acs.org/doi/abs/10.1021/nl9028736> (accessed July 5, 2015).
- [36] T.S. Sreepasad, S.M. Maliyekkal, K.P. Lisha, T. Pradeep, Reduced graphene oxide–metal/metal oxide composites: Facile synthesis and application in water purification, *J. Hazard. Mater.* 186 (2011) 921–931. doi:10.1016/j.jhazmat.2010.11.100.
- [37] A.M.K. Esawi, M.M. Farag, Carbon nanotube reinforced composites: Potential and current challenges, *Mater. Des.* 28 (2007) 2394–2401. doi:10.1016/j.matdes.2006.09.022.
- [38] Flexible energy storage devices based on graphene paper - Energy & Environmental Science (RSC Publishing) DOI:10.1039/C0EE00640H, (n.d.). <http://pubs.rsc.org/en/content/articlehtml/2011/ee/c0ee00640h> (accessed July 5, 2015).
- [39] X. Li, Y. Qin, S.T. Picraux, Z.-X. Guo, Noncovalent assembly of carbon nanotube-inorganic hybrids, *J. Mater. Chem.* 21 (2011) 7527. doi:10.1039/c1jm10516g.
- [40] S. Förster, T. Plantenberg, From Self-Organizing Polymers to Nanohybrid and Biomaterials, *Angew. Chem. Int. Ed.* 41 (2002) 688–714. doi:10.1002/1521-3773(20020301)41:5<688::AID-ANIE688>3.0.CO;2-3.
- [41] J.-H. Yang, Y.-S. Han, M. Park, T. Park, S.-J. Hwang, J.-H. Choy, New Inorganic-Based Drug Delivery System of Indole-3-Acetic Acid-Layered Metal Hydroxide Nanohybrids with Controlled Release Rate, *Chem. Mater.* 19 (2007) 2679–2685. doi:10.1021/cm070259h.
- [42] Y. Wang, G. Ouyang, J. Zhang, Z. Wang, A DNA-templated catalyst: the preparation of metal-DNA nanohybrids and their application in organic reactions, *Chem. Commun.* 46 (2010) 7912. doi:10.1039/c0cc02632h.
- [43] K.-Y. Chun, Y. Oh, J. Rho, J.-H. Ahn, Y.-J. Kim, H.R. Choi, S. Baik, Highly conductive, printable and stretchable composite films of carbon nanotubes and silver, *Nat. Nanotechnol.* 5 (2010) 853–857. doi:10.1038/nnano.2010.232.
- [44] F. He, J. Fan, D. Ma, L. Zhang, C. Leung, H.L. Chan, The attachment of Fe<sub>3</sub>O<sub>4</sub> nanoparticles to graphene oxide by covalent bonding, *Carbon.* 48 (2010) 3139–3144. doi:10.1016/j.carbon.2010.04.052.
- [45] E. Antolini, Carbon supports for low-temperature fuel cell catalysts, *Appl. Catal. B Environ.* 88 (2009) 1–24. doi:10.1016/j.apcatb.2008.09.030.

- [46] S.-F. Zheng, J.-S. Hu, L.-S. Zhong, W.-G. Song, L.-J. Wan, Y.-G. Guo, Introducing Dual Functional CNT Networks into CuO Nanomicrospheres toward Superior Electrode Materials for Lithium-Ion Batteries, *Chem. Mater.* 20 (2008) 3617–3622. doi:10.1021/cm7033855.
- [47] X. Fu, H. Yu, F. Peng, H. Wang, Y. Qian, Facile preparation of RuO<sub>2</sub>/CNT catalyst by a homogenous oxidation precipitation method and its catalytic performance, *Appl. Catal. Gen.* 321 (2007) 190–197. doi:10.1016/j.apcata.2007.02.002.
- [48] J. Guerra, M.A. Herrero, Hybrid materials based on Pd nanoparticles on carbon nanostructures for environmentally benign C-C coupling chemistry, *Nanoscale.* 2 (2010) 1390–1400. doi:10.1039/c0nr00085j.
- [49] G.G. Wildgoose, C.E. Banks, R.G. Compton, Metal nanoparticles and related materials supported on carbon nanotubes: methods and applications, *Small Weinh. Bergstr. Ger.* 2 (2006) 182–193. doi:10.1002/smll.200500324.
- [50] V. Georgakilas, D. Gournis, V. Tzitzios, L. Pasquato, D.M. Guldi, M. Prato, Decorating carbon nanotubes with metal or semiconductor nanoparticles, *J. Mater. Chem.* 17 (2007) 2679–2694. doi:10.1039/B700857K.
- [51] X. Peng, J. Chen, J.A. Misewich, S.S. Wong, Carbon nanotube–nanocrystal heterostructures, *Chem. Soc. Rev.* 38 (2009) 1076–1098. doi:10.1039/B811424M.
- [52] N.T. Nikolaos Karousis, Current progress on the chemical modification of carbon nanotubes., *Chem. Rev.* 110 (2010) 5366–97. doi:10.1021/cr100018g.
- [53] V.N. Khabashesku, Covalent functionalization of carbon nanotubes: synthesis, properties and applications of fluorinated derivatives, *Russ. Chem. Rev.* 80 (2011) 705. doi:10.1070/RC2011v080n08ABEH004232.
- [54] J. Yun, J.S. Im, H.-I. Kim, Effect of oxygen plasma treatment of carbon nanotubes on electromagnetic interference shielding of polypyrrole-coated carbon nanotubes, *J. Appl. Polym. Sci.* 126 (2012) E39–E47. doi:10.1002/app.36709.
- [55] M.N. Tchoul, W.T. Ford, G. Lolli, D.E. Resasco, S. Arepalli, Effect of Mild Nitric Acid Oxidation on Dispersability, Size, and Structure of Single-Walled Carbon Nanotubes, *Chem. Mater.* 19 (2007) 5765–5772. doi:10.1021/cm071758l.
- [56] M. Zhang, L. Su, L. Mao, Surfactant functionalization of carbon nanotubes (CNTs) for layer-by-layer assembling of CNT multi-layer films and fabrication of gold nanoparticle/CNT nanohybrid, *Carbon.* 44 (2006) 276–283. doi:10.1016/j.carbon.2005.07.021.
- [57] Y.-L. Zhao, J.F. Stoddart, Noncovalent Functionalization of Single-Walled Carbon Nanotubes, *Acc. Chem. Res.* 42 (2009) 1161–1171. doi:10.1021/ar900056z.
- [58] M.J. O’Connell, P. Boul, L.M. Ericson, C. Huffman, Y. Wang, E. Haroz, C. Kuper, J. Tour, K.D. Ausman, R.E. Smalley, Reversible water-solubilization of single-walled carbon nanotubes by polymer wrapping, *Chem. Phys. Lett.* 342 (2001) 265–271. doi:10.1016/S0009-2614(01)00490-0.
- [59] A.N. Enyashin, S. Gemming, G. Seifert, DNA-wrapped carbon nanotubes, *Nanotechnology.* 18 (2007) 245702. doi:10.1088/0957-4484/18/24/245702.
- [60] L. Jiang, L. Gao, J. Sun, Production of aqueous colloidal dispersions of carbon nanotubes, *J. Colloid Interface Sci.* 260 (2003) 89–94. doi:10.1016/S0021-9797(02)00176-5.

- [61] T.J. Simmons, J. Bult, D.P. Hashim, R.J. Linhardt, P.M. Ajayan, Noncovalent Functionalization as an Alternative to Oxidative Acid Treatment of Single Wall Carbon Nanotubes with Applications for Polymer Composites, *ACS Nano*. 3 (2009) 865–870. doi:10.1021/nn800860m.
- [62] J.H.T. Luong, S. Hrapovic, D. Wang, F. Bensebaa, B. Simard, Solubilization of Multiwall Carbon Nanotubes by 3-Aminopropyltriethoxysilane Towards the Fabrication of Electrochemical Biosensors with Promoted Electron Transfer, *Electroanalysis*. 16 (2004) 132–139. doi:10.1002/elan.200302931.
- [63] C. Nie, C. Cheng, Z. Peng, L. Ma, C. He, Y. Xia, C. Zhao, Mussel-inspired coatings on Ag nanoparticle-conjugated carbon nanotubes: bactericidal activity and mammal cell toxicity, *J. Mater. Chem. B*. (2016). doi:10.1039/C6TB00470A.
- [64] A. Patole, G. Lubineau, Carbon nanotubes with silver nanoparticle decoration and conductive polymer coating for improving the electrical conductivity of polycarbonate composites, *Carbon*. 81 (2015) 720–730. doi:10.1016/j.carbon.2014.10.014.
- [65] A. Jorio, M.A. Pimenta, A.G.S. Filho, R. Saito, G. Dresselhaus, M.S. Dresselhaus, Characterizing carbon nanotube samples with resonance Raman scattering, *New J. Phys.* 5 (2003) 139. doi:10.1088/1367-2630/5/1/139.
- [66] A. Cao, C. Xu, J. Liang, D. Wu, B. Wei, X-ray diffraction characterization on the alignment degree of carbon nanotubes, *Chem. Phys. Lett.* 344 (2001) 13–17. doi:10.1016/S0009-2614(01)00671-6.
- [67] J. Yu, N. Grossiord, C.E. Koning, J. Loos, Controlling the dispersion of multi-wall carbon nanotubes in aqueous surfactant solution, *Carbon*. 45 (2007) 618–623. doi:10.1016/j.carbon.2006.10.010.
- [68] T.T. Nguyen, S.U. Nguyen, D.T. Phuong, D.C. Nguyen, A.T. Mai, Dispersion of denatured carbon nanotubes by using a dimethylformamide solution, *Adv. Nat. Sci. Nanosci. Nanotechnol.* 2 (2011) 035015. doi:10.1088/2043-6262/2/3/035015.
- [69] M.R. Das, R.K. Sarma, R. Saikia, V.S. Kale, M.V. Shelke, P. Sengupta, Synthesis of silver nanoparticles in an aqueous suspension of graphene oxide sheets and its antimicrobial activity, *Colloids Surf. B Biointerfaces*. 83 (2011) 16–22. doi:10.1016/j.colsurfb.2010.10.033.
- [70] Y. Sun, Y. Xia, Shape-Controlled Synthesis of Gold and Silver Nanoparticles, *Science*. 298 (2002) 2176–2179. doi:10.1126/science.1077229.
- [71] Y. Ye, T. Guo, Effect of MWNT electroless Ag plating on field emission properties of MWNT/Ag nanocomposite cathodes, *Appl. Surf. Sci.* 264 (2013) 593–597. doi:10.1016/j.apsusc.2012.10.071.
- [72] S.S. Bale, P. Asuri, S.S. Karajanagi, J.S. Dordick, R.S. Kane, Protein-Directed Formation of Silver Nanoparticles on Carbon Nanotubes, *Adv. Mater.* 19 (2007) 3167–3170. doi:10.1002/adma.200701981.
- [73] M. Leleental, Dimethylamine Borane as the Reducing Agent in Electroless Plating Systems, *J. Electrochem. Soc.* 120 (1973) 1650–1654. doi:10.1149/1.2403322.
- [74] S. Pal, Y.K. Tak, J.M. Song, Does the Antibacterial Activity of Silver Nanoparticles Depend on the Shape of the Nanoparticle? A Study of the Gram-Negative Bacterium *Escherichia coli*, *Appl. Environ. Microbiol.* 73 (2007) 1712–1720. doi:10.1128/AEM.02218-06.

- [75] B. Ajitha, Y.A.K. Reddy, P.S. Reddy, H.-J. Jeon, C.W. Ahn, Role of capping agents in controlling silver nanoparticles size, antibacterial activity and potential application as optical hydrogen peroxide sensor, *RSC Adv.* 6 (2016) 36171–36179. doi:10.1039/C6RA03766F.
- [76] R. Brause, H. Möltgen, K. Kleinermanns, Characterization of laser-ablated and chemically reduced silver colloids in aqueous solution by UV/VIS spectroscopy and STM/SEM microscopy, *Appl. Phys. B.* 75 (2002) 711–716. doi:10.1007/s00340-002-1024-3.
- [77] Y. Yuan, Y. Ji, Modeling corroded section configuration of steel bar in concrete structure, *Constr. Build. Mater.* 23 (2009) 2461–2466. doi:10.1016/j.conbuildmat.2008.09.026.
- [78] K. Watanabe, T. Kimura, J. Niwa, Synergetic effect of steel fibers and shear-reinforcing bars on the shear-resistance mechanisms of RC linear members, *Constr. Build. Mater.* 24 (2010) 2369–2375. doi:10.1016/j.conbuildmat.2010.05.009.
- [79] M.Z. Hossain, A.S.M.A. Awal, Flexural response of hybrid carbon fiber thin cement composites, *Constr. Build. Mater.* 25 (2011) 670–677. doi:10.1016/j.conbuildmat.2010.07.022.
- [80] J.M.L. Reis, Fracture and flexural characterization of natural fiber-reinforced polymer concrete, *Constr. Build. Mater.* 20 (2006) 673–678. doi:10.1016/j.conbuildmat.2005.02.008.
- [81] P. Soroushian, J.-P. Won, M. Hassan, Durability characteristics of CO<sub>2</sub>-cured cellulose fiber reinforced cement composites, *Constr. Build. Mater.* 34 (2012) 44–53. doi:10.1016/j.conbuildmat.2012.02.016.
- [82] P. Soroushian, A. Tlili, A. Alhozaimy, A. Khan, Development and characterization of hybrid polyethylene-fibre-reinforced cement composites, *Constr. Build. Mater.* 7 (1993) 221–229. doi:10.1016/0950-0618(93)90006-X.
- [83] H. Su, J. Xu, Dynamic compressive behavior of ceramic fiber reinforced concrete under impact load, *Constr. Build. Mater.* 45 (2013) 306–313. doi:10.1016/j.conbuildmat.2013.04.008.
- [84] N. Morova, Investigation of usability of basalt fibers in hot mix asphalt concrete, *Constr. Build. Mater.* 47 (2013) 175–180. doi:10.1016/j.conbuildmat.2013.04.048.
- [85] S. Chuah, Z. Pan, J.G. Sanjayan, C.M. Wang, W.H. Duan, Nano reinforced cement and concrete composites and new perspective from graphene oxide, *Constr. Build. Mater.* 73 (2014) 113–124. doi:10.1016/j.conbuildmat.2014.09.040.
- [86] Y. Qing, Z. Zenan, K. Deyu, C. Rongshen, Influence of nano-SiO<sub>2</sub> addition on properties of hardened cement paste as compared with silica fume, *Constr. Build. Mater.* 21 (2007) 539–545. doi:10.1016/j.conbuildmat.2005.09.001.
- [87] J. Björnström, A. Martinelli, A. Matic, L. Börjesson, I. Panas, Accelerating effects of colloidal nano-silica for beneficial calcium–silicate–hydrate formation in cement, *Chem. Phys. Lett.* 392 (2004) 242–248. doi:10.1016/j.cplett.2004.05.071.
- [88] B.G. Demczyk, Y.M. Wang, J. Cumings, M. Hetman, W. Han, A. Zettl, R.O. Ritchie, Direct mechanical measurement of the tensile strength and elastic modulus of multiwalled carbon nanotubes, *Mater. Sci. Eng. A.* 334 (2002) 173–178. doi:10.1016/S0921-5093(01)01807-X.

- [89] S. Lv, Y. Ma, C. Qiu, T. Sun, J. Liu, Q. Zhou, Effect of graphene oxide nanosheets of microstructure and mechanical properties of cement composites, *Constr. Build. Mater.* 49 (2013) 121–127. doi:10.1016/j.conbuildmat.2013.08.022.
- [90] S. Lv, S. Ting, J. Liu, Q. Zhou, Use of graphene oxide nanosheets to regulate the microstructure of hardened cement paste to increase its strength and toughness, *CrystEngComm.* 16 (2014) 8508–8516. doi:10.1039/C4CE00684D.
- [91] Z. Liu, Z. Li, Z. Xu, Z. Xia, X. Hu, L. Kou, L. Peng, Y. Wei, C. Gao, Wet-Spun Continuous Graphene Films, *Chem. Mater.* 26 (2014) 6786–6795. doi:10.1021/cm5033089.
- [92] N. Wang, D. Jiang, L. Ye, M. Murugesan, M. Edwards, Y. Fu, J. Liu, Flexible Multifunctionalized Carbon Nanotubes-Based Hybrid Nanowires, *Adv. Funct. Mater.* 25 (2015) 4135–4143. doi:10.1002/adfm.201501017.
- [93] J.I. Paredes, S. Villar-Rodil, A. Martínez-Alonso, J.M.D. Tascón, Graphene Oxide Dispersions in Organic Solvents, *Langmuir.* 24 (2008) 10560–10564. doi:10.1021/la801744a.
- [94] N. Wang, S. Pandit, L. Ye, M. Edwards, V.R.S.S. Mokkalapati, M. Murugesan, V. Kuzmenko, C. Zhao, F. Westerlund, I. Mijakovic, J. Liu, Efficient surface modification of carbon nanotubes for fabricating high performance CNT based hybrid nanostructures, *Carbon.* 111 (2017) 402–410. doi:10.1016/j.carbon.2016.10.027.
- [95] N.L. Thomas, J.D. Birchall, The retarding action of sugars on cement hydration, *Cem. Concr. Res.* 13 (1983) 830–842. doi:10.1016/0008-8846(83)90084-4.
- [96] N.B. Singh, R. Sarvahi, N.P. Singh, Effect of superplasticizers on the hydration of cement, *Cem. Concr. Res.* 22 (1992) 725–735. doi:10.1016/0008-8846(92)90095-D.
- [97] Z. Gao, Y. Zhang, Y. Fu, M.M.F. Yuen, J. Liu, Thermal chemical vapor deposition grown graphene heat spreader for thermal management of hot spots, *Carbon.* 61 (2013) 342–348. doi:10.1016/j.carbon.2013.05.014.
- [98] K.M.F. Shahil, A.A. Balandin, Graphene–Multilayer Graphene Nanocomposites as Highly Efficient Thermal Interface Materials, *Nano Lett.* 12 (2012) 861–867. doi:10.1021/nl203906r.
- [99] R. Prasher, Graphene Spreads the Heat, *Science.* 328 (2010) 185–186. doi:10.1126/science.1188998.
- [100] M. Seelmann-Eggebert, P. Meisen, F. Schaudel, P. Koidl, A. Vescan, H. Leier, Heat-spreading diamond films for GaN-based high-power transistor devices, *Diam. Relat. Mater.* 10 (2001) 744–749. doi:10.1016/S0925-9635(00)00562-8.
- [101] A.A. Balandin, S. Ghosh, W. Bao, I. Calizo, D. Teweldebrhan, F. Miao, C.N. Lau, Superior Thermal Conductivity of Single-Layer Graphene, *Nano Lett.* 8 (2008) 902–907. doi:10.1021/nl0731872.
- [102] S.H. Aboutalebi, M.M. Gudarzi, Q.B. Zheng, J.-K. Kim, Spontaneous Formation of Liquid Crystals in Ultralarge Graphene Oxide Dispersions, *Adv. Funct. Mater.* 21 (2011) 2978–2988. doi:10.1002/adfm.201100448.
- [103] Y. Hernandez, V. Nicolosi, M. Lotya, F.M. Blighe, Z. Sun, S. De, I.T. McGovern, B. Holland, M. Byrne, Y.K. Gun'Ko, J.J. Boland, P. Niraj, G. Duesberg, S. Krishnamurthy, R. Goodhue, J. Hutchison, V. Scardaci, A.C. Ferrari, J.N. Coleman,

- High-yield production of graphene by liquid-phase exfoliation of graphite, *Nat. Nanotechnol.* 3 (2008) 563–568. doi:10.1038/nnano.2008.215.
- [104] F. Liu, M.-H. Jang, H.D. Ha, J.-H. Kim, Y.-H. Cho, T.S. Seo, Facile Synthetic Method for Pristine Graphene Quantum Dots and Graphene Oxide Quantum Dots: Origin of Blue and Green Luminescence, *Adv. Mater.* 25 (2013) 3657–3662. doi:10.1002/adma.201300233.
- [105] R. Rozada, J.I. Paredes, S. Villar-Rodil, A. Martínez-Alonso, J.M.D. Tascón, Towards full repair of defects in reduced graphene oxide films by two-step graphitization, *Nano Res.* 6 (2013) 216–233. doi:10.1007/s12274-013-0298-6.
- [106] D. R. Dreyer, S. Park, C. W. Bielawski, R. S. Ruoff, The chemistry of graphene oxide, *Chem. Soc. Rev.* 39 (2010) 228–240. doi:10.1039/B917103G.
- [107] C. Botas, P. Álvarez, C. Blanco, R. Santamaría, M. Granda, M.D. Gutiérrez, F. Rodríguez-Reinoso, R. Menéndez, Critical temperatures in the synthesis of graphene-like materials by thermal exfoliation–reduction of graphite oxide, *Carbon.* 52 (2013) 476–485. doi:10.1016/j.carbon.2012.09.059.
- [108] F.C. Nix, D. MacNair, The Thermal Expansion of Pure Metals: Copper, Gold, Aluminum, Nickel, and Iron, *Phys. Rev.* 60 (1941) 597–605. doi:10.1103/PhysRev.60.597.
- [109] X. Xu, J. Chen, B. Li, Phonon thermal conduction in novel 2D materials, *J. Phys. Condens. Matter.* 28 (2016) 483001. doi:10.1088/0953-8984/28/48/483001.
- [110] D.L. Nika, A.A. Balandin, Phonons and thermal transport in graphene and graphene-based materials, *Rep. Prog. Phys.* 80 (2017) 036502. doi:10.1088/1361-6633/80/3/036502.
- [111] Z. Wei, Z. Ni, K. Bi, M. Chen, Y. Chen, In-plane lattice thermal conductivities of multilayer graphene films, *Carbon.* 49 (2011) 2653–2658. doi:10.1016/j.carbon.2011.02.051.
- [112] J. Zhang, H. Yang, G. Shen, P. Cheng, J. Zhang, S. Guo, Reduction of graphene oxide via L-ascorbic acid, *Chem. Commun.* 46 (2010) 1112–1114. doi:10.1039/B917705A.
- [113] I.K. Moon, J. Lee, R.S. Ruoff, H. Lee, Reduced graphene oxide by chemical graphitization, *Nat. Commun.* 1 (2010) 73. doi:10.1038/ncomms1067.
- [114] S. Pei, J. Zhao, J. Du, W. Ren, H.-M. Cheng, Direct reduction of graphene oxide films into highly conductive and flexible graphene films by hydrohalic acids, *Carbon.* 48 (2010) 4466–4474. doi:10.1016/j.carbon.2010.08.006.
- [115] N.-J. Song, C.-M. Chen, C. Lu, Z. Liu, Q.-Q. Kong, R. Cai, Thermally reduced graphene oxide films as flexible lateral heat spreaders, *J. Mater. Chem. A.* 2 (2014) 16563–16568. doi:10.1039/C4TA02693D.
- [116] J.D. Renteria, S. Ramirez, H. Malekpour, B. Alonso, A. Centeno, A. Zurutuza, A.I. Cocemasov, D.L. Nika, A.A. Balandin, Strongly Anisotropic Thermal Conductivity of Free-Standing Reduced Graphene Oxide Films Annealed at High Temperature, *Adv. Funct. Mater.* 25 (2015) 4664–4672. doi:10.1002/adfm.201501429.
- [117] C. Mattevi, G. Eda, S. Agnoli, S. Miller, K.A. Mkhoyan, O. Celik, D. Mastrogiovanni, G. Granozzi, E. Garfunkel, M. Chhowalla, Evolution of Electrical, Chemical, and Structural Properties of Transparent and Conducting Chemically Derived Graphene Thin Films, *Adv. Funct. Mater.* 19 (2009) 2577–2583. doi:10.1002/adfm.200900166.

- [118] S. Pei, H.-M. Cheng, The reduction of graphene oxide, *Carbon*. 50 (2012) 3210–3228. doi:10.1016/j.carbon.2011.11.010.
- [119] A. Ganguly, S. Sharma, P. Papakonstantinou, J. Hamilton, Probing the Thermal Deoxygenation of Graphene Oxide Using High-Resolution In Situ X-ray-Based Spectroscopies, *J. Phys. Chem. C*. 115 (2011) 17009–17019. doi:10.1021/jp203741y.
- [120] D.R. Chowdhury, C. Singh, A. Paul, Role of graphite precursor and sodium nitrate in graphite oxide synthesis, *RSC Adv*. 4 (2014) 15138–15145. doi:10.1039/C4RA01019A.
- [121] K. Parvez, Z.-S. Wu, R. Li, X. Liu, R. Graf, X. Feng, K. Müllen, Exfoliation of Graphite into Graphene in Aqueous Solutions of Inorganic Salts, *J. Am. Chem. Soc.* 136 (2014) 6083–6091. doi:10.1021/ja5017156.
- [122] L.M. Malard, M.A. Pimenta, G. Dresselhaus, M.S. Dresselhaus, Raman spectroscopy in graphene, *Phys. Rep.* 473 (2009) 51–87. doi:10.1016/j.physrep.2009.02.003.
- [123] L.G. Cançado, K. Takai, T. Enoki, M. Endo, Y.A. Kim, H. Mizusaki, A. Jorio, L.N. Coelho, R. Magalhães-Paniago, M.A. Pimenta, General equation for the determination of the crystallite size  $L_a$  of nanographite by Raman spectroscopy, *Appl. Phys. Lett.* 88 (2006) 163106. doi:10.1063/1.2196057.
- [124] Y. Wang, Y. Ye, K. Wu, Simultaneous observation of the triangular and honeycomb structures on highly oriented pyrolytic graphite at room temperature: An STM study, *Surf. Sci.* 600 (2006) 729–734. doi:10.1016/j.susc.2005.12.001.
- [125] L.G. Cançado, K. Takai, T. Enoki, M. Endo, Y.A. Kim, H. Mizusaki, N.L. Speziali, A. Jorio, M.A. Pimenta, Measuring the degree of stacking order in graphite by Raman spectroscopy, *Carbon*. 46 (2008) 272–275. doi:10.1016/j.carbon.2007.11.015.
- [126] X. Mu, X. Wu, T. Zhang, D.B. Go, T. Luo, Thermal Transport in Graphene Oxide – From Ballistic Extreme to Amorphous Limit, *Sci. Rep.* 4 (2014). doi:10.1038/srep03909.
- [127] T. Ma, Z. Liu, J. Wen, Y. Gao, X. Ren, H. Chen, C. Jin, X.-L. Ma, N. Xu, H.-M. Cheng, W. Ren, Tailoring the thermal and electrical transport properties of graphene films by grain size engineering, *Nat. Commun.* 8 (2017) 14486. doi:10.1038/ncomms14486.
- [128] Y. Hishiyama, A. Yoshida, Y. Kaburagi, M. Inagaki, Graphite films prepared from carbonized polyimide films, *Carbon*. 30 (1992) 333–337. doi:10.1016/0008-6223(92)90027-T.
- [129] G. Xin, H. Sun, T. Hu, H.R. Fard, X. Sun, N. Koratkar, T. Borca-Tasciuc, J. Lian, Large-Area Freestanding Graphene Paper for Superior Thermal Management, *Adv. Mater.* 26 (2014) 4521–4526. doi:10.1002/adma.201400951.
- [130] B. Shen, W. Zhai, W. Zheng, Ultrathin Flexible Graphene Film: An Excellent Thermal Conducting Material with Efficient EMI Shielding, *Adv. Funct. Mater.* 24 (2014) 4542–4548. doi:10.1002/adfm.201400079.
- [131] G. Xin, T. Yao, H. Sun, S.M. Scott, D. Shao, G. Wang, J. Lian, Highly thermally conductive and mechanically strong graphene fibers, *Science*. 349 (2015) 1083–1087. doi:10.1126/science.aaa6502.
- [132] H. Chen, M.B. Müller, K.J. Gilmore, G.G. Wallace, D. Li, Mechanically Strong, Electrically Conductive, and Biocompatible Graphene Paper, *Adv. Mater.* 20 (2008) 3557–3561. doi:10.1002/adma.200800757.

- [133] C. Teng, D. Xie, J. Wang, Z. Yang, G. Ren, Y. Zhu, Ultrahigh Conductive Graphene Paper Based on Ball-Milling Exfoliated Graphene, *Adv. Funct. Mater.* (2017) n/a-n/a. doi:10.1002/adfm.201700240.
- [134] Z. Liu, Z. Li, Z. Xu, Z. Xia, X. Hu, L. Kou, L. Peng, Y. Wei, C. Gao, Wet-Spun Continuous Graphene Films, *Chem. Mater.* 26 (2014) 6786–6795. doi:10.1021/cm5033089.
- [135] X. Wang, L. Zhi, K. Müllen, Transparent, Conductive Graphene Electrodes for Dye-Sensitized Solar Cells, *Nano Lett.* 8 (2008) 323–327. doi:10.1021/nl072838r.
- [136] J. Li, F. Ye, S. Vaziri, M. Muhammed, M.C. Lemme, M. Östling, Efficient Inkjet Printing of Graphene, *Adv. Mater.* 25 (2013) 3985–3992. doi:10.1002/adma.201300361.
- [137] H.A. Becerril, J. Mao, Z. Liu, R.M. Stoltenberg, Z. Bao, Y. Chen, Evaluation of Solution-Processed Reduced Graphene Oxide Films as Transparent Conductors, *ACS Nano.* 2 (2008) 463–470. doi:10.1021/nn700375n.
- [138] Y. Li, K. (Jack) Moon, C.P. Wong, Nano-conductive Adhesives for Nano-electronics Interconnection, in: C.P. Wong, K.-S. Moon, Y. (Grace) Li (Eds.), *Nano-Bio- Electron. Photonic MEMS Packag.*, Springer US, 2010: pp. 19–45. doi:10.1007/978-1-4419-0040-1\_2.
- [139] N. Wang, M. Murugesan, L. Ye, B. Carlberg, S. Chen, J. Liu, Reliability investigation of nano-enhanced thermal conductive adhesives, in: 2012 12th IEEE Conf. Nanotechnol. IEEE-NANO, 2012: pp. 1–6. doi:10.1109/NANO.2012.6322137.
- [140] H.P. Wu, X.J. Wu, M.Y. Ge, G.Q. Zhang, Y.W. Wang, J. Jiang, Properties investigation on isotropical conductive adhesives filled with silver coated carbon nanotubes, *Compos. Sci. Technol.* 67 (2007) 1182–1186. doi:10.1016/j.compscitech.2006.05.010.
- [141] Z. Han, A. Fina, Thermal conductivity of carbon nanotubes and their polymer nanocomposites: A review, *Prog. Polym. Sci.* 36 (2011) 914–944. doi:10.1016/j.progpolymsci.2010.11.004.
- [142] E. Hammel, X. Tang, M. Trampert, T. Schmitt, K. Mauthner, A. Eder, P. Pötschke, Carbon nanofibers for composite applications, *Carbon.* 42 (2004) 1153–1158. doi:10.1016/j.carbon.2003.12.043.
- [143] H.P. Wu, J.F. Liu, X.J. Wu, M.Y. Ge, Y.W. Wang, G.Q. Zhang, J.Z. Jiang, High conductivity of isotropic conductive adhesives filled with silver nanowires, *Int. J. Adhes. Adhes.* 26 (2006) 617–621. doi:10.1016/j.ijadhadh.2005.10.001.
- [144] K.M.F. Shahil, A.A. Balandin, Graphene–Multilayer Graphene Nanocomposites as Highly Efficient Thermal Interface Materials, *Nano Lett.* 12 (2012) 861–867. doi:10.1021/nl203906r.
- [145] A.A. Balandin, S. Ghosh, W. Bao, I. Calizo, D. Teweldebrhan, F. Miao, C.N. Lau, Superior Thermal Conductivity of Single-Layer Graphene, *Nano Lett.* 8 (2008) 902–907. doi:10.1021/nl0731872.
- [146] Y.-X. Fu, Z.-X. He, D.-C. Mo, S.-S. Lu, Thermal conductivity enhancement of epoxy adhesive using graphene sheets as additives, *Int. J. Therm. Sci.* 86 (2014) 276–283. doi:10.1016/j.ijthermalsci.2014.07.011.

- [147] Y. Hernandez, V. Nicolosi, M. Lotya, F.M. Blighe, Z. Sun, S. De, I.T. McGovern, B. Holland, M. Byrne, Y.K. Gun'Ko, J.J. Boland, P. Niraj, G. Duesberg, S. Krishnamurthy, R. Goodhue, J. Hutchison, V. Scardaci, A.C. Ferrari, J.N. Coleman, High-yield production of graphene by liquid-phase exfoliation of graphite, *Nat. Nanotechnol.* 3 (2008) 563–568. doi:10.1038/nnano.2008.215.
- [148] A. Kozbial, Z. Li, C. Conaway, R. McGinley, S. Dhingra, V. Vahdat, F. Zhou, B. D'Urso, H. Liu, L. Li, Study on the Surface Energy of Graphene by Contact Angle Measurements, *Langmuir.* 30 (2014) 8598–8606. doi:10.1021/la5018328.
- [149] S. Wang, Y. Zhang, N. Abidi, L. Cabrales, Wettability and Surface Free Energy of Graphene Films, *Langmuir.* 25 (2009) 11078–11081. doi:10.1021/la901402f.
- [150] J. Lyklema, The surface tension of pure liquids: Thermodynamic components and corresponding states, *Colloids Surf. Physicochem. Eng. Asp.* 156 (1999) 413–421. doi:10.1016/S0927-7757(99)00100-4.
- [151] A. O'Neill, U. Khan, P.N. Nirmalraj, J. Boland, J.N. Coleman, Graphene Dispersion and Exfoliation in Low Boiling Point Solvents, *J. Phys. Chem. C.* 115 (2011) 5422–5428. doi:10.1021/jp110942e.
- [152] J.L. Ross, W.D. Bruce, W.S. Janna, Surface tension measurements of benzyl benzoate using the Sugden maximum bubble pressure method, *Langmuir.* 8 (1992) 2644–2648. doi:10.1021/la00047a013.
- [153] S.D. Bergin, V. Nicolosi, P.V. Streich, S. Giordani, Z. Sun, A.H. Windle, P. Ryan, N.P.P. Niraj, Z.-T.T. Wang, L. Carpenter, W.J. Blau, J.J. Boland, J.P. Hamilton, J.N. Coleman, Towards Solutions of Single-Walled Carbon Nanotubes in Common Solvents, *Adv. Mater.* 20 (2008) 1876–1881. doi:10.1002/adma.200702451.
- [154] A.B. Bourlinos, V. Georgakilas, R. Zboril, T.A. Steriotis, A.K. Stubos, Liquid-Phase Exfoliation of Graphite Towards Solubilized Graphenes, *Small.* 5 (2009) 1841–1845. doi:10.1002/sml.200900242.
- [155] S.R. Dhakate, N. Chauhan, S. Sharma, J. Tawale, S. Singh, P.D. Sahare, R.B. Mathur, An approach to produce single and double layer graphene from re-exfoliation of expanded graphite, *Carbon.* 49 (2011) 1946–1954. doi:10.1016/j.carbon.2010.12.068.
- [156] S. Stankovich, D.A. Dikin, R.D. Piner, K.A. Kohlhaas, A. Kleinhammes, Y. Jia, Y. Wu, S.T. Nguyen, R.S. Ruoff, Synthesis of graphene-based nanosheets via chemical reduction of exfoliated graphite oxide, *Carbon.* 45 (2007) 1558–1565. doi:10.1016/j.carbon.2007.02.034.
- [157] J. Zhang, H. Yang, G. Shen, P. Cheng, J. Zhang, S. Guo, Reduction of graphene oxide via L-ascorbic acid, *Chem. Commun.* 46 (2010) 1112–1114. doi:10.1039/B917705A.
- [158] A.C. Ferrari, J.C. Meyer, V. Scardaci, C. Casiraghi, M. Lazzeri, F. Mauri, S. Piscanec, D. Jiang, K.S. Novoselov, S. Roth, A.K. Geim, Raman Spectrum of Graphene and Graphene Layers, *Phys. Rev. Lett.* 97 (2006) 187401. doi:10.1103/PhysRevLett.97.187401.
- [159] J.H. Byeon, J. Hwang, Morphology of metallic nanoparticles as a function of deposition time in electroless deposition of metal on multi-walled carbon nanotubes, *Surf. Coat. Technol.* 203 (2008) 357–363. doi:10.1016/j.surfcoat.2008.09.017.

- [160] X. Ma, N. Lun, S. Wen, Formation of gold nanoparticles supported on carbon nanotubes by using an electroless plating method, *Diam. Relat. Mater.* 14 (2005) 68–73. doi:10.1016/j.diamond.2004.07.002.
- [161] L. Zhao, L. Gao, Stability of multi-walled carbon nanotubes dispersion with copolymer in ethanol, *Colloids Surf. Physicochem. Eng. Asp.* 224 (2003) 127–134. doi:10.1016/S0927-7757(03)00155-9.
- [162] Y. Yamada, K. Yano, Synthesis of monodispersed super-microporous/mesoporous silica spheres with diameters in the low submicron range, *Microporous Mesoporous Mater.* 93 (2006) 190–198. doi:10.1016/j.micromeso.2006.02.013.
- [163] Z. Xiu, Y. Wu, X. Hao, L. Zhang, Fabrication of SiO<sub>2</sub>@Ag@SiO<sub>2</sub> core-shell microspheres and thermal stability investigation, *Colloids Surf. Physicochem. Eng. Asp.* 386 (2011) 135–140. doi:10.1016/j.colsurfa.2011.07.018.
- [164] F. Tang, L. Li, D. Chen, Mesoporous Silica Nanoparticles: Synthesis, Biocompatibility and Drug Delivery, *Adv. Mater.* 24 (2012) 1504–1534. doi:10.1002/adma.201104763.
- [165] S.K. Choi, K.-Y. Chun, S.-B. Lee, Selective decoration of silver nanoparticles on the defect sites of single-walled carbon nanotubes, *Diam. Relat. Mater.* 18 (2009) 637–641. doi:10.1016/j.diamond.2008.11.006.
- [166] X. Ma, N. Lun, S. Wen, Formation of gold nanoparticles supported on carbon nanotubes by using an electroless plating method, *Diam. Relat. Mater.* 14 (2005) 68–73. doi:10.1016/j.diamond.2004.07.002.
- [167] S. Guo, J. Li, W. Ren, D. Wen, S. Dong, E. Wang, Carbon Nanotube/Silica Coaxial Nanocable as a Three-Dimensional Support for Loading Diverse Ultra-High-Density Metal Nanostructures: Facile Preparation and Use as Enhanced Materials for Electrochemical Devices and SERS, *Chem. Mater.* 21 (2009) 2247–2257. doi:10.1021/cm900300v.
- [168] Joseph Fjelstad, Flexible circuitry - technology background and important fundamental issues, *Circuit World.* 25 (1999) 6–10. doi:10.1108/03056129910258207.
- [169] J.A. Rogers, Z. Bao, K. Baldwin, A. Dodabalapur, B. Crone, V.R. Raju, V. Kuck, H. Katz, K. Amundson, J. Ewing, P. Drzaic, Paper-like electronic displays: Large-area rubber-stamped plastic sheets of electronics and microencapsulated electrophoretic inks, *Proc. Natl. Acad. Sci.* 98 (2001) 4835–4840. doi:10.1073/pnas.091588098.
- [170] S. Park, S. Jayaraman, Smart Textiles: Wearable Electronic Systems, *MRS Bull.* 28 (2003) 585–591. doi:10.1557/mrs2003.170.
- [171] D.J. Lipomi, B.C.-K. Tee, M. Vosgueritchian, Z. Bao, Stretchable Organic Solar Cells, *Adv. Mater.* 23 (2011) 1771–1775. doi:10.1002/adma.201004426.
- [172] H.C. Ko, M.P. Stoykovich, J. Song, V. Malyarchuk, W.M. Choi, C.-J. Yu, J.B. Geddes Iii, J. Xiao, S. Wang, Y. Huang, J.A. Rogers, A hemispherical electronic eye camera based on compressible silicon optoelectronics, *Nature.* 454 (2008) 748–753. doi:10.1038/nature07113.
- [173] R. Carta, P. Jourand, B. Hermans, J. Thoné, D. Brosteaux, T. Vervust, F. Bossuyt, F. Axisa, J. Vanfleteren, R. Puers, Design and implementation of advanced systems in a flexible-stretchable technology for biomedical applications, *Sens. Actuators Phys.* 156 (2009) 79–87. doi:10.1016/j.sna.2009.03.012.

- [174] T. Sekitani, T. Someya, Stretchable, Large-area Organic Electronics, *Adv. Mater.* 22 (2010) 2228–2246. doi:10.1002/adma.200904054.
- [175] M. Gonzalez, F. Axisa, M.V. Bulcke, D. Brosteaux, B. Vandeveld, J. Vanfleteren, Design of metal interconnects for stretchable electronic circuits, *Microelectron. Reliab.* 48 (2008) 825–832. doi:10.1016/j.microrel.2008.03.025.
- [176] X. Wang, H. Hu, Y. Shen, X. Zhou, Z. Zheng, Stretchable Conductors with Ultrahigh Tensile Strain and Stable Metallic Conductance Enabled by Prestrained Polyelectrolyte Nanoplayers, *Adv. Mater.* 23 (2011) 3090–3094. doi:10.1002/adma.201101120.
- [177] P. Calvert, Inkjet Printing for Materials and Devices, *Chem. Mater.* 13 (2001) 3299–3305. doi:10.1021/cm0101632.
- [178] T.-Y. Dong, W.-T. Chen, C.-W. Wang, C.-P. Chen, C.-N. Chen, M.-C. Lin, J.-M. Song, I.-G. Chen, T.-H. Kao, One-step synthesis of uniform silver nanoparticles capped by saturated decanoate: direct spray printing ink to form metallic silver films, *Phys. Chem. Chem. Phys.* 11 (2009) 6269–6275. doi:10.1039/B900691E.
- [179] K. Kordás, T. Mustonen, G. Tóth, H. Jantunen, M. Lajunen, C. Soldano, S. Talapatra, S. Kar, R. Vajtai, P.M. Ajayan, Inkjet Printing of Electrically Conductive Patterns of Carbon Nanotubes, *Small.* 2 (2006) 1021–1025. doi:10.1002/smll.200600061.
- [180] J. Wu, M. Agrawal, H.A. Becerril, Z. Bao, Z. Liu, Y. Chen, P. Peumans, Organic Light-Emitting Diodes on Solution-Processed Graphene Transparent Electrodes, *ACS Nano.* 4 (2010) 43–48. doi:10.1021/nn900728d.
- [181] L. Hu, H.S. Kim, J.-Y. Lee, P. Peumans, Y. Cui, Scalable Coating and Properties of Transparent, Flexible, Silver Nanowire Electrodes, *ACS Nano.* 4 (2010) 2955–2963. doi:10.1021/nn1005232.
- [182] Z. Chen, W. Ren, L. Gao, B. Liu, S. Pei, H.-M. Cheng, Three-dimensional flexible and conductive interconnected graphene networks grown by chemical vapour deposition, *Nat. Mater.* 10 (2011) 424–428. doi:10.1038/nmat3001.
- [183] T. Kim, H. Song, J. Ha, S. Kim, D. Kim, S. Chung, J. Lee, Y. Hong, Inkjet-printed stretchable single-walled carbon nanotube electrodes with excellent mechanical properties, *Appl. Phys. Lett.* 104 (2014) 113103. doi:10.1063/1.4868633.
- [184] T. Sekitani, Y. Noguchi, K. Hata, T. Fukushima, T. Aida, T. Someya, A Rubberlike Stretchable Active Matrix Using Elastic Conductors, *Science.* 321 (2008) 1468–1472. doi:10.1126/science.1160309.
- [185] S. Yun, X. Niu, Z. Yu, W. Hu, P. Brochu, Q. Pei, Compliant Silver Nanowire-Polymer Composite Electrodes for Bistable Large Strain Actuation, *Adv. Mater.* 24 (2012) 1321–1327. doi:10.1002/adma.201104101.
- [186] K. Takei, Z. Yu, M. Zheng, H. Ota, T. Takahashi, A. Javey, Highly sensitive electronic whiskers based on patterned carbon nanotube and silver nanoparticle composite films, *Proc. Natl. Acad. Sci. U. S. A.* 111 (2014) 1703–1707. doi:10.1073/pnas.1317920111.
- [187] F. Xu, Y. Zhu, Highly Conductive and Stretchable Silver Nanowire Conductors, *Adv. Mater.* 24 (2012) 5117–5122. doi:10.1002/adma.201201886.
- [188] K.-Y. Chun, Y. Oh, J. Rho, J.-H. Ahn, Y.-J. Kim, H.R. Choi, S. Baik, Highly conductive, printable and stretchable composite films of carbon nanotubes and silver, *Nat. Nanotechnol.* 5 (2010) 853–857. doi:10.1038/nnano.2010.232.

- [189] M. Park, J. Im, M. Shin, Y. Min, J. Park, H. Cho, S. Park, M.-B. Shim, S. Jeon, D.-Y. Chung, J. Bae, J. Park, U. Jeong, K. Kim, Highly stretchable electric circuits from a composite material of silver nanoparticles and elastomeric fibres, *Nat. Nanotechnol.* 7 (2012) 803–809. doi:10.1038/nnano.2012.206.
- [190] Y. Yu, J. Zeng, C. Chen, Z. Xie, R. Guo, Z. Liu, X. Zhou, Y. Yang, Z. Zheng, Three-Dimensional Compressible and Stretchable Conductive Composites, *Adv. Mater.* 26 (2014) 810–815. doi:10.1002/adma.201303662.
- [191] Y. Li, H. Shimizu, Toward a Stretchable, Elastic, and Electrically Conductive Nanocomposite: Morphology and Properties of Poly[styrene-*b*-(ethylene-co-butylene)-*b*-styrene]/Multiwalled Carbon Nanotube Composites Fabricated by High-Shear Processing, *Macromolecules.* 42 (2009) 2587–2593. doi:10.1021/ma802662c.
- [192] L. Hu, M. Pasta, F.L. Mantia, L. Cui, S. Jeong, H.D. Deshazer, J.W. Choi, S.M. Han, Y. Cui, Stretchable, Porous, and Conductive Energy Textiles, *Nano Lett.* 10 (2010) 708–714. doi:10.1021/nl903949m.
- [193] J. Li, L. Liu, D. Zhang, D. Yang, J. Guo, J. Wei, Fabrication of polyaniline/silver nanoparticles/multi-walled carbon nanotubes composites for flexible microelectronic circuits, *Synth. Met.* 192 (2014) 15–22. doi:10.1016/j.synthmet.2014.02.026.